

REPORT DOCUMENTATION PAGE

AD-A201 411

DTIC
RECEIVED

D

SCHEDULE 9 1988

D 4

4. PERFORMING ORGANIZATION REPORT NUMBER(S)

6a. NAME OF PERFORMING ORGANIZATION
Univ. of Puerto Rico6b. OFFICE SYMBOL
(If applicable)

6c. ADDRESS (City, State, and ZIP Code)

Rio Piedras Campus
San Juan, Puerto Rico6a. NAME OF FUNDING/SPONSORING
ORGANIZATION

U. S. Army Research Office

8c. ADDRESS (City, State, and ZIP Code)

P. O. Box 12211
Research Triangle Park, NC 27709-22118b. OFFICE SYMBOL
(If applicable)

11. TITLE (Include Security Classification)

Optical and Electrical Properties of Co-Sputtered Semiconductors and Metal-Insulator Films

12. PERSONAL AUTHOR(S)

Zvi S. Weisz, Manuel Gomez-Rodriguez, and James A. Muir

13a. TYPE OF REPORT
Final13b. TIME COVERED
FROM 8/1/84 TO 7/31/8814. DATE OF REPORT (Year, Month, Day)
August 1988

15. PAGE COUNT

16. SUPPLEMENTARY NOTATION

The view, opinions and/or findings contained in this report are those of the author(s) and should not be construed as an official Department of the Army position, policy, or decision, unless so designated by other documentation.

17. COSATI CODES

18. SUBJECT TERMS (Continue on reverse if necessary and identify by block number)

Semiconductors, Metal-Insulator Films, Thin Films,
Sputtering Techniques, Semiconductor Alloys, Surface
Plasmons, Silver, Optical Properties, Electrical Properties

19. ABSTRACT (Continue on reverse if necessary and identify by block number)

The objective of the investigation was the study of thin films prepared mostly by sputtering techniques. Specifically, the objectives include (a) the investigation of the optical and electrical properties of hydrogenated amorphous semiconductor alloys and the effect on these properties of the mode of preparation, and (b) the study of surface plasmons on silver with the view of gaining further understanding of surface enhanced Raman scattering.

One of the most important parameters in an amorphous semiconductor alloy system is the alloy composition. To determine this parameter the method of Auger depth profiling was used. Upon closer examination of this method, some problems were found that affect the accuracy of the determination of the alloy composition from Auger measurements. Because of the widespread use of Auger spectroscopy for quantitative analysis, certain aspects of Auger electron spectroscopy were investigated. In addition, it was also necessary to include some work on crystalline semiconductors (Si and ZnO).—

20. DISTRIBUTION/AVAILABILITY OF ABSTRACT

 UNCLASSIFIED/UNLIMITED SAME AS RPT. DTIC USEPC

21. ABSTRACT SECURITY CLASSIFICATION

Unclassified

22a. NAME OF RESPONSIBLE INDIVIDUAL

22b. TELEPHONE (Include Area Code)

22c. OFFICE SYMBOL

**OPTICAL AND ELECTRICAL PROPERTIES OF CO-SPUTTERED
SEMICONDUCTORS AND METAL-INSULATOR FILMS**

FINAL REPORT

Principal Investigators: Zvi S. Weisz, Manuel Gomez-Rodriguez,
and James A. Muir

July 30, 1988

U.S. ARMY RESEARCH OFFICE
Grant Number DAAG29-84-G-0059



UNIVERSITY OF PUERTO RICO, RIO PIEDRAS

**APPROVED FOR PUBLIC RELEASE;
DISTRIBUTION UNLIMITED.**

SEARCHED	INDEXED
SERIALIZED	FILED
JULY 30 1988	
U.S. ARMY RESEARCH OFFICE	
DAAG29-84-G-0059	
UNIVERSITY OF PUERTO RICO	
RIO PIEDRAS	

A-1

88 1017, 05 9

TABLE OF CONTENTS

1. Objective.....	1
2. Summary of results.....	2
3. List of publications.....	9
4. Scientific personnel supported.....	11
5. Appendixes, reprints and preprints.....	12

Objective. The objective of the investigation was the study of thin films prepared mostly by sputtering techniques.

Specifically, the objectives included (a) the investigation of the optical and electrical properties of hydrogenated amorphous semiconductor alloys and the effect on these properties of the mode of preparation, and (b) the study of surface plasmons on silver with the view of gaining further understanding of surface enhanced Raman scattering.

One of the most important parameters in an amorphous semiconductor alloy system is the alloy composition. To determine this parameter we used, like many other investigators, the method of Auger depth profiling. Upon closer examination of this method we came across some problems that affect the accuracy of the determination of the alloy composition from Auger measurements. Because of the widespread use of Auger spectroscopy for quantitative analysis, we felt it appropriate to include in our investigation certain aspects of Auger electron spectroscopy. In addition, in the course of our investigation we also found it necessary to include in our research some work on crystalline semiconductors (Si and ZnO).

1. Auger electron spectroscopy for quantitative analysis. One of the most important conclusions resulting from this investigation is not related directly to the sputtered alloys but to the determination, by Auger measurements, of alloy composition. Careful Auger measurements on MgO showed that unless the instrumental resolution width is sufficiently narrow, the atomic concentrations derived from the Auger measurements are resolution dependent. A mathematical analysis, developed by us, shows that unless the ratio of the instrumental resolution linewidth to the natural linewidth of each Auger line is less than about 0.3, the measured peak-to-peak amplitudes of the differentiated Auger signals do not represent accurately the atomic concentrations. At the same time, the analysis provides the means for overcoming this difficulty even when the linewidth ratio is considerably larger than 0.3. A universal curve was presented whereby the experimentally measured peak-to-peak amplitudes can be corrected so as to enable one to derive quite accurately the relative atomic concentrations in one's samples. Unfortunately, however, most of the available Auger sensitivity data required for quantitative analysis, do not specify the instrumental resolution used. In fact, we showed that at least in some cases the published data were measured with a resolution far from satisfactory. It is our contention, therefore, that there is a need for re-measurement of the sensitivity data with adequate resolution if a really quantitative determination of atomic concentrations is to become feasible.

We also measured the Auger spectra of the polar and prism surfaces of single crystal ZnO. The results showed that the sensitivity factors for oxygen from the Physical Electronic's Handbook of Auger Electron Spectroscopy are non-applicable to ZnO. The values for the sensitivities deduced from our results are 0.26 for an incident electron energy of 3 keV and 0.25 for 5 keV. These values agree fairly well with the theoretical values of Mroczkowski and Lichtman. High resolution measurements revealed also that the principal line of the oxygen Auger derivative spectrum of ZnO consists of double peaks. It was concluded that the double peaks are probably due to local maxima in the valence-band density of states of ZnO.

2. Hydrogenated amorphous Si-Sn alloy films. Amorphous Si-Sn films were prepared at different temperatures between 100 and 200°C. The tin content of the films was up to about 11 at.% and was determined using Auger depth profiling. The optical absorption and photoconductivity were measured as a function of wavelength and film composition. The energy gap, as evaluated from these measurements, decreases as the tin content increases, the lower the temperature of preparation the more pronounced this decrease. For instance, for 100°C sputtering the gap decreases by 0.7 eV for 5 at.% tin while for 200°C sputtering the gap decreases "only" by about 0.4 eV. We also find that the dark conductivity of the films (which is of course a function of tin concentration) decreases with increasing preparation temperature. Likewise, the photoconductance response, ν , increases by close to two orders of magnitude as the sputtering temperature varies

between 100 and 200°C. As a function of composition, at all preparation temperatures, ν_m decreases strongly with increasing tin concentration.

For infrared measurements the films were deposited on impurity-free silicon substrates. On these films the oxygen contamination was found to increase with tin concentration but it was uniform over the thickness of the films. The infrared measurements showed vibrational bands characteristic of Si-H, Sn-H, Si-O and perhaps Sn-O. The presence of Sn was found to facilitate the formation of more Si-H and SiH₂ bonds. The Si-O band was found to shift from 1030 cm⁻¹ to 1075 cm⁻¹ as the Sn concentration increased to 10 at.%. In addition, a new peak at 1155 cm⁻¹ appeared in the mixed samples for Sn concentrations over about 10 at.%.

3. Surface plasmons on silver films. The surface-plasmon spectrum was measured by Electron Loss Spectroscopy (ELS), using incident electron energies of 20 eV. We compared the ELS spectrum of smooth silver surfaces with silver surfaces roughened electrolytically. Immediately after introducing the smooth sample into the ultra-high vacuum system and prior to any cleaning, we found a loss peak at 3.41 eV which is due to the surface plasmon of silver. Actually, the energy of the surface plasmon of silver is somewhat larger (by about 0.2 eV) and the shift to lower energies is attributed to adsorbates on the surface. And indeed, after cleaning the sample by argon-ion sputtering, the energy loss of the surface plasmon increased to 3.65 eV. This shift is

appreciable and the lower energy-loss peak could have possibly been mistakenly identified with a localized-mode plasmon.

Rough surfaces were prepared by electrolytic roughening. After the roughening the samples were coated by a thin layer of PNBA (para nitrobenzoic acid). The Raman spectrum from the rough surfaces exhibited several Raman peaks enhanced by the rough surface. Comparing the spectrum to the signal measured on smooth surfaces we ascertained that the Raman spectrum is due to surface enhanced Raman scattering.

After inserting the sample into the vacuum system and cleaning it we measured its ELS spectrum. We found again the prominent surface-plasmon peak at 3.65 eV, identical to that observed on the smooth surface, but we also saw a peak or shoulder between 1.5 and 2.5 eV, centered around 2 eV. After the sample underwent a repeated cleaning cycle, the feature around 2 eV became very weak, sometimes even hard to detect. Part of the difficulty is due to the fact that this feature is partially obscured by the tail of the elastic peak. The absorption peak or shoulder around 2 eV may possibly be due to localized plasmons. However, our results are very much of a preliminary nature and further work is required to resolve this question.

4. The study of the electronic structure using the semiconductor electrolyte interface. As a preliminary to our investigation of amorphous semiconductors and in order to familiarize ourselves with this method, which was successfully applied in the past to single crystal semiconductors, we started with the study of crystalline silicon and crystalline ZnO. The measurements showed

that at the Si surface, excess surface electron densities as high as 10^{14} cm^{-2} can be induced. (These densities are over an order of magnitude larger than can be attained in Si inversion layers in MOS structures.) A complete mapping out of the surface-state energy distribution in the upper half of the forbidden gap has been carried out. The surface states, of total density of about 10^{12} cm^{-2} and of capture cross sections around $5 \times 10^{-18} \text{ cm}^2$, were found to be distributed uniformly in an energy interval of 0.2 eV, centered 0.3 eV below the conduction-band edge. In strong accumulation layers, charge leakage across the interface took place, most probably by a tunneling process. The leakage occurs practically instantaneously, in a time less than 50 nsec, but the leakage charge remains stored near the interface for considerably longer times. We put forward some ideas to explain this unusual behaviour. Studies on (thin film) hydrogenated amorphous silicon, now in progress, show that the electronic structure is much more complex than in the case of crystalline silicon.

Publications

1. Low Energy Hydrogen-Ion Implantation on Thermally Treated ZnO Surfaces. G. Yaron, J. Levy, A. Many, Y. Goldstein, S.Z. Weisz, and O. Resto. *J. Phys. Chem. Solids* **47**, 401 (1986).
2. Space Charge and Surface State Characteristics of the Silicon/Electrolyte Interface. M. Wolovelsky, J. Levy, Y. Goldstein, A. Many, S.Z. Weisz, and O. Resto. *Surf. Sci.* **171**, 442 (1986).
3. Alloying Effects on the Optical Absorption Edge and Photoconductance of RF Sputtered $a\text{-Sn}(x)\text{Si}(1-x)$ Films. R. Perez, O. Resto, S.Z. Weisz, and Y. Goldstein. *Appl. Phys. Commun.* **7**, 291 (1987).
4. Calibration of Oxygen Auger Signal from Single-Crystal ZnO Surfaces. S.Z. Weisz, O. Resto, G. Yaron, A. Many, and Y. Goldstein. *J. Vac. Sci. & Technology A* **5**, 302 (1987).
5. Infrared Spectroscopy of $a\text{-Si}_{1-x}\text{Sn}_x\text{:H}$ Films. R.S. Katiyar, O. Resto, R. Perez, M. Gomez, and S.Z. Weisz. Accepted for publication in *Thin Solid Films*.
6. Auger Electron Spectroscopy for Quantitative Analysis. A. Many, Y. Goldstein, S.Z. Weisz, and O. Resto. Accepted for publication in *Appl. Phys. Letters*.

7. The Oxygen Auger Line in ZnO and MgO. S.Z. Weisz, O. Resto, Y. Goldstein, G. Yaron, and A. Many. Accepted for publication in J. Vac. Sci. & Technology.
8. Quantitative Determination of Atomic Concentrations by Auger Electron Spectroscopy. Y. Goldstein, A. Many, S.Z. Weisz, and O. Resto. Accepted for publication in J. Vac. Sci. & Technology.

Presentations

1. Alloying Effects on the Optical Absorption Edge and Photoconductance of RF Sputtered $a\text{-Sn}(x)\text{Si}(1-x)$. S.Z. Weisz, O. Resto, and R. Perez. American Physical Society Meeting, New York, March 1987; Bull. Am. Phys. Soc. **32**, 678 (1987).
2. Optical and Electrical Properties of Hydrogenated Amorphous Semiconductor Alloys. S.Z. Weisz. Short School and Workshop "Material Science, Energy and Development" Mona, Jamaica, April 1987.
3. Alloying Effects on the Infrared Absorption Studies in $a\text{-Si}_{1-x}\text{Sn}_x\text{:H}$ Films. R.S. Katiyar, O. Resto, R. Perez, M. Gomez, and S.Z. Weisz. American Physical Society Meeting, New Orleans, March 1988; Bull. Am. Phys. Soc. **33**, 475 (1988).

Scientific personnel supported by this project and degrees awarded.

1. Zvi S. Weisz, Project Director
2. Manuel Gomez, Principal Investigator
3. James Muir, Principal Investigator
4. Yehuda Goldstein, Research Associate
5. Raul Perez, Graduate Student, Finished Ph.D. 1988
6. Jose Penalbert, Graduate Student,
7. Melvin Rodriguez, Graduate Student,

Apendixes

LOW ENERGY HYDROGEN-ION IMPLANTATION ON THERMALLY TREATED ZnO SURFACES

G. YARON, J. LEVY, A. MANY, and Y. GOLDSTEIN
The Racah Institute of Physics, The Hebrew University, Jerusalem 91904, Israel

and

S. Z. WEISZ and O. RESTO
Department of Physics, University of Puerto Rico, Rio Piedras, PR 00931

(Received 16 August 1985; accepted in revised form 7 November 1985)

Abstract—Studies are reported of ZnO surfaces prepared by a three-stage implantation procedure consisting of: (1) bombardment with a 100-eV hydrogen-ion beam of an insulating sample held at 200°C, a process that introduces a very high surface density of free electrons; (2) annealing at 300°C, which restores the initial insulating state of the surface, suggesting loss of all memory of the preceding implantation; and, finally, (3) re-bombardment with 100-eV ions, but now while the sample is kept at room temperature. The surfaces so produced are totally different from those reported previously in which only the last implantation stage had been applied. In addition to the narrow, electron-rich layer resembling very closely the accumulation-like layer observed on the latter surfaces, a second, much wider electron-rich layer also forms. The first layer, extending to about 20 Å below the surface proper, contains hydrogen donors which are fully ionized down to at least 10 K. The second layer is several thousand angstroms wide and the hydrogen donors in it are only partially ionized at room temperature, becoming completely unionized at 100 K. The enormous penetration range of the implanted hydrogen, as evidenced by the thickness of the wide layer, is very difficult to account for. Equally difficult to explain is the marked difference in the characteristics of the hydrogen donors in the narrow and wide layers. Some suggestions concerning these rather puzzling observations are put forward but at this stage they are largely of a speculative nature.

Keywords: ZnO, surface, hydrogen, ion implantation, electrolyte.

INTRODUCTION

ZnO is an ideal medium for studying low-energy hydrogen-ion implantation. Instead of detecting the implanted hydrogen species directly, a fairly difficult task, one can derive their properties and spatial distribution beneath the surface by measurements of transport and space-charge characteristics of the free electrons originating from the donors introduced by the implanted hydrogen.

In previous papers [1, 2], we reported on the properties of (0001) ZnO surfaces bombarded by 100-eV hydrogen ions. The implanted ions, consisting mostly of protons, were shown to penetrate up to a depth of 10–20 Å beneath the bombarded surface. The protons act as fully ionized donors, the donor levels effectively lying at least 1.5 eV above the conduction-band edge. They give rise to a highly conducting layer of comparable depth and of surface electron densities of up to $2 \times 10^{14} \text{ cm}^{-2}$. Such narrow layers resemble closely "ordinary" accumulation layers on ZnO surfaces [3–5] obtained, for example, by exposing the surface to atomic hydrogen [6–10]. The implanted layers, just as ordinary strong accumulation layers, thus constitute a quantized two-dimensional electron gas system. The important advantage of the implanted over the ordinary accumulation layers, however, is that they are completely inert to oxygen and, in fact, remain practically intact even at room air. This unique feature is

very advantageous in the study of two-dimensional electron gas systems.

In the course of these measurements we encountered, rather accidentally, a most surprising phenomenon. Starting with an insulating ZnO sample, hydrogen implantation was usually effected while the sample was kept at room temperature. This will be referred to as "simple implantation". If, on the other hand, the hydrogen implantation (at room temperature) is preceded by implantation at 200°C (to be referred to as "hot implantation") and annealing at 300°C, a surface of totally different properties results. This is so in spite of the fact that the annealing is found to restore the initial insulating state of the surface, thus appearing to wipe out all memory of the previous hot implantation. In addition to a narrow accumulation-like layer, very similar to that produced by simple implantation, a wide conducting layer several thousand angstroms thick also forms. Some 80 percent of the implanted hydrogen species are found to reside in the wide layer. Moreover, the donor levels introduced by the implanted hydrogen in this layer lie *below* the conduction-band edge and are similar to other shallow donor levels commonly encountered in bulk ZnO [11, 12].

The enormous penetration range of the majority of the implanted hydrogen in surfaces produced by the three-stage implantation procedure just described poses a difficult question. It is about one hundred times larger than expected on theoretical grounds [13–15] and can

only originate from some channeling process [16]. Such long-range channeling was found, however, to be practically absent in the case of simple implantation [2]. One is therefore led to conclude that the first two stages, those of hot implantation and annealing, are responsible, in an as yet unknown fashion, for making the surface region so transparent to the hydrogen-ion beam in the third stage of the implantation procedure. Another puzzling feature is the drastically different donor characteristics of the implanted hydrogen in the narrow and wide layers.

The results to be presented were obtained from conductivity and Hall effect measurements, from experiments of calibrated chemical etching and from studies of the space-charge characteristics using the ZnO/electrolyte system. The combined data give a consistent picture of the properties outlined above of the three-stage implanted surface. They shed little light, however, on some of the puzzling questions posed by these findings.

EXPERIMENTAL

The samples were cut from ZnO single crystals made insulating either by Li doping or by thermal diffusion of oxygen. The high resistivity is essential in order to minimize the parallel bulk conductance when performing surface transport measurements. Typically, the sample dimensions were $10 \times 2 \times 1 \text{ mm}^3$ with the hexagonal *c* axis perpendicular to the large surfaces. The measurements were carried out on the "oxygen" ($(000\bar{1})$ face, all other faces being masked by ceramic glue. The surface was lapped with a diamond paste to a flatness of $1 \mu\text{m}$. It was subsequently etched in HCl and then chemically polished in a 2% bromine methanol solution.

Tantalum sheets pressed on sputtered vanadium strips at the two ends of the sample were used as current contacts. Four tungsten wires, pressed upon small sputtered vanadium dots, two on each side of the sample, served as voltage probes. The sample was mounted in an ultra-high vacuum (UHV) chamber where the sample temperature could be varied between 10 K and 800 K. For Hall-effect measurements, magnetic fields (up to 2000 Gauss) were applied by an external electromagnet. Such measurements were employed for determining the surface mobility and surface electron density and their variation with temperature in the surfaces under study. Argon sputtering and hydrogen implantation were carried out with a Varian ion gun (energy range of 0–3000 eV).

Prior to all measurements, the surface was cleaned by repeated cycles of 1000-eV argon-ion bombardment, at a pressure of 5×10^{-3} Torr, and subsequent annealing at 400°C. During the sputtering, ultra pure argon gas was cycled through the system at a rate of 10 l/sec, corresponding to an effective change of the argon gas in the vacuum chamber every 5 sec.

Hydrogen implantation was effected by bombarding the surface with 100-eV hydrogen ions, at a hydrogen

pressure of 5×10^{-5} Torr maintained by continuous cycling of ultra pure hydrogen gas. As discussed previously [1], although the hydrogen-ion beam consists predominantly of H_2^+ , the implanted species are mostly protons. Very likely, the H_2^+ ions dissociate upon impact at the surface and protons of approximately half the beam energy penetrate the crystal. In any case, the penetration depths of 50-eV protons and of 100-eV H_2^+ ions are expected to be comparable [14], some 10–20 Å below the surface.

The implantation procedure used in the present investigation consists of three stages: in the first, the 100-eV hydrogen-ion bombardment is carried out for a few minutes while the sample is being held at a temperature of 200°C (hot implantation). Just as in the case of simple implantation used previously [1, 2], the implanted protons give rise to a high surface conductivity of about 10^{-3} mho/square, corresponding to a surface electron density of 10^{16} cm^{-2} . In the second stage, the sample is annealed in vacuum for five minutes at a temperature of 300°C, as a result of which its conductivity drops typically to 5×10^{-4} mho/square, 2–3 orders of magnitude lower than that of the hot-implanted surface (electron density of about 10^{11} cm^{-2}). The surface region thus appears to have returned to its initial, high-resistivity state. As will be shown below, however, an irreversible change has taken place. In particular, subsequent cold implantation of 100-eV hydrogen ions, which constitutes the third stage of the present implantation procedure, now results in penetration depths of several thousand angstroms.

The penetration range of the implanted protons was estimated by calibrated chemical etching. After the implantation, the sample was removed from the UHV chamber and chemically etched in a highly diluted aqueous solution of HCl (1 part of concentrated HCl in 100 parts of water) kept at 15°C. Conductivity and Hall effect measurements were carried out at suitable intervals. The rate of surface layer removal for such etching conditions was determined to be 5–10 Å per second [2].

Another technique for assessing the depth profile of the implanted proton donors employed the ZnO/electrolyte system [2, 17, 18]. Basically, the experimental arrangement consists of a large-area platinum electrode and the ZnO sample under study, both immersed in a $\text{Ca}(\text{NO}_3)_2$ electrolyte. Only a small area (about 1 mm^2) of the ZnO surface is in contact with the aqueous solution, the rest of the surface, as well as the ohmic metal contacts and wire leads, being masked. By biasing the electrolyte with respect to the semiconductor, space charge can be induced at the semiconductor surface by virtue of the essentially blocking nature of the semiconductor/electrolyte interface. Such blocking prevents, or at least minimizes, charge leakage between the two phases [19, 20]. By using special pulse techniques [17, 18], charge leakage across the interface can be eliminated or else its undesirable effects completely taken into account in deriving the relation between the surface space-charge density and the surface potential

barrier. A short (1-10 μ sec) voltage pulse applied between the Pt electrode and the ZnO sample is used to charge up the space-charge capacitance at the ZnO surface. The voltage drop between the Pt electrode and the semiconductor bulk, measured just after the termination of the pulse, represents, to a good approximation, the change in the barrier height V , across the space-charge layer induced by the applied pulse. The corresponding change in the space-charge density Q_s can be readily obtained from the voltage developed across a large series capacitor, again at the termination of the pulse. In accumulation or other electron-rich layers, the space charge is made up predominantly of free electrons [21] so that $Q_s = -qN_s$, where N_s is the surface electron density and q is the absolute magnitude of the electronic charge.

In ZnO, extremely strong accumulation layers can be induced at the surface by this technique [3, 4]. In the present case, the proton-implanted ZnO surface already contains a very high free-electron density and negative pulses applied to the Pt electrode would repel electrons away from the surface. For sufficiently high pulse amplitudes, the entire electron population can be depleted. Positive pulses, on the other hand, enhance the existing high surface electron density.

The purpose of measuring the variation of $N_s - N_{s0}$ with $V_s - V_{s0}$ (where N_{s0} and V_{s0} are the initial values of N_s and V_s) is two-fold. First, it yields directly the total surface electron density N_s at the implanted surface and hence the total density of the implanted proton donors. Secondly and more important, it provides valuable information on the depth profile of the donors, as will be discussed below. It should be pointed out that in the samples studied, neither deep lying bulk traps [18] nor surface states are present to any significant amount to interfere with the measurements.

RESULTS

The measurements were carried out on (0001) surfaces of ZnO that have undergone the three-stage implantation procedure described above. After completion of the third stage, consisting of cold implantation with 100-eV hydrogen ions, another annealing at 300°C (second stage) and subsequent cold implantation (third stage) result in a surface of practically identical properties. This was also found to be the case even if the second and third stages were repeated several times. On the other hand, the first two stages (hot implantation and annealing) introduce an irreversible change, and the truly virgin state of the surface could not be restored other than by chemically etching away a few micrometers of the surface region.

Results of conductivity and Hall effect measurements are shown in Figs. 1 and 2. Prior to the measurements, oxygen has been introduced into the UHV system in order to remove traces of an ordinary accumulation layer that always forms as a by-product of hydrogen implantation. Such an accumulation layer presumably originates from the presence of atomic hy-

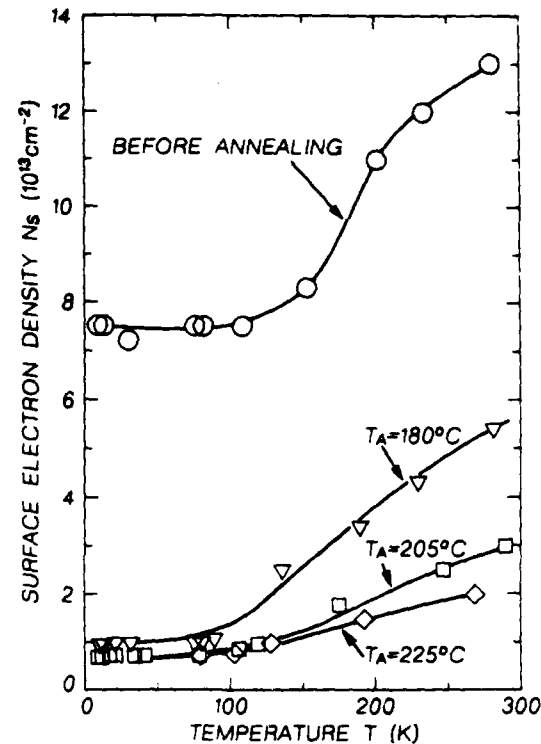


Fig. 1. Surface electron density as function of temperature for a three-stage implanted surface before and after annealing at different temperatures as marked.

drogen [6-10], produced by the hot filament of the ion gun from the ambient (molecular) hydrogen. This layer is readily destroyed by exposure to oxygen. In contrast, the free electron layer associated with the *implanted* hydrogen is completely inert to oxygen.

The temperature dependence of the surface electron density N_s in the implanted layer is shown in Fig. 1. The upper curve (labelled "before annealing") has been obtained right after the three-stage implantation procedure. N_s is seen to decrease monotonically as the temperature is lowered down to about 100 K. At this temperature, some 5×10^{13} electrons per cm^2 have been frozen out, while the rest (about $7.5 \times 10^{13} \text{ cm}^{-2}$) remain free down to at least 10 K, the lowest temperature reached in our experiment. The curve below (marked " $T_A = 180^\circ\text{C}$ ") was obtained after the sample has been annealed at 180°C for two minutes. It is seen that such annealing has lowered N_s by about $7 \times 10^{13} \text{ cm}^{-2}$ and that almost all the electrons left in the sample now freeze at about 100 K, the unfreezing component having been practically eliminated. The other two curves in Fig. 1 were obtained after a two-minute annealing at 205°C and at 225°C . Such annealing reduces N_s still further, but now it is the freezing component that is mainly affected. As will be discussed below, the unfreezing component of the surface electron density originates from fully ionized hydrogen donors situated in a narrow layer, some 20 Å thick, whereas the freezing component arises from partially ionized hydrogen do-

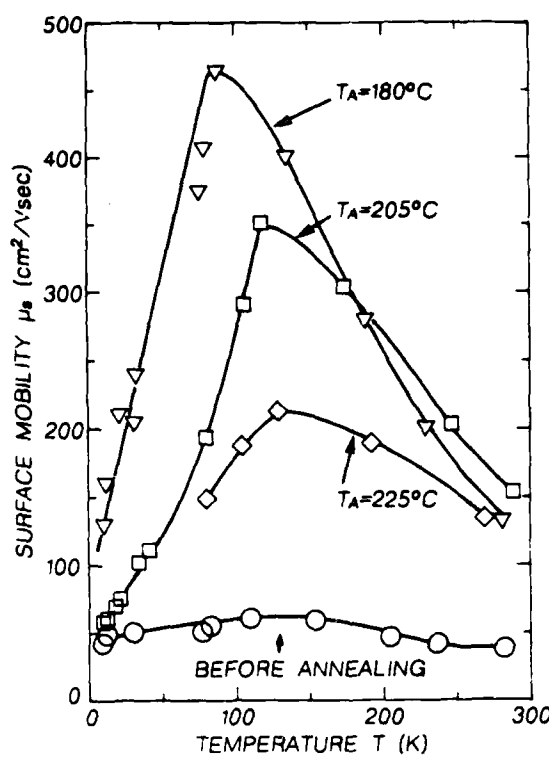


Fig. 2. Surface mobility as function of temperature for the same implanted surface as that in Fig. 1.

nors distributed over a layer about one hundred times wider.

The temperature dependence of the surface mobility μ_s for the same implanted surface is displayed in Fig. 2. It is seen that before annealing, μ_s is almost temperature-independent, varying between 40 and 60 cm^2/Vsec . After a two-minute annealing at 180°C , the behaviour of the surface mobility changes drastically. In the first place, the room-temperature value of μ_s increases from 40 to $130 \text{ cm}^2/\text{Vsec}$. More significantly, however, μ_s increases upon cooling up to the peak value of $460 \text{ cm}^2/\text{Vsec}$, reached at 110 K . It then decreases as the temperature is lowered further. A similar behaviour characterizes the temperature dependence of μ_s after a two-minute annealing at 205°C and at 225°C . However, the peak value decreases and its position shifts to higher temperatures the higher the annealing temperature.

The temperature dependence of both the surface mobility and of the freezing component of the surface electron density is typical to electrons in bulk ZnO [5, 11, 12, 22-25] and, as will be discussed below, it suggests that a substantial fraction of the implanted hydrogen penetrates quite deep below the surface. This behaviour is to be contrasted with the analogous results reported previously [1] for surfaces produced by simple implantation (with no prior hot implantation and annealing). On such surfaces, no electron freeze-out was found to take place down to at least 10 K . Also, annealing at comparable temperatures (around 200°C)

produced only minor changes in the surface mobility which, furthermore, did not exhibit any peak at low temperatures.

The results of Fig. 1 were used to evaluate the temperature dependence of the freezing component of the surface electron density N_s . This component is obviously given by the difference between the total electron density N , and the density $N_s(10 \text{ K})$ at 10 K . This difference is plotted in Fig. 3 on a semi-log scale against $1000/T$ for the four measurement cycles in Fig. 1. All curves are seen to be linear and parallel. If we describe these curves by exponential functions of the form $\exp(-E'/kT)$, where E' is some activation energy and k is Boltzmann's constant, then the common slope yields $E' = 0.035 \text{ eV}$. For a non-degenerate free-electron layer, $2E'$ would have represented the energy depth of the hydrogen donors below the conduction-band edge. Actually, however, the layer is somewhat degenerate and the depth of the donors comes out to be about 0.05 eV (see below).

Results obtained by conductivity and Hall effect measurements (at room temperature) during calibrated chemical etching are displayed in Fig. 4. Here the surface electron density N_s on a three-stage implanted surface is plotted against the depth of the etched-away layer: Following a rapid drop taking place after the removal of some $10-20 \text{ \AA}$ (corresponding to an etching time of two-three seconds), N_s is seen to decrease much

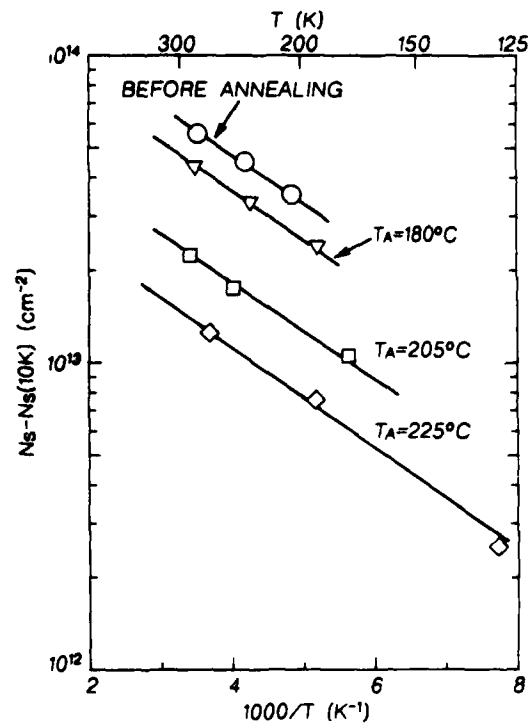


Fig. 3. Semilog plot of the surface electron density with respect to the density at 10 K (the freezing component of the electron density) as function of $1000/T$ for the same surface as in Figs. 1 and 2.

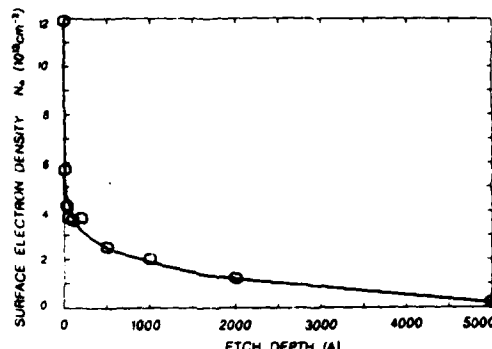


Fig. 4. Surface electron density as function of depth of the etched-away layer for a three-stage implanted surface.

more slowly with etch depth, extending to several thousand angstroms. A surface layer about 5000 Å thick has to be etched away in order to eliminate completely the free electrons introduced by the implanted hydrogen donors.

Finally, we present results of space charge capacitance measurements, carried out in the ZnO/electrolyte system. In Fig. 5 the absolute value of the change in surface electron density $|N_s - N_{s0}|$ is plotted against the change in surface potential barrier $V_s - V_{s0}$. The left-hand side of the figure (negative $V_s - V_{s0}$) corresponds to measurements performed with negative pulses (i.e. electrons repelled away from the surface, $N_s - N_{s0}$ negative), while the right-hand side—to positive pulses (electrons attracted to the surface, $N_s - N_{s0}$ positive). For negative pulses, the points exhibit two different regimes. In the first, extending to about -1.5 V, $|N_s - N_{s0}|$ rises very steeply to a value of about $4 \times 10^{13} \text{ cm}^{-2}$. As will be shown momentarily, this can be attributed to the expulsion from the sample of those electrons originating from the proton donors situated in the narrow layer beneath the surface. The space-charge capacitance C_x associated with these electrons is given by the product of the above density and the electronic charge divided by 1.5 Volts, which comes to about $4 \mu\text{F}/\text{cm}^2$. The effective charge distance [21] L_c , i.e., the depth below the surface of the center of charge, is given by $L_c = \kappa \epsilon_0 / C_x$, where κ ($= 8.5$) is the relative dielectric constant of ZnO and ϵ_0 is the permittivity of free space. Using this relation one derives the value of 20 \AA for L_c , comparable to the effective charge distance (15 \AA) for an ordinary accumulation layer of the same surface electron density [4]. One thus concludes that the implanted hydrogen species in the narrow layer do indeed lie within about 20 \AA from the surface. The second regime in Fig. 5, between -1.5 V and -10 V, represents expulsion of electrons originating from much more deeply implanted hydrogen donors. The two curves in the figure are theoretical. The solid curve was calculated by numerical integration of Poisson's equation, taking into account the hydrogen donor distributions in both the narrow and wide layers. The narrow layer is represented [2] by a Gaussian donor distribution

peaked 10 \AA below the surface and having a standard deviation of 20 \AA . The wide layer below it is represented by a constant donor concentration of 10^{19} cm^{-3} . (The choice of this value is considered in the Discussion section below.) Using a constant concentration is a very good approximation because in the V_s range attained experimentally ($V_s - V_{s0}$ between -1.5 V and -10 V), only a small section of the wide layer is depleted of its electrons. (In order to deplete the electrons from the *entire* wide layer, a change of -1000 V or so in $V_s - V_{s0}$ would have been required!) The two distributions are seen to account well for the experimental points. The dashed curve was calculated for the case in which donors are present only in the narrow layer, as is applicable to surfaces produced by simple implantation [2]. As expected, this curve coincides with the solid curve up to $V_s - V_{s0} = -1.5$ V. It then levels off because in this case there is no wide layer of donors from which electrons can be depleted. For positive pulses, $N_s - N_{s0}$ is seen to rise steeply with $V_s - V_{s0}$ throughout. In this polarity, the existing narrow, accumulation-like layer is made ever stronger by the applied pulses. It is to be noted that close to the origin ($V_s - V_{s0} = 0$), the behaviour is symmetrical for the two polarities. This is only to be expected [21] because the initial state of the implanted surface already contains a very strong accumulation layer.

DISCUSSION

ZnO surfaces produced by the three-stage implantation procedure are drastically different from those prepared by simple implantation. In both procedures,

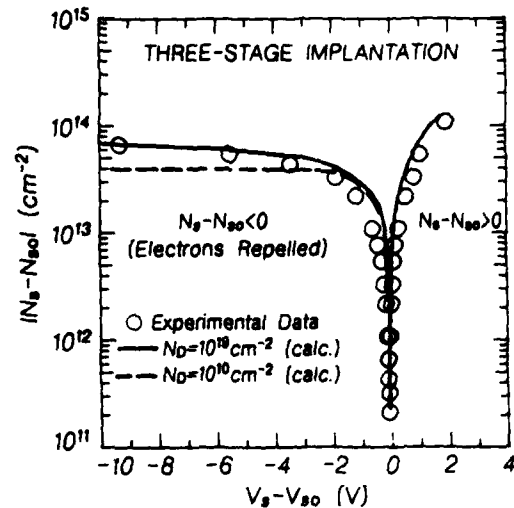


Fig. 5. Change $N_s - N_{s0}$ in surface electron density as function of change $V_s - V_{s0}$ in surface potential barrier for a three-stage implanted surface. (N_{s0} is the surface electron density on the implanted layer and V_{s0} is the corresponding potential barrier at the surface.) The circles represent data measured in the ZnO/electrolyte system. The curves were calculated for two different donor concentrations in the wide layer, as noted in the figure.

the last stage, that of cold implantation of 100-eV ions, is identical. The only difference is that in the present procedure this stage is preceded by hot (200°C) hydrogen implantation followed by annealing at 300°C. The general picture that emerges from the data presented is that while a fraction of the implanted hydrogen is situated 10–20 Å beneath the surface, just as for the case of simple implantation, most of the hydrogen species following the three-stage implantation penetrate up to a depth of several thousand angstroms. The surface region thus consists of a narrow layer of a very high volume concentration of hydrogen and a much wider layer of lower volume concentration below it. As will be discussed in a moment, the hydrogen donor levels in the narrow layer lie well above the conduction-band edge so as to remain fully ionized down to very low temperatures. In the wide layer, on the other hand, the donor levels are below the conduction-band edge and at room temperature only about one fourth of them are ionized.

The properties of the narrow layer are best displayed by the space-charge capacitance measurements using the ZnO/electrolyte system. From Fig. 5 one sees that some 4×10^{13} electrons per cm^2 are characterized by an effective charge distance L_c of about 20 Å, typical of an ordinary accumulation layer of the same surface electron density [4]. Thus, just as in the case of simple implantation, a narrow, accumulation-like layer forms at the surface. Such layers are highly degenerate, with the conduction-band edge at the surface lying about 1.5 eV below the Fermi level [4]. This can only come about if the donor levels are energetically removed by at least that amount *above* the conduction-band edge. Under these conditions, no electron freeze-out should take place down to very low temperatures and undoubtedly the unfreezing component of the surface electron density in Fig. 1 involves the electrons in the narrow layer. This is further supported by the observation that brief annealing at 180°C is sufficient to eliminate this layer (see Fig. 1), similarly to the case of surfaces produced by simple implantation [1], where the implanted layer has been established to be very narrow. The space-charge capacitance measurements are less sensitive to the presence of the wide electron layer because only a small portion of this layer can be depleted for $V_s - V_{so} = -10$ V, the highest swing attained in our experiment. Yet, a fairly good quantitative agreement has been obtained between the experimental points and the theoretical curve calculated by taking into account the donor distribution in both the narrow and wide layers (see Fig. 5). The calibrated etching measurements, on the other hand, are particularly suitable for monitoring the wide electron layer. The plot of the surface electron density against etch depth (Fig. 4) immediately reveals this layer to be several thousand angstroms thick.

The mere fact that a fraction of the free electrons in the implanted surface is observed to freeze out at low temperatures (see Fig. 1) points to two conclusions: firstly, that these electrons originate from donors that lie energetically *below* the conduction-band edge and, secondly, that the donors are distributed over a rela-

tively wide layer. An estimate of the donor level energy and a lower limit for the width of this layer can be obtained on the basis of the following simple reasoning. Consider for simplicity a uniform layer. The electron volume concentration n in this layer is given by

$$n = \int_{E_c}^{\infty} N(E) \{1 + \exp[(E - E_F)/kT]\}^{-1} dE, \quad (1)$$

where E_c is the conduction-band edge and E_F is the Fermi level. In ZnO, the conduction band is parabolic [4] up to at least 2 eV above E_c , so that the density of states $N(E)$ is given by

$$N(E) = (4\pi/h^3)(2m_n)^{3/2}(E - E_c)^{1/2}, \quad (2)$$

where m_n is the isotropic effective mass and h is Planck's constant. At the same time, since the freezing electrons originate entirely from donors introduced by the implanted hydrogen, n must also be equal to

$$n = N_D \{1 + \exp[(E_D - E_F)/kT]\}^{-1}, \quad (3)$$

where N_D is the donor concentration and E_D is the donor energy. Equating eqns (1) and (3) yields an implicit relation between n and T , involving $E_c - E_D$ and N_D as parameters. Numerical solution shows that even if one takes the unreasonably high value of $5 \times 10^{21} \text{ cm}^{-3}$ for N_D (hydrogen concentration of about 10 percent), n does not exceed $2 \times 10^{19} \text{ cm}^{-3}$. (The highest hydrogen concentration obtained in the narrow layer is only $5 \times 10^{20} - 1 \times 10^{21} \text{ cm}^{-3}$, corresponding to 10^{14} electrons per cm^2 spread over a layer 10–20 Å thick.) Physically, the reason for such a low value of n/N_D is that the Fermi level in the degenerate layer lies above the donor levels. The electron concentration is then insensitive to the value of N_D : increasing N_D tends to raise E_F and thus to increase n but this has the opposite effect of lowering the degree of ionization of the donors. Accordingly, since the room-temperature surface density of the freezing electrons is $5 \times 10^{13} \text{ cm}^{-2}$, it follows that the 2×10^{19} (or, very likely, much less) electrons per cm^3 must be spread over a layer at least 250-Å thick.

Actually, this is an over-cautious estimate of the lower limit. The etching experiments indicate that the wide layer is about ten times thicker so that the average room-temperature electron concentration in it is of the order of only $2 \times 10^{18} \text{ cm}^{-3}$. In order to account for the observed temperature dependence of the freezing component of the surface electron density shown in Fig. 3, one must take a value of $8 \times 10^{18} \text{ cm}^{-3}$ for the donor concentration N_D and an energy depth $E_c - E_D$ of 0.05 eV for the donor levels. Thus, only about one fourth of the implanted hydrogen in the wide layer is ionized at room temperature. It follows, then, that altogether some 80 percent of the implanted hydrogen species are located within the wide layer.

The estimated energy of the donor levels is close to the ionization energies reported for other donor levels in bulk ZnO [11, 12]. Also, after annealing at 180°C, which eliminates the narrow layer, the temperature

dependence of the mobility (see Fig. 2) is very similar to that of bulk electrons in ZnO [5, 11, 12, 22-25]. Annealing at higher temperatures gradually removes electrons from the wide layer as well, until eventually the insulating state of the surface region is restored. The question that arises is where did the hydrogen donors disappear to. Although a fraction of the implanted hydrogen species may have diffused out into the vacuum, the remainder (half or thereabout) would be expected to diffuse inwards or in any case remain in the sample. One is therefore led to conclude that, after annealing, the implanted hydrogen species cease, first in the narrow layer and at higher temperatures in the wide layer as well, to act as shallow donors. Such transformation may come about from hydrogen diffusion or displacement into sites in which the ionization energy of the hydrogen atoms becomes too large. Altogether, it appears then that the implanted hydrogen can occupy three different lattice sites. In one site, situated at the narrow layer, hydrogen introduces donor levels lying well above the conduction-band edge. In another site, located within the wide layer, hydrogen gives rise to shallow donor levels below the band edge. And finally, a third site, just discussed, in which the donor levels are sufficiently deep to remain unionized, at least at room temperature. The nature of these sites is not clear to us at present.

The enormous penetration depth of hydrogen (implanted at room temperature) is most surprising. It is about a hundred times larger than the range expected from stopping power considerations [13-15] or from room-temperature diffusion [26]. Both these processes should yield a range of about 10 Å, which was actually observed in the case of simple implantation [1, 2]. True enough, during the process of hot implantation (first stage), hydrogen diffuses to a depth of thousands of angstroms [26]. However, the annealing in vacuum at 300°C (second stage) restores the initial insulating state of the surface, indicating that the previously implanted hydrogen species have either been removed from the sample or else displaced into sites in which they no longer act as shallow donors. The question to be answered is what makes such a surface so transparent to the newly implanted hydrogen ions during the third stage of cold (room-temperature) implantation. It should be noted that even in the case of simple implantation some of the hydrogen species penetrate to a comparable depth [2] but only less than one percent of the implanted hydrogen is involved. Very likely, such penetration is effected by channelling through the large open channels that exist along the hexagonal *c* axis of ZnO, by virtue of the substantial difference between the radii of the zinc and oxygen ions [27]. One might speculate that hot implantation (and subsequent annealing) widens these channels, for example by reducing lattice oxygen and out diffusion of OH radicals or water molecules. It is not clear, however, whether this mechanism could enable some 80 percent of the hydrogen species implanted subsequently (at room temperature) to penetrate thousands of angstroms below the surface. Further work is required to resolve

this issue which, at this stage, is much of a mystery to us.

Acknowledgments—This work was supported in part by The National Council for Research and Development, Israel and G. F. K. Karlsruhe, Germany and in part by U.S. Army Research Office Grant DAAG29-84-G-0059.

REFERENCES

1. Yaron G., Many A. and Goldstein Y., *J. Appl. Phys.* **58**, 3508 (1985).
2. Yaron G., Levy J., Goldstein Y. and Many A., *J. Appl. Phys.* (to be published).
3. Eger D., Many A. and Goldstein Y., *Phys. Lett.* **A55**, 197 (1975); *Surf. Sci.* **58**, 18 (1976).
4. Eger D. and Goldstein Y., *Phys. Rev.* **B19**, 1089 (1979).
5. Grinshpan Y., Nitzan M. and Goldstein Y., *Phys. Rev.* **B19**, 1098 (1979); Nitzan M., Grinshpan Y. and Goldstein Y., *Phys. Rev.* **B19**, 4107 (1979).
6. Heiland G., Mollwo E. and Stockmann F., *Solid State Phys.* **8**, 193 (1958).
7. Heiland G., *J. Phys. Chem. Solids* **6**, 155 (1958).
8. Heiland G. and Kunstmänn P., *Surf. Sci.* **13**, 72 (1969).
9. Shapira Y. and Lichtman D., *J. Vac. Sci. Technol.* **13**, 615 (1976).
10. Gersten J. I., Wagner L., Rosenthal A., Goldstein Y., Many A. and Kirby R. E., *Phys. Rev.* **B29**, 2458 (1984).
11. Littbarski R., in *Zinc Oxide*, by Hirschwald W., Bonaszewicz P., Ernst L., Grade M., Hoffmann D., Krebs S., Littbarski R., Neumann G., Grunze M., Kolb D. and Schulz H. J., Vol. 7 of *Current Topics in Materials Science* (Edited by E. Kaldus), p. 212. North-Holland, Amsterdam (1981).
12. Hutson A. R., *J. Phys. Chem. Solids* **8**, 467 (1959).
13. Schiott H. E., Kgl. Dansk Vidensk. Selsk., *Mat. Fys. Medd.* **35**, No. 9. (1966).
14. Schiott H. E., *Rad. Effects* **6**, 107 (1970).
15. Oen O. S. and Robinson M. T., in *Applications of Ion Beams to Materials*, 1975. (Edited by G. Carter, J. S. Colligon, and W. A. Grant). Conference No. 28, 329 Institute of Physics, London (1976).
16. Mayer J. W., Eriksson L. and Davies J., *Ion Implantation in Semiconductors. Silicon and Germanium*. Academic Press, New York (1970).
17. Trokman S., Ph.D. Thesis, Hebrew University of Jerusalem, Israel (1978); Many A. and Balberg I., *Investigation of Semiconductors by the Electrolyte/Solid System*. Final Report of United States-Israel Bi-National Science Foundation, No. 1340 (Unpublished) (1980).
18. Trokman S., Many A., Goldstein Y., Heiland G., Kohl D. and Moermann H., *J. Phys. Chem. Solids* **42**, 937 (1981).
19. Rose A., *Concepts in Photoconductivity and Allied Problems*. Wiley-Interscience, New York (1963).
20. Morrison S. R., in *Progress in Surface Science* (Edited by S. G. Davison), Vol. 1, p. 105. Pergamon, Oxford (1971); Morrison S. R., *The Chemical Physics of Surfaces*. Plenum Press, New York (1977).
21. Many A., Goldstein Y. and Grover N. B., *Semiconductor Surfaces*. North Holland, Amsterdam (1965).
22. Hausman A. and Teuerle W., *Z. Phys.* **259**, 189 (1973).
23. Wagner P. and Helbig R., *J. Phys. Chem. Solids* **35**, 327 (1974).
24. Utsch B. and Hausmann A., *Z. Phys.* **B21**, 27 (1975).
25. Hausmann A. and Utsch B., *Z. Phys.* **B21**, 217 (1975).
26. Thomas D. G. and Lander J. J., *J. Chem. Phys.* **25**, 1136 (1956).
27. Neumann G., in *Zinc Oxide*, by Hirschwald W., Bonaszewicz P., Ernst L., Grade M., Hoffmann D., Krebs S., Littbarski R., Neumann G., Grunze M., Kolb D. and Schulz H. J., Vol. 7 of *Current Topics in Materials Science* (Edited by E. Kaldus), p. 153. North Holland, Amsterdam (1981).

SPACE CHARGE AND SURFACE STATE CHARACTERISTICS OF THE SILICON/ELECTROLYTE INTERFACE

M. WOLOVELSKY, J. LEVY, Y. GOLDSTEIN and A. MANY

Racah Institute of Physics, The Hebrew University, Jerusalem 91904, Israel

and

S.Z. WEISZ and O. RESTO

Department of Physics, University of Puerto Rico, Rio Piedras, Puerto Rico 00931, USA

Received 26 July 1985; accepted for publication 17 December 1985

The essentially blocking nature of the silicon/electrolyte (S/E) interface enables charge to be induced electrostatically at the interface by an applied bias. The use of pulsed rather than DC biases provides a fairly detailed picture of the silicon interface. The results reported here concern the silicon space-charge layer, localized states at the S/E interface and charge leakage across the interface. As to the first, evidence is presented that strong, quantized accumulation layers of excess surface-electron densities as high as 10^{14} cm^{-2} can be induced at the Si surface, an order of magnitude larger than can be attained in Si inversion layers in MOS structures. The localized states are of total density of about 10^{12} cm^{-2} and of capture cross sections around $5 \times 10^{-18} \text{ cm}^2$. The nature of these states is not known; they are probably fast surface states at the silicon surface. The charge leakage occurs under strong accumulation conditions, very likely by electron tunneling from the silicon electrode into the electrolyte. It takes place practically instantaneously, but the leaked charge remains stored near the interface for a considerable time. Some suggestions concerning this unexpected behavior are put forward.

1. Introduction

The investigation of silicon surfaces reported in this paper is based on the semiconductor/electrolyte (S/E) system. The use of special pulse techniques developed in this laboratory [1,2] appears to circumvent to a large extent electrochemical processes, permitting the derivation of the physical characteristics of the silicon surface with minimal involvement of the rather complex surface chemistry. A short-duration pulse applied to the S/E system charges up the interface region. The discharge process following the pulse termination is usually found to consist of two distinctly different and easily resolved components. The first and dominant component is very fast, lasting typically a few microseconds or less. The second component, when present, is much

0039-6028/86/\$03.50 © Elsevier Science Publishers B.V.
(North-Holland Physics Publishing Division)

slower, in the millisecond range. We interpret the fast component as representing the discharge of free electrons in the silicon space-charge layer, whereas the slow component is attributed to thermal release of electrons trapped in localized states back into the conduction band. On this premise, we find that extremely strong electron accumulation layers, of surface densities as high as 10^{14} cm^{-2} , can be induced in the silicon space-charge layer, compared to at most 10^{13} cm^{-2} attainable in Si inversion layers in MOS structures [3-5]. Such layers, which are characterized by a width of about 10 Å, constitute nearly perfect two-dimensional electron gas systems. A study of quantization effects in these layers should therefore prove highly interesting. The accent in the present investigation is placed, however, on the interface states and on the processes of charge transfer across the S/E interface.

The interface states, of total density around 10^{12} cm^{-2} , can reversibly exchange charge with the silicon space-charge layer and are very likely ordinary surface states at the silicon surface. As such, they are uniformly distributed in an energy interval of about 0.2 eV, situated half way between the conduction-band edge and the midgap. Analysis of the interaction kinetics between the interface states and the conduction band yields capture cross sections in the neighborhood of $5 \times 10^{-18} \text{ cm}^2$. The states are thus of the "fast" type and are probably located very close to the silicon surface [6].

The S/E interface is not perfectly blocking and some charge leaks between the two phases, especially when strong accumulation layers are induced at the Si surface. The characteristics of the leakage process are of particular interest. The leakage charge is found to increase exponentially with increasing potential barrier height, i.e. with increasing interface field. This is a strong indication that some tunneling mechanism across the interface is involved. The leakage can take place practically instantaneously (in less than 0.1 μs), but the leaked charge remains stored at or very close to the interface for a considerable time. A possible mechanism that may account for this rather surprising aspect of the leakage process is considered.

2. The space-charge layer and the semiconductor/electrolyte interface

In this section we review briefly the characteristics of the semiconductor surface space-charge layer [6] and consider several features of the semiconductor/electrolyte system, stressing those points that are directly related to our present work. We consider a homogeneous, non-degenerate, n-type semiconductor having fully ionized donors. For depletion and accumulation layers, the surface space-charge density (per unit area) can be expressed as

$$Q_{sc} = -qN_s, \quad (1)$$

where q is the absolute magnitude of the electronic charge and N_s is the excess

surface electron density. By definition, N_s is zero under flat-band conditions, positive for accumulation layers and negative for depletion layers. The space-charge capacitance is given by

$$C_{sc} = |Q_{sc}/V_s|, \quad (2)$$

where V_s is the potential barrier height at the surface. The effective charge distance L_c , which represents the effective width of the space-charge layer, is given by the expression

$$C_{sc} = \kappa \epsilon_0 / L_c, \quad (3)$$

where κ is the relative dielectric constant of the semiconductor (11.7 for Si) and ϵ_0 is the permittivity of free space. First integration of Poisson's equation leads to

$$N_s = \pm (\kappa \epsilon_0 n_b kT / q^2)^{1/2} F_s, \quad (4)$$

where the positive sign applies to accumulation layers, the negative sign to depletion layers; n_b is the electron bulk concentration, k is Boltzmann's constant and T the absolute temperature. For parabolic conduction bands, the function F_s is given by

$$F_s = \sqrt{2} \left[(4/3)^{-1/2} \exp(w_b) F_{3/2}(v_s - w_b) - v_s - 1 \right]^{1/2}, \quad (5)$$

where $w_b = W_b/kT$, W_b being the energy separation between the Fermi level and the conduction-band edge in the bulk; $v_s = qV_s/kT$ is the so-called dimensionless barrier height; and

$$F_{3/2}(y) = \int_0^\infty x^{3/2} [1 + \exp(x - y)]^{-1} dx \quad (6)$$

is a definite integral which is available in tabular form [7].

For strong accumulation layers, in which the conduction-band edge lies well below the Fermi level, it may be necessary to replace the $F_{3/2}$ function by a more complicated integral [1] to take into account possible non-parabolicity of the bands. In our measurements in silicon, however, non-parabolicity is negligible up to the strongest accumulation layer attained ($N_s = 10^{14} \text{ cm}^{-2}$), and eq. (6) can be used throughout the range of interest.

A much more important factor that needs to be considered in strong accumulation layers is associated with the spatial confinement of the electron gas. When the effective charge distance L_c becomes comparable to or less than the de Broglie wavelength of a conduction electron, quantization effects set in. The classical calculations reviewed above may no longer be adequate, the less so the stronger the accumulation layer (larger N_s , smaller L_c). One should then solve self-consistently Poisson's and Schrödinger's equations [3,4,8,9]. Unfortunately, for silicon such calculations have been carried out [3,4] for surface electron densities up to only 10^{13} cm^{-2} , whereas the range of interest here

extends to 10^{14} cm^{-2} . For $N_s = 10^{13} \text{ cm}^{-2}$ in electron inversion layers on the (111) surface, the calculated value [3] of L_c is somewhat less than 30 Å, which is very close to the value evaluated classically [eqs. (1)-(6)] for accumulation layers of the same electron density. Since the space-charge characteristics of strong inversion and strong accumulation layers are very similar [6], one can safely conclude that the classical expressions are adequate up to at least $N_s = 10^{13} \text{ cm}^{-2}$. As to larger N_s values, one cannot say definitely, but judging from the results obtained for very strong accumulation layers on ZnO [8,9], one should not expect too large a deviation of the N_s versus V_s curve from that calculated classically.

For non-degenerate surface conditions, corresponding to depletion and weak accumulation layers, F_s can be well approximated by the simpler expression

$$F_s = \sqrt{2} [\exp(v_s) - v_s - 1]^{1/2}. \quad (7)$$

The semiconductor/electrolyte system considered here consists of a semiconductor surface in contact with an indifferent electrolyte such as an aqueous solution of a salt [KCl or Ca(NO₃)₂]. By biasing the electrolyte with respect to the semiconductor, charge can be induced electrostatically at the semiconductor surface. This is made possible by the essentially blocking nature of the S/E interface, which largely prevents charge transfer between the two phases. The induced charge is in general distributed between the surface space-charge region and surface states (if present). In the absence of a foreign layer (such as an oxide) at the semiconductor interface, the applied bias drops across three adjacent regions [6,10]: the space-charge layer at the semiconductor surface, and the Helmholtz and Gouy layers in the electrolyte. Of these three layers, the latter two are much thinner than the former, at least under pulsed bias conditions, so that practically the entire applied bias drops across the semiconductor space-charge layer. This is evidenced by space-charge capacitance measurements on metal/electrolyte interfaces [1]. Hence the measured bias represents to a very good approximation the change δV_s in barrier height V_s across the semiconductor space-charge layer. If an insulating layer is present at the semiconductor surface, the bias is distributed across both this layer and the space-charge layer, as will be discussed below.

In practice, the interface is not perfectly blocking and to a lesser or greater extent some charge leaks across the S/E interface. The leakage charge is usually insignificant when depletion layers are induced (electrolyte biased negatively with respect to the n-type semiconductor). It becomes appreciable, however, under accumulation conditions, the more so the stronger the induced accumulation layer. It is this leakage that had prevented in the past the formation of strong accumulation layers by DC biases. By employing our pulse techniques [1,2], on the other hand, it appears possible to induce extremely strong accumulation layers not only on silicon but also on a number

of other semiconductors, such as Ge and CdS [1] and ZnO [8,9], without being hampered by charge leakage. Moreover, these techniques enable a straightforward separation of the different components of the induced charge, so as to obtain the variation of both the surface space-charge density and the occupancy of the interface states with the surface potential barrier. More important still, the use of a limited number of short-duration pulses minimizes electrochemical reactions which may otherwise greatly complicate the interpretation of the data. By the same token, surface damage that usually occurs under prolonged application of large DC biases is largely eliminated.

3. Experimental

The samples were cut from highly polished, transistor grade n-type silicon wafers of several ohm cm resistivity. The samples' dimensions were typically $3 \times 3 \times 0.5$ mm³, with the large faces parallel to the (111) plane. Chromium, followed by gold, was sputtered onto one of the large faces to form an ohmic contact. After attaching a wire lead, this face was glued to a glass tube, and the entire sample, except for a well-defined area of about 1 mm² on the opposite face, was masked by an epoxy cement (see fig. 1). The exposed area was etched in CP-4.

A schematic diagram of the experimental arrangement is displayed in fig. 1. The semiconductor sample and a platinum electrode are immersed in a $\text{Ca}(\text{NO}_3)_2$ electrolyte. Because of the masking described above, only a small area of the sample is exposed to the aqueous solution. The platinum electrode

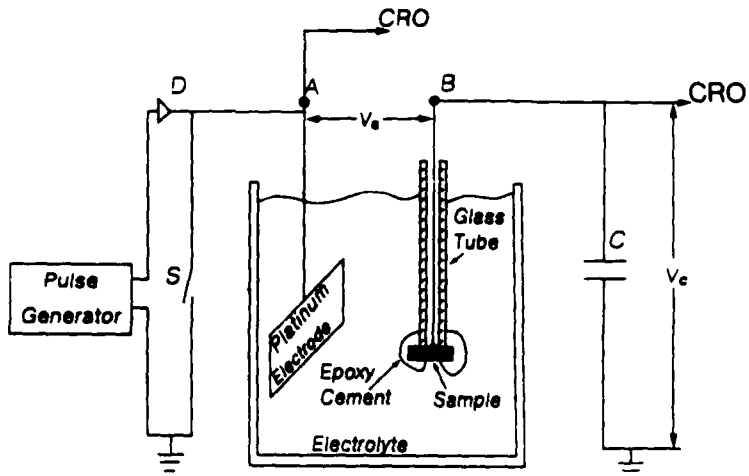


Fig. 1. Schematic diagram of semiconductor/electrolyte system.

(chosen because of its inertness) is in the form of a sheet of large surface area (about 2 cm²). The pulse generator (Hewlett-Packard type 214A) can provide positive and negative pulses of up to 100 V in amplitude and 0.05 to 200 μ s in duration. It is connected to the platinum and semiconductor electrodes via a diode D and a large (0.1 to 1 μ F) series capacitor C. The diode polarity is such as to permit current flow only while the pulse is on. An electronic switch S can short-circuit the Pt electrode to ground at any prescribed time following the termination of the pulse. Short-duration (0.1 to 10 μ s) pulses were applied singly, two or three pulses per data point taken, in order to minimize any electrochemical reactions that may take place at the silicon surface. A Tektronix type 7407 CRO was used to monitor the voltage drop V_s between the Pt electrode and the ohmic contact of the sample, and the drop V_c across the series capacitor C. Strictly speaking, the relevant oscilloscope is that of the voltage drop V'_s between a reference electrode and the sample, rather than V_s . However, the space-charge capacitance at the platinum surface is orders of magnitude larger than that at the semiconductor surface. Hence, only a negligible fraction of the applied bias is expected to drop across the Pt/electrolyte interface, so that the two traces should yield practically identical results. This was indeed checked to be the case by the occasional use [8,9] of a reference electrode.

In most cases a space-charge layer exists at the semiconductor surface, characterized by an equilibrium barrier height V_{s0} and a space-charge density Q_{sc0} . If surface states are present, there may also be an equilibrium surface-state charge of density Q_{ss0} . The voltage pulse, of amplitude anywhere between 0 and 100 V, charges up the semiconductor surface region. As will be shown in a moment, the voltage drop V_s , measured just after the termination of the pulse, represents to a very good approximation the change $\delta V_s = V_s - V_{s0}$ in barrier height induced by the applied pulse. (We assume for the moment that there is no foreign layer such as an oxide at the semiconductor surface.) The voltage drop V_c across the series capacitor C, again measured just after the termination of the pulse, yields the overall charge Q'_{tot} ($= CV_c$) passing through the system. The charge density Q_{tot} (per unit area) is obtained by dividing Q'_{tot} by the area of the semiconductor surface exposed to the electrolyte.

As suggested above, Q_{tot} is made up in general of three components:

$$Q_{tot} = \delta Q_{sc} + \delta Q_{ss} + Q_L, \quad (8)$$

where $\delta Q_{sc} = Q_{sc} - Q_{sc0}$ is the change in space-charge density, $\delta Q_{ss} = Q_{ss} - Q_{ss0}$ is the change in surface-state charge density, and Q_L is the density of the charge leaked across the S/E interface. In terms of electron densities, this can be re-written as

$$N_{tot} = \delta N_s + \delta N_{ss} + N_L, \quad (9)$$

where N_{tot} is the total electron density passing through the system.

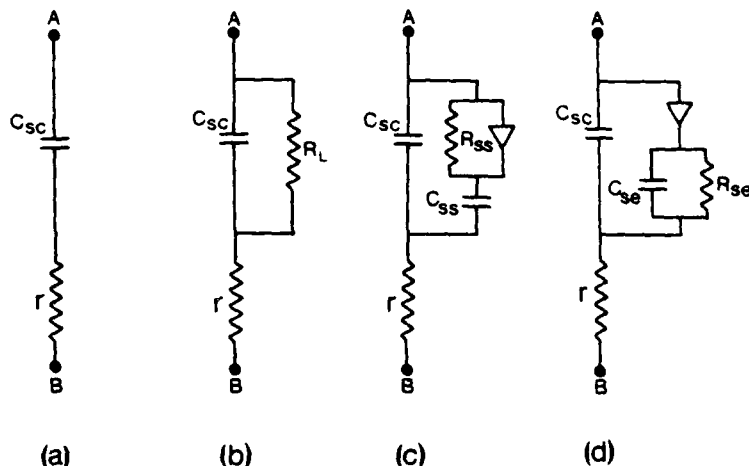


Fig. 2. Equivalent circuits representing semiconductor/electrolyte interface. (a) Perfectly blocking interface. (b) Simple leakage mechanism. (c) In presence of surface states. (d) Stored leakage mechanism.

$\delta N_s = N_s - N_{s0}$ is the change in excess surface electron density, $\delta N_{ss} = N_{ss} - N_{ss0}$ is the density change in surface-state occupation, and N_L the density of electrons that have leaked across the interface.

We shall now discuss the experimental procedure used in determining the magnitudes of the three components in eq. (8) or (9). This is best done in terms of the equivalent circuits shown in fig. 2. The ideal case of a perfectly blocking interface and no surface states is simulated by fig. 2a. Here the space-charge capacitance C_{sc} is shown in series with the combined resistance r of the electrolyte and the underlying semiconductor bulk below the surface. Typically, r is about 60Ω , approximately half of which representing the electrolyte resistance and the other half the sample resistance. Fig. 2b represents the simplest form of leakage across the interface, where a shunting resistance R_L is introduced in parallel with C_{sc} . More complex circuits prescribed by the experimental results to be presented below are shown in figs. 2c and 2d. In fig. 2c, R_L is replaced by a resistor R_{ss} shunted by a diode, both in series with a capacitor C_{ss} . This circuit corresponds to the case in which surface states are present and charge leakage is totally absent. On the application of a positive pulse, such states charge up very quickly, hence the shunting diode. Their discharge following the termination of the pulse is usually much slower, the more so the deeper they are located energetically and the lower the temperature [6]. Lastly, the circuit in fig. 2d simulates a special type of charge leakage, observed to take place in strong accumulation layers.

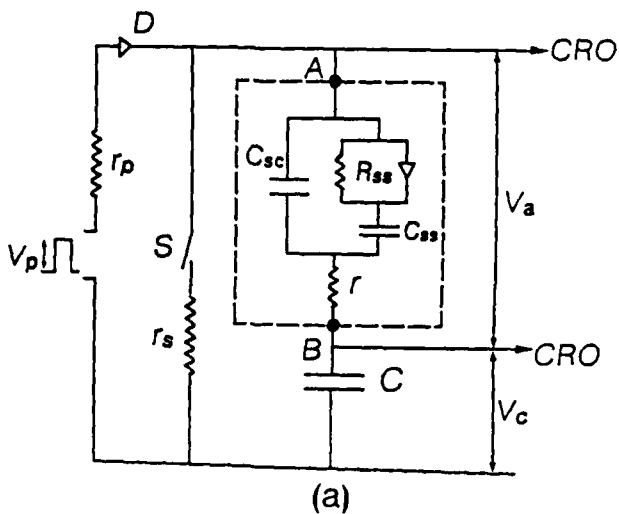
It should be noted that the equivalent circuits shown in fig. 2 serve merely

as a means of classifying the different processes at the S/E interface on the one hand, and as aids in the understanding of the methods of measurement, on the other hand. They do not represent accurately the actual conditions at the interface. In particular, all elements of the equivalent circuits (except r) are in reality not passive but voltage dependent.

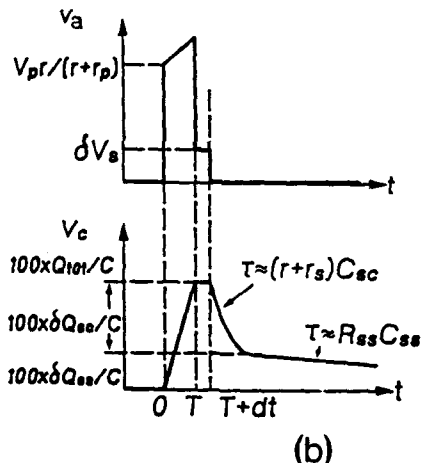
The detailed circuitry corresponding to the experimental arrangement shown in fig. 1 is displayed in fig. 3a. The sample is represented here (in the dashed enclosure) by the surface-state equivalent circuit of fig. 2c. The pulse generator, of internal resistance r_p ($= 50 \Omega$), is connected across the sample in series with the capacitor C . The magnitude of C is chosen so as to be large compared to the semiconductor surface capacitance, typically by a factor of 100 or so. The voltage developed across it is thus smaller (by the same factor) than the voltage developed across the space-charge layer. The diode D permits rapid charging of the system while the pulse is on and prevents its discharge (through the low-impedance pulse generator) after the termination of the pulse. The electronic switch S shorts point A (the Pt electrode) to ground a short time dt (usually $0.1 \mu s$) following the pulse termination, sufficient to permit accurate readings of V_s and V_c just after the termination of the pulse. The residual resistance r_s of the shorted switch is a few Ohms. In silicon, R_{ss} is found to be very large compared to both r_s and r .

Fig. 3b illustrates the time variations of V_s and V_c during and following the application of a positive pulse of amplitude V_p . All the values marked in fig. 3b correspond to unit surface area. The initial rise in V_s (at $t = 0_+$), up to the value $V_p r / (r + r_p)$, is very fast (about $0.01 \mu s$) and represents the ohmic voltage drop across r . Subsequently, V_s rises much more slowly as C_{sc} and C_{ss} charge up. At the termination of the pulse ($t = T$), V_s drops rapidly to the level δV_s , where δV_s is the voltage developed across C_{sc} , i.e. the induced change in the potential barrier height. As for V_c , it rises monotonically up to $t = T$, to the level Q_{tot}/C , where Q_{tot} is the total charge density induced by the pulse, consisting of the changes δQ_{sc} and δQ_{ss} in the space-charge and surface-state charge densities. Both V_s and V_c remain nearly constant up to the activation of the shorting switch (at $t = T + dt$). At this point V_s drops abruptly to practically zero (V_c being very small compared to V_s), and charge redistribution among C_{sc} , C_{ss} and C begins to take place. In the first stage, the charge δQ_{sc} stored in C_{sc} and its equal counterpart in C discharge relatively fast through $r + r_s$. The decay constant associated with this process is approximately $(r + r_s)C_{sc}$ (C_{sc} being small compared to C) and is typically a few microseconds. As a result, V_c decays (with the same decay constant) to the value $\delta Q_{ss}/C$, δQ_{ss} being the charge remaining in C after the fast decay process. Thereafter V_c decays with the much longer surface-state time constant of approximately $R_{ss}C_{ss}$. This behavior [$R_{ss}C_{ss} \gg (r + r_s)C_{sc}$] is characteristic of the silicon interface and enables the separate determination of both C_{sc} and C_{ss} , as well as of R_{ss} .

The pulse response of an interface represented by the stored leakage circuit in fig. 2d is identical, except for the important difference exhibited by the last decay stage of V_c . After the fast decay following the activation of the switch,



(a)



(b)

Fig. 3. (a) Circuitry of experimental arrangement. The sample is represented (in dashed enclosure) by the surface-state equivalent circuit (fig. 2c). (b) Schematic representation of expected pulse responses of the voltage drops V_a and V_c . Pulse amplitude V_p , pulse duration T , shorting switch activated at $T + dt$. (c) Actual pulse responses of V_a (upper trace, 1 V/cm) and V_c (lower trace, 50 mV/cm) for Si/electrolyte interface ($C = 0.33 \mu\text{F}$, $R + r_s = 70 \Omega$, surface area of interface $S = 1.9 \text{ mm}^2$). Time base 5 $\mu\text{s}/\text{cm}$. Some derived values: $8V_p = 0.8 \text{ V}$, $8Q_{101} = 2.8 \times 10^{-8} \text{ C}$ ($8N_s = 9 \times 10^{12} \text{ cm}^{-2}$).

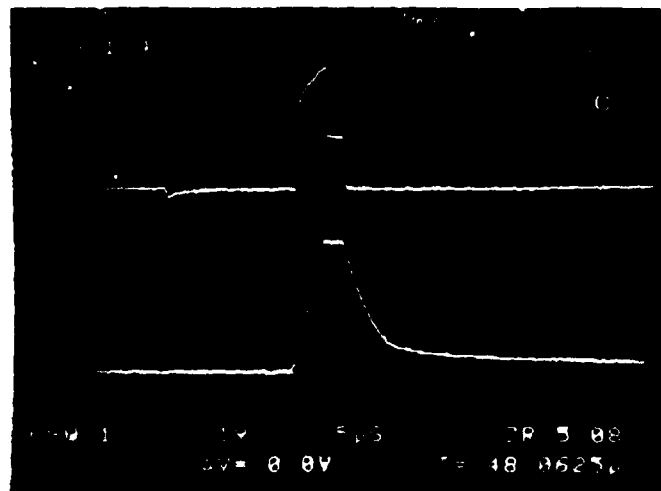


Fig. 3. (Continued).

which is characterized by the same decay constant of $(r + r_s)C_{se}$, V_c remains constant indefinitely. (In practice, V_c decays very slowly, with a time constant of typically 1 s, determined by the values of C and of the input impedance of the CRO.) It is this difference that makes it possible to distinguish in actual situations between charge storage in surface states (fig. 2c) and stored leakage charge (fig. 2d).

It should be noted that the leakage mechanism represented by fig. 2d involves charge storage (in C_{se}) and dissipation (through R_{se}), whereas in the simple leakage mechanism represented by fig. 2b, charge is not stored but dissipates continuously. One way of distinguishing between the two mechanisms is that for the same change δV_s in barrier height, the leakage charge should be, over a wide range, independent of pulse duration in the former case, as was observed for silicon, whereas it should increase with increasing pulse duration in the latter case.

As will be discussed below, in silicon the surface-state process is operative in depletion and weak accumulation layers, whereas for strong accumulation layers the stored leakage mechanism becomes significant as well. This can be simulated by adding to fig. 3a the stored leakage branch (C_{se} , R_{se} and the diode) of fig. 2d in parallel with the existing surface-state circuit (fig. 2c). Such a combination leaves the initial fast decay in V_c unaltered [decay constant $(r + r_s)C_{se}$]. The slow decay, however, now consists of two components: initially, V_c decays from $(\delta Q_{ss} + Q_L)/C$ to Q_L/C , with the surface-state time constant of $R_{ss}C_{ss}$, followed by a non-decaying component representing the stored leakage charge Q_L .

Typical oscilloscopes illustrating the actual pulse response of the Si/electrolyte interface for an applied positive pulse (induced accumulation layer) are displayed in fig. 3c. The upper and lower traces depict the time variation of V_a and V_c , respectively. They are seen to be very similar to the corresponding schematic diagrams in fig. 3b, indicating that the models discussed above do indeed provide a realistic description of the S/E interface. As expected, however, the decay processes of V_c following the activation of the shorting switch are not exponential, since the capacitative and resistive components in the actual S/E interface are not passive elements but voltage dependent. This does not interfere at all with the measurement of δV_s , δN_s , δN_{ss} and N_L , and the results to be presented below were obtained precisely as described in connection with fig. 3b. It should be noted that the fast decay in V_c is characterized by a decay time of 2 to 3 μ s, just the value to be expected from the discharge of the free electrons in the accumulation layer previously induced by the applied pulse [$(r + r_s)S\delta Q_{sc}/\delta V_s = 2.5 \mu$ s, S being the area of the silicon surface in contact with the electrolyte]. Accordingly, we identify the amplitude of the fast component as representing the induced change in space-charge density. As to the subsequent, much slower decay apparent in the V_c trace (decay time in the millisecond range), evidence will be presented below that it represents the discharge of surface states previously filled by the pulse. Its amplitude yields the change in surface state occupancy, while the decay characteristics are controlled by the kinetics of electron release back into the silicon conduction band. Finally, in strong accumulation layers, the slow decay is followed by a non-decaying component representing the leakage charge. For the same induced change δV_s , the magnitude of this component is found to be independent of pulse duration, indicating that the leakage is of the storage type (fig. 2d).

In order to get some idea as to the composition of the silicon interface, an Auger analysis was carried out. After the conclusion of the electrical measurements, one of the samples was removed from the electrolyte and inserted into the vacuum chamber of a Physical Electronics Scanning Auger Microprobe. The electron beam diameter was about 5 μ m and, in order to minimize possible electron desorption, a scanning mode over an area of 0.1×0.1 mm^2 was employed. Calibrated argon-ion sputtering (at 2000 eV) was used to peel-off successive layers of the surface region.

4. Results

The results to be reported are based on the analysis of oscilloscope traces of the type shown in fig. 3c above. Under equilibrium conditions, a depletion layer usually exists at the Si surface in contact with the electrolyte. Since the measurements described above yield directly only the changes $\delta N_s = N_s - N_{s0}$

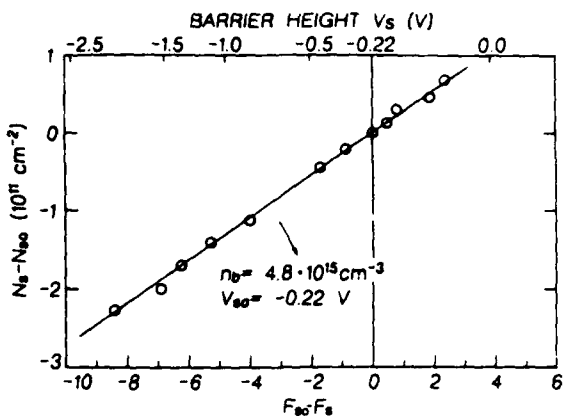


Fig. 4. Change $N_s - N_{s0}$ in excess surface electron density versus $F_{s0} - F_s$, as calculated for $V_{s0} = -0.22$ V. Corresponding values of the barrier height V_s are marked off at upper abscissa.

and $\delta N_{ss} = N_{ss} - N_{ss0}$ in the excess-surface and surface-state electron densities as functions of $\delta V_s = V_s - V_{s0}$, the first task is to determine the equilibrium barrier height V_{s0} . [The equilibrium surface electron density N_{s0} is then derived from eqs. (4) to (7).] Using eq. (4), we can write for depletion layers (V_s and V_{s0} negative)

$$\delta N_s = (\kappa \epsilon_0 n_b kT/q^2)^{1/2} (F_{s0} - F_s), \quad (10)$$

where F_{s0} and F_s are the values of F_s for V_{s0} and $V_{s0} + \delta V_s$, respectively, as given by eq. (7). A plot of the $N_s - N_{s0}$ data against the calculated values of $F_{s0} - F_s$ should yield a straight line only if the correct value of V_{s0} is chosen in the calculation of F_{s0} and F_s . A simple computer program has been set up to so determine V_{s0} . The results are shown in fig. 4, where the choice of $V_{s0} = -0.22$ V is seen to lead to the required linear relation. The accuracy of this method is about ± 0.02 V, the limits for which deviations from linearity become detectable. The slope of the straight line yields the electron bulk concentration n_b [see eq. (10)]. The value so obtained is marked on fig. 4 and agrees well with Hall effect measurements.

Once V_{s0} and N_{s0} have been determined, the complete N_s versus V_s curve (depletion and accumulation ranges) can be evaluated from the measured data through the relations $V_s = V_{s0} + \delta V_s$, $N_s = N_{s0} + \delta N_s$. Typical results obtained in this manner are displayed by the open circles in the semi-log plot of fig. 5. In the depletion range ($V_s < 0$), N_s is negative but, because of the logarithmic scale used, the plot is that of its absolute magnitude. The solid curve represents eqs. (4) and (5), and is seen to account well for the data in depletion and moderate accumulation layers. The deviations of the points from the

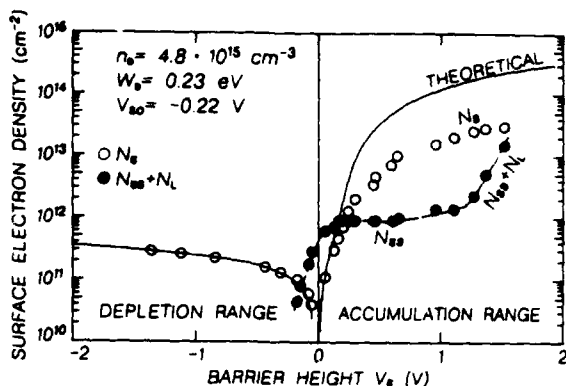


Fig. 5. Surface electron density versus barrier height. Open circles represent excess surface electron density N_s , with theoretical curve calculated from eqs. (4) and (5). (In the depletion range, $V_s < 0$, N_s is negative and the plot is that of $-N_s$.) Full circles represent sum of density N_{ss} of occupied surface states and of density N_L of electron leakage.

theoretical curve for stronger accumulation layers will be discussed below. The full circles represent the sum of the occupied surface-state (N_{ss}) and the electron leakage (N_L) densities. The curve plotted through these points (dashed) is seen to rise from a low value up to a saturation level which remains constant over a considerable range of V_s . Thereafter it rises steeply (nearly exponentially) with increasing V_s . Such a behavior indicates that the plateau represents the total density of surface states which, at $V_s \approx 0.2$ V fill up completely, while the steep rise for stronger accumulation layers is associated with electron leakage across the S/E interface. This conclusion is supported by the observation that in the plateau region the decay time of the charge stored in the series capacitor C (see fig. 3) is less than 2 ms (see fig. 9 below), whereas the decay time associated with the steeply rising component for strong accumulation layers is 1 s, the instrumental time constant.

Independent evidence for the above interpretation is provided by the data displayed in fig. 6. Here, similar results, obtained on a different Si sample, are shown (open and full circles) in the accumulation range. After these data had been taken, a small positive DC bias was superimposed in series with the pulse generator. As a result, the equilibrium barrier height of $V_{s0} = -0.42$ V has been shifted to $+0.09$ V, corresponding to a very weak accumulation layer. Pulse measurements carried out under these conditions are represented by the open and full triangles in fig. 6. It is seen that the N_s data obtained before (circles) and after the application of the DC bias (triangles) coincide, as they should. However, the surface-state plateau has disappeared, leaving behind only the leakage component N_L , which now varies exponentially with V_s throughout. As expected, the DC bias shifts the energy bands downwards and

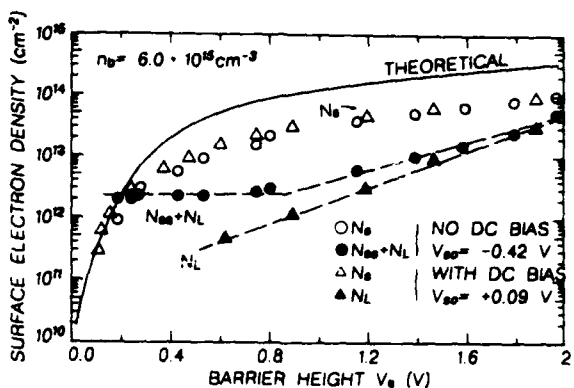


Fig. 6. Surface electron density versus barrier height in the accumulation range. Circles correspond to equilibrium barrier height ($V_{s0} = -0.42$ V), triangles to shifted barrier height ($V_{s0} = +0.09$ V) as produced by DC bias.

as a result the surface-state levels are brought below the Fermi level and become fully occupied. Charge induced by positive pulses can then no longer be localized in surface states: it can only reside in the space-charge region and possibly leak across the S/E interface.

The departure of the N_e points from the theoretical curve under strong accumulation conditions, as seen in both figs. 5 and 6, may have two possible origins. One may involve the theoretical curve which was calculated classically, without taking into account quantization effects. Such effects are expected to broaden the accumulation layers and hence to shift the corrected curve towards larger V_s values, bringing it somewhat closer to the experimental points. However, as was pointed out above, the corrections to the classical curve are expected to be relatively small [8,9], far from sufficient to account for the experimental data. The other, and more likely possibility is that an oxide layer at the Si surface is responsible for the major part of the observed deviation. The effect of the series Helmholtz layer cannot be completely ruled out although we have good grounds [1] to suppose that it is appreciably thinner. In any case, the series combination of these two layers would effectively introduce a "geometric" capacitance C_g in series with the Si surface capacitance. Referring to figs. 2 and 3, one can readily see that the measured values of the induced charge densities δQ_{sc} , δQ_{ss} and Q_L will not be affected by the presence of C_g . However, the voltage drop V_s (measured at the termination of the pulse) will now be distributed between C_g and the space-charge capacitance C_{sc} . Thus, the effect of the oxide and Helmholtz layers would be to reduce δV_s by Q_{tot}/C_g . The results in fig. 5 are re-plotted in fig. 7 on this premise, with C_g chosen so as to obtain the best fit between the

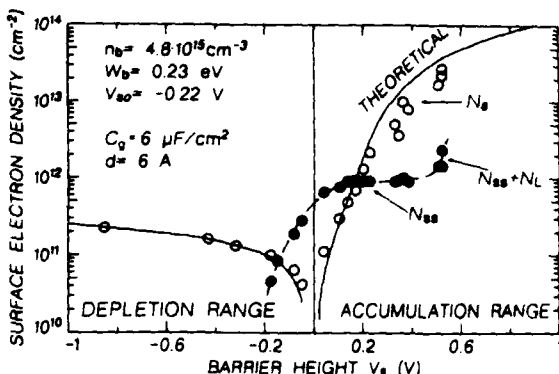


Fig. 7. Re-plot of data in fig. 5 on the assumption that an oxide layer 6 Å thick (introducing geometric capacitance C_s of $6 \mu\text{F}/\text{cm}^2$) is present on silicon surface.

adjusted points and the theoretical curve. The agreement is not bad, considering that only one adjustable parameter (C_s) has been used. The magnitude of C_s so estimated is $6 \mu\text{F}/\text{cm}^2$. Using a value [11] of 3.9 for the relative dielectric constant of silicon oxide, we conclude that the oxide layer is 6 Å thick, somewhat less if we take into account the appreciably larger but unknown-precisely Helmholtz capacitance. This corresponds to about 2 monolayers (ML), which is quite reasonable. Attempts to dissolve the thin oxide layer by adding HF to the electrolyte did not succeed, the changes introduced being within the experimental uncertainty.

It should be noted that whether the deviations are due to the presence of an oxide layer as assumed above, to quantization effects or to some other unknown factor, they do not affect the analysis to be presented below of the surface state data. Inspection of fig. 5 shows that the plateau level in N_{ss} , corresponding to fully occupied surface states, is reached before the N_s points begin to deviate from the theoretical curve. Thus, the V_s values in the pertinent range ($V_s < 0.2$ V), which are used in the analysis below, are not adjusted values.

The N_{ss} results in fig. 5 are re-plotted in fig. 8 on a linear scale. One sees that the surface states begin to fill up at $V_s = -0.2$ V and when $V_s = +0.2$ V they become fully occupied at a density of $9 \times 10^{11} \text{ cm}^{-2}$. [Coincidentally, for this sample ($W_b = 0.23$ eV), they are half filled under just about flat-band conditions ($V_s = 0$)]. The dashed curve represents the Fermi-Dirac distribution function for a discrete distribution of surface states located 0.23 eV below the conduction-band edge. Obviously, such a distribution cannot account for the data, indicating that the surface states must be spread out in energy. The simplest distribution of this sort is a continuous uniform distribution. The best

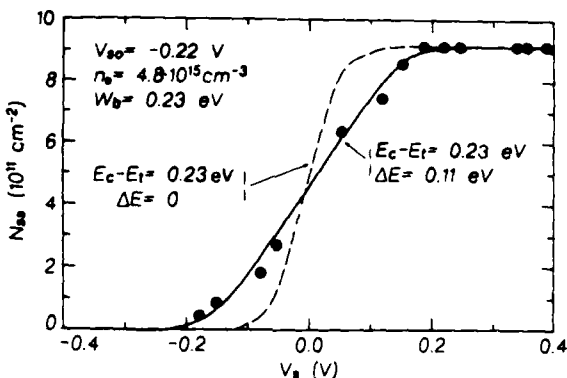


Fig. 8. Density N_{ss} of occupied surface states versus barrier height V_s . Curves represent Fermi-Di-
rac function for discrete (dashed curve) and continuous uniform (full curve) distribution of surface
states.

fit, represented by the solid curve, was calculated for such a distribution, centered 0.23 eV below the conduction-band edge and spreading up to $\Delta E = 0.11$ eV on either side.

More direct evidence for the essentially uniform nature of the surface-state distribution is derived from measurements of the decay characteristics of the surface-state charge following the activation of the shorting switch. In the equivalent circuit of fig. 3, the decay is exponential (with a time constant of $R_{ss}C_{ss}$). This would have also been the case for the actual surface were the surface states discrete in energy. The interaction kinetics between the surface states and the conduction band would then be governed by [6]

$$dN_{ss}/dt = v_T A [n_s (N_i - N_{ss}) - n_1 N_{ss}], \quad (11)$$

where N_i is the total density of surface states (occupied and unoccupied), v_T is the electron thermal velocity, A is the capture cross section of the surface states, and n_s is the electron volume concentration at the surface; the so-called emission constant n_1 is given by

$$n_1 = N_c \exp[-(E_c - E_i)/kT], \quad (12)$$

where N_c is the effective density of states in the conduction band and $E_c - E_i$ is the energy depth of the discrete surface states below the conduction-band edge E_c . Under the conditions of the experiment, the surface states are filled up by the applied pulse. Following the activation of the shorting switch, the initial depletion condition of the surface is practically fully restored after the relatively fast decay of the induced space charge, and before the onset of the slower decay in surface-state charge. Hence, n_1 is very small throughout the

surface-state decay process and the first term on the right-hand side of eq. (11) can be neglected. The solution of this equation is then

$$N_{ss} = N_t \exp(-t/\tau_{ss}), \quad (13)$$

where τ_{ss} is the surface-state time constant given by

$$\tau_{ss} = 1/(v_T A n_1). \quad (14)$$

The decay in surface-state charge should thus be exponential.

Actually, the measured decay is far from exponential, exhibiting decay times ranging from microseconds to milliseconds (see fig. 9 below). This immediately indicates that the surface states are not discrete but spread out in energy, with the shallow ones discharging first and the deeper ones with increasing decay times the deeper they are located. For a continuous distribution, N_{ss} and N_t in eq. (11) should be replaced by $\bar{N}_{ss}(E)$ and $\bar{N}_t(E)$, the occupied and total surface-state densities per unit area and now per unit energy as well. The solution then becomes

$$N_{ss} = \int_{E_t - \Delta E}^{E_t + \Delta E} \bar{N}_{ss}(E) dE = \int_{E_t - \Delta E}^{E_t + \Delta E} \bar{N}_t(E) \exp[-t/\tau(E)] dE, \quad (15)$$

where the integration extends over the energy range $\pm \Delta E$ encompassing the surface states, and

$$\tau(E) = (1/v_T A N_c) \exp[(E_c - E)/kT]. \quad (16)$$

The three sets of points in fig. 9 represent the time dependence of N_{ss} , the density of occupied surface states, measured at three temperatures as marked. In order to accommodate the large range of decay times, a rather non-conventional logarithmic time scale has been employed. The parameters $E_c - E_t$ and

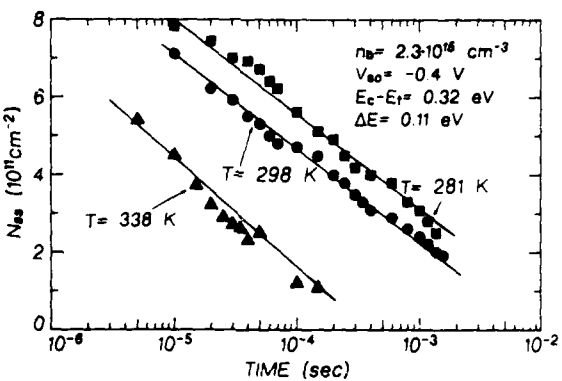


Fig. 9. Decay characteristics of electrons trapped in surface states measured at three temperatures as marked. Parameters of surface states, as determined by surface capacitance measurements, are listed at top. The curves were calculated from eqs. (15) and (16) based on these parameters.

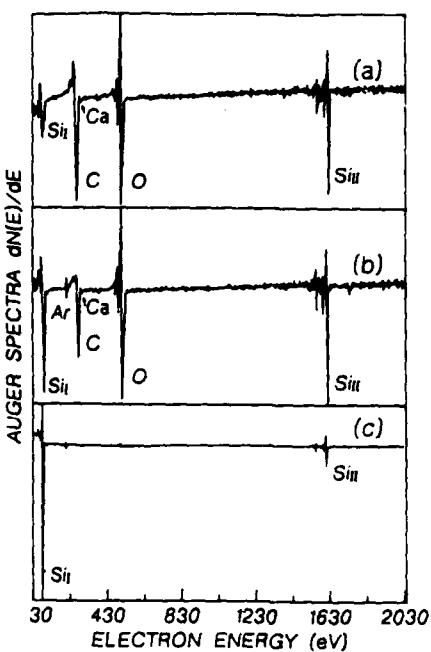


Fig. 10. Auger survey of silicon surface. (a) Immediately after sample was removed from electrolyte. (b) After 1 min argon-ion sputtering. (c) After prolonged argon-ion sputtering.

ΔE of the surface-state energy distribution have been determined from the analysis of N_{ss} versus V , data similar to that shown in fig. 8 for a different sample, and are listed at the top of fig. 9. The curves in fig. 9 were calculated by numerical integration of eqs. (15) and (16), based on these parameters. The surface-state distribution in the energy interval $\pm \Delta E$ has been assumed to be uniform ($\bar{N}_s(E)$ constant). The only adjustable parameters used were the values of the cross section, and these solely for the purpose of determining the vertical positions of the calculated curves. The cross sections come out a little different for the three temperatures (3.5×10^{-18} , 4×10^{-18} and $9 \times 10^{-18} \text{ cm}^2$ for 281, 298 and 338 K, respectively). The calculated time dependences have not been adjusted at all and are seen to account very well for the data.

The width and composition of the thin oxide layer assumed to be present at the silicon surface while in contact with the electrolyte cannot be determined by direct means. Obviously, even if such a layer were absent for some reason, it would undoubtedly be formed after removal of the sample from the electrolyte. Nevertheless, some idea as to the characteristics of the oxide can be obtained from the Auger spectra in figs. 10 and 11, taken for a sample that had previously been immersed in a $\text{Ca}(\text{NO}_3)_2$ electrolyte. In fig. 10 are

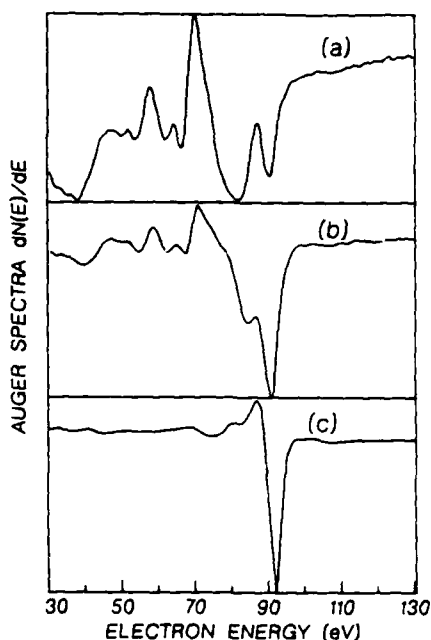


Fig. 11. Auger spectrum on an expanded energy scale showing the Si_L line for the same three stages as in fig. 10.

displayed three representative Auger surveys taken at one point of the silicon surface. Curve (a) was obtained right after the sample was inserted into the Auger chamber. The Si line around 90 eV (designated by Si_L) is heavily masked by carbon and oxygen coverages, as evidenced by the strong C and O lines. A weak Ca line is also apparent. Curve (b) was obtained after a 1 min argon-ion sputtering. Using a value of 0.5 for the sputtering yield [12], we estimate that some 5 Å of the surface region have been sputtered away. The carbon and oxygen coverages have been appreciably reduced, as evidenced by the strong enhancement of the Si_L line. The Ca line, on the other hand, is still present, with its amplitude relative to that of the oxygen line almost undiminished. Curve (c), obtained after a more prolonged argon sputtering, represents the clean state of the silicon surface.

In fig. 11, the Si_L line is plotted on an expanded energy scale for the same three stages as in fig. 10. For the unspattered surface [curve (a)], the amplitude of the silicon oxide line [13] (at about 80 eV) is seen to be roughly 50% larger than that of the silicon line (at 90 eV). Analysis of this curve along the lines used by Kelemen et al. [14] yields an oxide-layer thickness of about 15 Å. After the 1 min sputtering [curve (b)], the amplitude ratio of the silicon oxide

and silicon lines decreases, leading to an estimated oxide-layer thickness of 10 Å. This is consistent with our estimate that a 5 Å layer has been sputtered away. In curve (c), corresponding to the clean surface, only the Si line is present, as expected.

Auger scans performed at different locations of the surface show some variation in the relative amplitudes of the silicon oxide and silicon lines. The best estimate for the initial oxide thickness, obtained by averaging the data over the surface, is 12 Å. The margin of error in this value is, however, quite large, at least 25%.

5. Conclusion

The pulse technique method applied to the semiconductor/electrolyte system appears to be a powerful tool for the study of silicon as well as other semiconductor surfaces. It enables a wide swing in barrier height, ranging from depletion to extremely strong accumulation conditions. As a result, a fairly detailed characterization of the space-charge layer and of the surface states becomes available. As for depletion and moderate accumulation layers on silicon, the N_s versus V_s data obtained are in good agreement with the expressions derived from the classical solution of Poisson's equation. Such agreement has been obtained with no adjustable parameters whatsoever. It is maintained irrespective of whether the surface states are fully occupied or empty (see fig. 6). In the former case, the entire charge induced by the applied positive pulse (aside from the small leakage charge) resides in the space-charge region in the form of free electrons. In the latter case, the surface states absorb a significant fraction of the induced charge, and it is the special feature of the pulse technique used that enables a quantitative separation between the charge trapped in the surface states and that induced in the space-charge region. This is substantiated by the observation that the N_s versus V_s data for the two cases are identical. This example and the general agreement between theory and experiment lend, we believe, strong support to our contention that the measurement technique is adequate, and provide confidence in the analysis of data in stronger accumulation layers where the experimental points appear to deviate from the theoretical curve. One might argue that the lack of agreement in this range may be indicative of the involvement of electrochemical processes rather than that of the simple process of the charging of the space-charge region. However, the pulse response in both the moderate and the strong accumulation ranges appears identical in shape and detailed characteristics, and it is therefore unlikely that such a sharp change between "physical" and "chemical" mechanisms would take place in the transition between moderate and strong accumulation conditions. In both regimes the results are independent over wide limits of the applied pulse duration. Even the strongest

accumulation layer can equally well be induced in as short a time as 0.2 μ s as (with much lower pulse amplitudes) in 10 μ s or longer. Also, and more important, the fast decay process (following the activation of the shorting switch) is characterized by just the decay time expected from the discharge of free electrons in the previously induced accumulation layer (see discussion in connection with fig. 3c). It would be too much of a coincidence if these and other features of the observed pulse response would be the result of electrochemical processes. We strongly believe, rather, that the differences between theory and experiment found in very strong accumulation layers are due to the presence on the silicon surface of an oxide layer. A 6 \AA layer, corresponding to about 2 ML, appears to account well for the observed differences, with the good agreement with theory now extending throughout (see fig. 7). The fact that only one parameter is required for such a fit lends further support to our interpretation.

The Auger data indicate that an oxide layer about 12 \AA thick exists at the surface. Some of the oxide has probably grown when the sample was transferred from the electrolyte into the Auger chamber. Very likely, this accounts for the thickness estimated from the Auger data being larger than that derived from the electrical measurements. At the same time, the persistence of the calcium line (originating from the $\text{Ca}(\text{NO}_3)_2$ electrolyte used), after some 5 \AA of the surface region had been sputtered away, suggests that part of the oxide had been present on the silicon surface while in contact with the electrolyte. The fact that HF added to the electrolyte does not seem to remove the oxide may be considered as an argument against this supposition, but it is more likely that the oxide is continuously replenished while being dissolved by HF.

The presence of the oxide layer, thin as it is, precludes the use of the space-charge capacitance measurements for a more detailed study, similar to that achieved in ZnO [8,9], of quantization effects in the induced accumulation layers. This is because in the range of most interest (surface electron densities between 10^{13} and 10^{14} cm^{-2}), the width of the space-charge layer approaches and eventually becomes comparable to the thickness of the oxide layer and, as a result, the barrier height cannot be determined to any reasonable accuracy. The mere fact, however, that such strong accumulation layers can be induced at the silicon surface opens up interesting possibilities of studying quantization effects by other means. In particular, transport and optical measurements of the type performed on MOS inversion layers [4,5] could no doubt be advantageously employed for this purpose, with the available range of surface electron densities extended tenfold.

There are several arguments supporting the identification of the observed interface states with surface states at the silicon surface, rather than with more complex electrochemical reactions. The first is based on the observation of the extended plateau in the N_{ss} versus V_s curve (see figs. 5 and 6). The plateau signifies the complete filling up of all the interface states and determines

directly their density at about 10^{12} cm^{-2} . This is just the density of surface states typical of oxidized silicon surfaces [6,15]. Moreover, the plateau is observed to disappear completely after a small positive DC bias has been applied (fig. 6). This is the very behavior expected from surface states: the DC bias shifts the energy bands downwards and, as a result, the surface-state energy levels are brought below the Fermi level and become fully occupied. Under these conditions the surface states cease to be operative in the pulse measurement, hence the disappearance of the plateau. Finally, further support for our interpretation is provided by a completely different type of measurement, that of the decay characteristics of the charge trapped in the interface states. The points in fig. 9 represent the measured decay in the trapped electron density N_{ss} , while the curves were calculated on the basis of the state parameters as derived from analysis of the N_{ss} versus V_s data. The curves are seen to account very well for the measured time dependencies (at three temperatures) characterizing the processes of electron release from the states into the conduction band. It should be noted that the calculated time dependencies are very sensitive to the energy position of the states [see eqs. (15) and (16)], so that the good agreement is most significant. It is difficult to envisage any mechanism other than the one involving surface states that would be both self-consistent and compatible with these various observations.

It appears, then, that a fairly complete mapping of the surface-state distribution in the upper half of the silicon energy gap has been achieved. The surface states, of total density around 10^{12} cm^{-2} , are found to be uniformly distributed over an energy interval of 0.2 eV. Much the same density and energy distribution has been observed for a number of samples. The center of the uniform distribution has been found, however, to vary somewhat from sample to sample, lying in the range 0.23 to 0.33 eV below the conduction-band edge. The measurements described do not probe any surface states that may lie in the lower half of the energy gap. Such states, if present, would be fully occupied in equilibrium and would take impractically long times to release their electrons when depletion layers are induced. The origin of the surface states is not known. Judging from the value of their capture cross sections (around $5 \times 10^{-18} \text{ cm}^2$) they should be of the "fast" type and are probably situated very close to the boundary between the silicon surface and its oxide [6].

The results shed also some light on the charge leakage process across the Si/electrolyte interface taking place under strong accumulation conditions. The observation that such leakage increases nearly exponentially with barrier height and hence with interface field suggests that electrons tunnel from the accumulation layer into some unidentified ionic species in the electrolyte. The charge leakage can take place practically instantaneously, in less than $0.1 \mu\text{s}$ following the onset of the applied pulse, as expected from a tunneling process. What is most surprising, however, is that the leakage charge remains stored

somewhere close to the interface for a considerably longer time. It could well be that the tunneling electrons saturate all the active ionic species within a tunneling distance corresponding to the induced interface field. The storage time may then represent the time it takes for the neutralized ionic species to diffuse away from the interface. More work is required to elucidate the nature of this rather unexpected type of leakage.

The pulse techniques described in this paper can also be used advantageously to map out the energy distribution of bulk states when present [2]. Just as for the case of surface states discussed here, the occupation of bulk states in the space-charge region can be varied by inducing changes in the surface barrier height. The analysis is then more involved but it is still manageable. Preliminary measurements on amorphous silicon and copper indium diselenide look promising in this respect.

Acknowledgment

This work was supported in part by US Army Research Office Grant DAAG29-84-G-0059.

References

- [1] S. Trokman, PhD Thesis, Hebrew University of Jerusalem, Jerusalem (1978);
A. Many and I. Balberg, Investigation of Semiconductors by the Electrolyte/Solid System, Final Report of United States-Israel Bi-National Science Foundation, No. 1340, 1980, unpublished.
- [2] S. Trokman, A. Many, Y. Goldstein, G. Heiland, D. Kohl and H. Moermann, *J. Phys. Chem. Solids* 42 (1981) 937.
- [3] F. Stern, *Phys. Rev. B5* (1972) 4891.
- [4] T. Ando, A.B. Fowler and F. Stern, *Rev. Mod. Phys.* 54 (1982) 434.
- [5] See, for example, Proc. 4th and 5th Intern. Conf. on Electronic Properties of Two-Dimensional Systems, *Surface Sci.* 113 (1982) and 142 (1984).
- [6] A. Many, Y. Goldstein and N.B. Grover, *Semiconductor Surfaces* (North-Holland, Amsterdam, 1965).
- [7] J. McDougall and E.C. Stoner, *Trans. Roy. Soc. London A237* (1938) 67.
- [8] D. Eger, A. Many and Y. Goldstein, *Surface Sci.* 58 (1976) 18.
- [9] D. Eger and Y. Goldstein, *Phys. Rev. B19* (1979) 1089.
- [10] S.R. Morrison, in: *Progress in Surface Science*, Vol. 1, Ed. S.G. Davison (Pergamon, Oxford, 1971) p. 105;
S.R. Morrison, *The Chemical Physics of Surfaces* (Plenum, New York, 1977).
- [11] H.F. Wolf, *Silicon Semiconductor Data* (Pergamon, Oxford, 1969).
- [12] N. Laegreid and G.K. Wehner, *J. Appl. Phys.* 32 (1961) 365.
- [13] B. Lang, P. Scholler and B. Carriere, *Surface Sci.* 99 (1980) 103, and references therein.
- [14] S.R. Kelemen, Y. Goldstein and B. Abeles, *Surface Sci.* 116 (1982) 488.
- [15] E.H. Nicollian and J.R. Brews, *MOS (Metal Oxide Semiconductor) Physics and Technology* (Wiley, New York, 1982).

ALLOYING EFFECTS ON THE OPTICAL ABSORPTION EDGE AND
PHOTOCONDUCTANCE OF RF SPUTTERED $a\text{-Sn}_x\text{Si}_{1-x}\text{:H}$ FILMS

R. Perez, O. Resto, S. Z. Weisz, and Y. Goldstein*
Department of Physics, University of Puerto Rico,
Rio Piedras, PR 00931

ABSTRACT

Hydrogenated amorphous Sn-Si alloy films were prepared by reactive co-sputtering at 220 and at 110°C. The tin content of the films varied between 0.3 and 4.7 at.%. The optical absorption and photoconductivity were measured as a function of wavelength and film composition. The energy gap, as evaluated from these measurements, decreases with increasing tin content, more strongly for samples prepared at the lower temperature. The photoconductance response, $\eta\mu\tau$, varies strongly, by about three orders of magnitude, as the Sn concentration increases to 4.7 at.% and is quite different for the two kind of samples.

INTRODUCTION

Over the last few years considerable effort has been devoted to the study of silicon based hydrogenated amorphous semiconductor alloys. Most of this research was prompted by the need for new materials to be used in photovoltaic solar cells. It was found that the optical band gap of the alloys changes systematically with composition and it becomes possible, at least in principle, to tailor the gap to any particular application. Alloys of Si with Ge or C received most of the attention and have been by now reasonably well characterized [1-14].

* Permanent address: Racah Institute of Physics, The Hebrew University, Jerusalem, Israel

The electronic and optical properties of hydrogenated amorphous alloys of Si with Sn were investigated much less extensively. Itozaki et al. [15] investigated the conductivity and optical gap of Si-Sn alloys prepared by sputter-assisted plasma CVD, where the glow discharge is used both to decompose silane gas and to sputter Sn from a solid tin target. Williamson et al. [16] studied the structure, conductivity, and optical properties of films prepared by reactive co-sputtering using a planar magnetron target holder. The target consisted of a silicon target and small pieces of tin wafers in a random array. The sputtering power used was relatively high (- 500 W) and the substrate was rotated to ensure uniformity. The substrate temperature during sputtering was about 150 - 170°C. Mahan et al. [17] studied the optical gap and photoconductivity of films prepared by the glow discharge technique using silane, hydrogen, and SnCl_4 or $\text{Sn}(\text{CH}_3)_4$ gas mixtures.

In this paper we present a study of the optical properties and photoconductivity of hydrogenated amorphous $a\text{-Sn}_x\text{Si}_{1-x}\text{:H}$ alloys prepared by reactive RF sputtering. The usual procedure in the preparation of hydrogenated amorphous films is to heat the substrate during deposition to elevated temperatures (around 200 - 300°C) and we did so likewise. However, to see the influence of deposition temperature upon film properties we studied also samples prepared at a much lower temperature (110°C). The method of film preparation was similar to that of Williamson et al. [16], except that the tin pieces were placed on one side of the silicon target and each deposition yielded thus a film with a compositional variation along its length.

FILM PREPARATION

The $a\text{-Sn}_x\text{Si}_{1-x}\text{:H}$ films were sputtered reactively in a conventional parallel plate RF (13.56 MHz) sputtering system using a gas mixture of argon at 12 mTorr and hydrogen at 2 mTorr and an RF power of 50 W with a cathode self-bias voltage of -900 V. In order to produce a compositional gradient in the plane of the substrate we used a silicon full-disc target (of 15 cm dia.) on top of which we bonded a

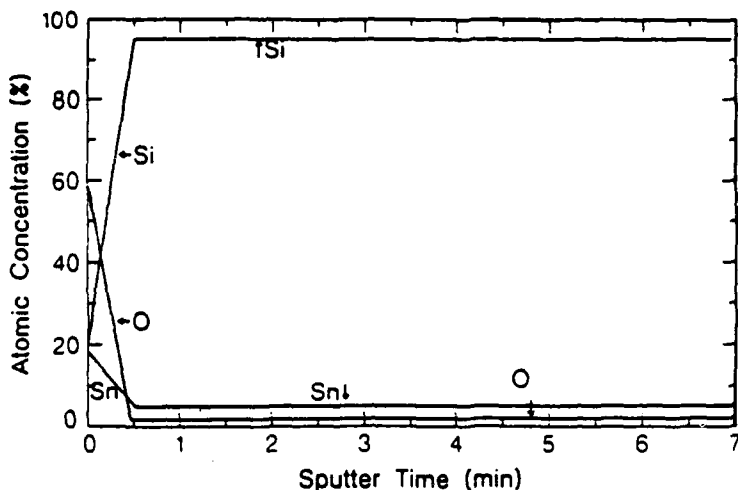


FIGURE 1. The atomic concentration of silicon, tin, and oxygen as a function of sputtering time with Ar⁺ ions for a 3.5 at.% tin sample, obtained by Auger depth profiling.

number of small (- 1 cm dia.) tin discs. The tin discs were grouped into a spherical sector of about 30°. The substrates, quartz or 7059 glass, were mounted on an electrically grounded steel plate facing the target in a plane parallel with and 5 cm above the target. The steel plate was electrically heated to maintain the substrate at the desired temperature. Samples prepared at two temperatures, 220 and 110°C, were studied.

The substrates were 1.2 cm wide and 15 cm long and were positioned above the target with the long axis bisecting the 30° sector with the tin discs. The Sn-Si films were about 13 cm long and 3 mm wide. For electrical measurements 50 metal contacts were deposited onto the substrate at intervals of 2.5 mm prior to the deposition of the Sn-Si film, thus dividing the film into 49 samples.

To evaluate the composition of the film as a function of position we used Auger electron spectroscopy. We used depth profiling to ascertain that the tin concentration is constant throughout the sample thickness. In this method the sample surface is being peeled-off by

controlled argon-ion sputtering while continuously monitoring the Auger spectrum. An example of such a measurement is shown in Fig. 1. The data were taken using an argon-ion beam at 4 kV and an electron beam at 5 kV. We plot in Fig. 1 the atomic concentration of Si and Sn as a function of sputtering time for a sample having about 3.5 at.% Sn. As can be seen in the figure, after the sample has been cleaned off, the Sn concentration is fairly constant throughout the sample thickness. We also monitored the oxygen concentration in the films; in the sample shown in Fig. 1 the concentration of oxygen is below 0.5 at.%. The above is true for samples having a tin concentration below about 10 at.%. Auger depth profiling of samples with higher tin content showed that Sn tends to precipitate to the surface and in parallel we also found a higher oxygen content. The results presented in this paper were obtained on samples having low Sn concentration and the oxygen content and the uniformity of the tin concentration was always checked with Auger depth profiling.

RESULTS

The optical absorption coefficient α as a function of wavelength was measured by using a Nicolet 6000 FTIR spectrometer. The analysis of the data followed the procedure outlined by Cody et al. [18]. The optical band gaps E_G were determined by fitting the measured absorption coefficient by the Tauc relation

$$(\alpha h\nu)^{1/2} = \text{constant}(h\nu - E_G)$$

for photon energies $h\nu > E_G$. In Fig. 2 we plot the values of the optical gaps as a function of Sn concentration for two a-Sn_xSi_{1-x}:H films, one prepared at 220°C (triangles) and the other at 110°C (circles). We see that the gaps for both films decrease fairly rapidly, and much more so for the film prepared at the lower temperature. The value for a-Si:H (square), also shown in the figure, was measured on a film prepared at 220°C under similar conditions as the a-Sn_xSi_{1-x}:H films but with a target of silicon only (without tin).

The rate of decrease of the optical absorption coefficient with decreasing photon energy was found to be very much the same for

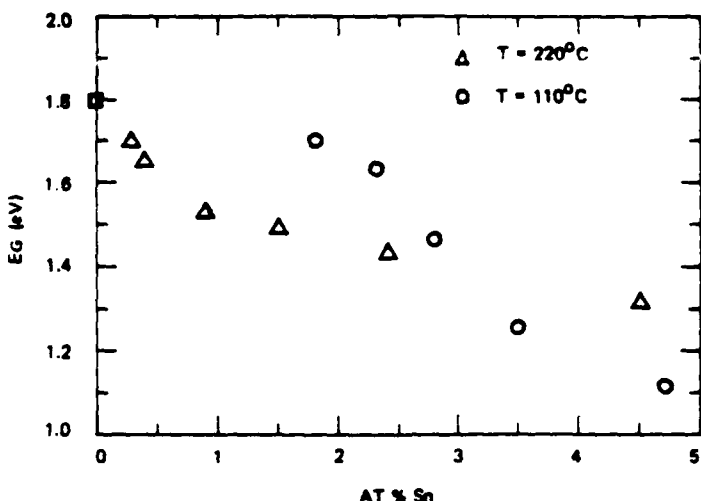


FIGURE 2. The optical band gap as a function of tin concentration for two $a\text{-Sn}_{x}\text{Si}_{1-x}\text{:H}$ films prepared at 220°C (triangles) and 110°C (circles) and an $a\text{-Si:H}$ sample (square).

samples prepared at both temperatures. The decrease is quite gradual and nowhere as abrupt as, for instance, in $a\text{-Ge}_x\text{Si}_{1-x}\text{:H}$ alloys [13], indicating the presence of defect states introduced by the alloying. As an example, we plot in Fig. 3 the optical absorption coefficient on a logarithmic scale as a function of photon energy for five samples prepared at 110°C and having different tin content, as marked. The full symbols represent optical data and were obtained from optical transmission measurements. The open symbols represent data derived from photoconductivity measurements, and, as can be seen in the figure, are in good agreement with the optical data. We notice that the data shift to lower energies with increasing tin content, as expected.

The photoconductivity was measured using a Bausch & Lomb monochromator, a chopper at 17 cps and a lock-in amplifier. The photon flux was determined by measuring the photoconductivity of a germanium single-crystal sample, the carrier lifetime (20 μsec) in which had been determined previously. The flux was of the order of $10^{15} \text{ cm}^{-2}\text{sec}^{-1}$.

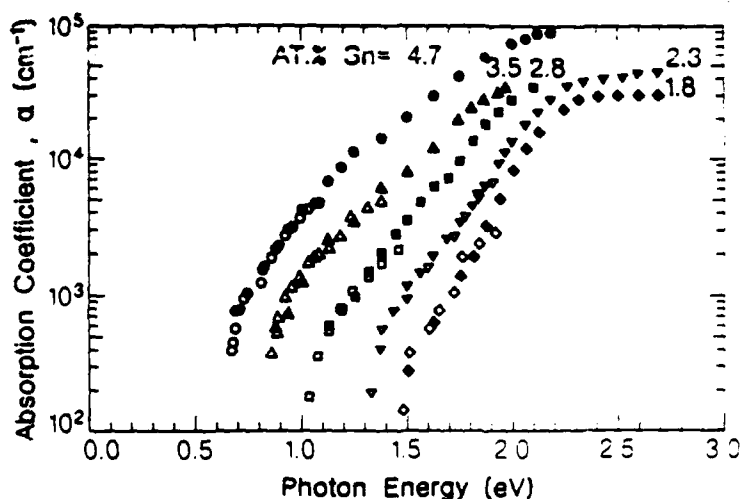


FIGURE 3. Optical absorption coefficient derived from optical (full symbols) and photoconductance (open symbols) data as a function of photon energy for a film prepared at 110°C. The tin concentrations are marked in the figure.

The photoconductivity (corrected for reflectance) is given by

$$\sigma_{ph} = qF\mu\tau [1 - \exp(-\alpha d)]/d,$$

where q is the absolute value of the electronic charge, F is the photon flux entering the sample, n is the quantum efficiency for photocarrier generation, u the photocarrier drift mobility, τ its lifetime, and d the sample thickness. The normalized photoconductivity

$$\sigma_{ph}' / qF\mu\tau = [1 - \exp(-\alpha d)]/d$$

as a function of photon energy is plotted in Fig. 4 for the same samples as in Fig. 3. The values of $\mu\tau$ derived from the saturation values of the photoconductivity are plotted in Fig. 5 on a logarithmic scale for two films prepared at 220°C (triangles) and 110°C (circles). For comparison, the value for an a-Si:H sample prepared at 220°C is also shown (square). We observe that the values of $\mu\tau$ for the high-temperature film start at a relatively high value of $5 \times 10^{-8} \text{ cm}^2/\text{V}$

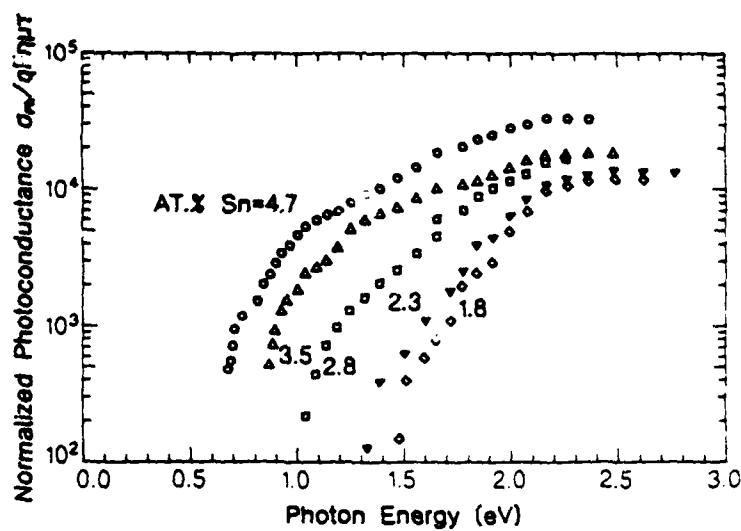


FIGURE 4. Normalized photoconductance as a function of photon energy for the same samples as in Fig. 3.

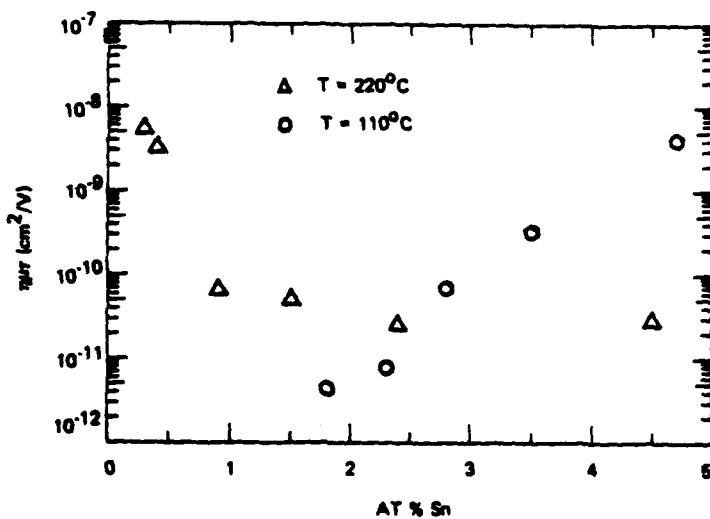


FIGURE 5. The photoconductance response as a function of tin concentration for two $a\text{-Sn}_{x}\text{Si}_{1-x}\text{:H}$ films prepared at 220°C (triangles) and 110°C (circles) and an $a\text{-Si:H}$ sample (square).

at very low tin concentration and drop rapidly as the tin concentration increases. From about 2 at.% Sn on, $\eta\mu\tau$ is fairly constant for this film. As for the low-temperature samples, we had difficulties preparing very low concentration Sn samples and thus could not measure in the Sn range where the strong drop in $\eta\mu\tau$ occurs. However, at higher concentrations this film shows a very rapid rise as the tin concentration increases.

DISCUSSION

Both Williamson et al. [18] and Anderson et al. [19] report that sputtered films prepared at higher argon pressures (~ 20 - 30 mTorr) tend to oxidize fairly heavily. It was found by Williamson et al. that in those samples the tin tended partially to crystallize. The low oxygen content of our samples thus seems to indicate that the films under study were amorphous.

The decrease in the optical gap upon alloying with tin was expected and actually the variation found in E_G with Sn concentration for the samples prepared at 220°C is not so different from that found by Williamson et al. [18] on their sputtered films. However, the much stronger variation of E_G with at.% Sn for samples prepared at 110°C shows that E_G is quite sensitive to the preparation temperature and, one would expect, also to the preparation technique used (sputtering, glow discharge). Films prepared by the glow-discharge method by Mahan et al. [17] exhibit a somewhat slower variation of the optical gap with Sn concentration. This may be due both to the different preparation technique and/or to the presence of C and Cl in the films, as pointed out by the authors.

The values of $\eta\mu\tau$ found here for the high-temperature samples (see Fig. 5) are smaller than those observed [12,13] for $Si_xGe_{1-x}:H$ alloys and show a strong initial decrease with tin concentration. The probable reason for this is that alloying with tin introduces a large density of defect states. This is evidenced also by the broad optical absorption edge (Fig. 4). The sharp increase in the value of $\eta\mu\tau$ with increasing tin concentration for the low-temperature samples

emphasizes again the difference in the electronic properties due to preparation temperature. It may be due to increasing effectiveness of new recombination states whose capture cross section for electrons must be quite small. Such behaviour has been observed²⁰ also on phosphorus doped hydrogenated amorphous silicon.

Our high-temperature results are not so unlike those published by Mahan et al. [17] for glow-discharge prepared films, the only published results on the photoconductivity of a-Sn_xSi_{1-x}:H that we are aware of. They find a sharp decrease of $\eta\mu\tau$ with tin concentration for the first ~ 2 at.% of Sn and then a very gradual increase with increasing Sn concentration. Mahan et al. attribute this behaviour to a transition from n-type to p-type conduction. It is possible that this is the case with our films as well, however, we have no evidence for such n to p transition.

In summary we measured the optical properties and photoconductivity of resistively sputtered a-Sn_xSi_{1-x}:H alloys. Both the gap and the photoconductivity parameters of the films are fairly sensitive to the preparation temperature. Our high-temperature results are not so unlike those published by others. The low-temperature results, however, are quite different and exhibit a stronger drop in E_G and a very fast rise in $\eta\mu\tau$ with increasing tin concentration.

ACKNOWLEDGMENT

This work was supported in part by US Army Research Office Grant DAAG29-84-G-0059 and in part by NSF-EPSCOR grant RII 8610677.

REFERENCES

- ¹ Y. Tawada, K. Tsuge, M. Kondo, H. Okamoto, and Y. Hamakawa, *J. Appl. Phys.* 53, 5273 (1982).
- ² G. Nakamura, K. Sato, and Y. Yukimoto, *Proc. Sixteenth IEEE PV Specialists Conf., San Diego, 1982*, p. 1331.
- ³ B. von Roedern, D. K. Paul, J. Blake, R. W. Collins, G. Moddel, and W. Paul, *Phys. Rev. B* 25, 7678 (1982).

- ⁴ R. S. Sussmann and R. Ogden, *Philos. Mag. B* 44, 137 (1981).
- ⁵ M. Le Coutelec, J. Richard, A. Guivarch, E. Ligeon, and J. Fontenille, *Thin Solid Films* 58, 407 (1979).
- ⁶ A. Morimoto, T. Muira, M. Kumeda, and T. Shimizu, *J. Appl. Phys.* 53, 7299 (1982).
- ⁷ D. Caffier, M. Le Coutelec, and J. Richard, *J. Phys. C* 42, 1037 (1981).
- ⁸ N. Van Dong, T. H. Dank, and J. Y. Leng, *J. Appl. Phys.* 52, 338 (1981).
- ⁹ W. Paul, D. K. Paul, B. von Roedern, J. Blake, and S. Orguz, *Phys. Rev. Lett.* 46, 1016 (1981).
- ¹⁰ T. Shimizu, M. Kumeda, and Y. Kiriyama, in Tetrahedrally Bonded Amorphous Semiconductors, AIP Conf. Proc. 73, 171 (1981).
- ¹¹ L. Chahed, C. Senemaud, M. L. Theye, J. Bullet, M. Galin, M. Gauthier, R. Bourdon, and M. Toulemonde, *Solid State Commun.* 45, 649 (1983).
- ¹² S. Z. Weiss, M. Gomez, J. A. Muir, O. Resto, R. Perez, Y. Goldstein, and B. Abeles, *Appl. Phys. Lett.* 44, 634 (1984).
- ¹³ S. Z. Weiss, Y. Goldstein, M. Gomez, J. A. Muir, O. Resto, and R. Perez, *Thin Solid Films* 119, 59 (1984).
- ¹⁴ S. Z. Weiss, M. Gomez, J. A. Muir, O. Resto, R. Perez, and Y. Goldstein, *Appl. Phys. Commun.* 4, 1 (1984).
- ¹⁵ H. Itozaki, N. Fujita, T. Igarashi, and H. Hitotsuyanagi, *J. Non-Crystalline Solids* 59-60, 589 (1983).
- ¹⁶ D. L. Williamson, R. C. Kerns, and S. K. Deb, *J. Appl. Phys.* 55, 2816 (1984).
- ¹⁷ A. H. Mahan, D. L. Williamson, and A. Madan, *Appl. Phys. Lett.* 44, 220 (1984).
- ¹⁸ G. D. Cody, C. R. Wronski, B. Abeles, R. B. Stephens and B. Brooks, *Sol. Cells* 2, 227 (1980).
- ¹⁹ D. A. Anderson, G. Moddel, M. A. Paesler, and W. Paul, *J. Vac. Sci. Technol.* 16, 906 (1979).
- ²⁰ C. R. Wronski, B. Abeles, T. Tiedje, and G. D. Cody, *Solid State Commun.* 44, 1423 (1982).

Calibration of oxygen Auger signal from single-crystal ZnO surfaces

S. Z. Weisz and O. Resto

Department of Physics, University of Puerto Rico, Rio Piedras, Puerto Rico 00931

G. Yaron, A. Many, and Y. Goldstein

Racah Institute of Physics, Hebrew University, Jerusalem, 91904 Israel

(Received 29 September 1986; accepted 4 January 1987)

The Auger spectra of the polar and prism surfaces of single-crystal ZnO were measured. The sensitivity factors derived from the differentiated spectra are 0.26 and 0.25 for a beam energy of 3 and 5 keV, respectively. These values agree fairly well with the theoretical calculations of Mroczkowski and Lichtman.

I. INTRODUCTION

ZnO crystallizes in the hexagonal wurtzite structure with alternating zinc and oxygen layers perpendicular to the hexagonal *c* axis. A platelet cut perpendicularly to the *c* axis always ends up with one "zinc" (0001) face and one "oxygen" (000 $\bar{1}$) face, commonly called the polar surfaces. The (1010) face, parallel to the *c* axis, is usually referred to as the prism or checkered face, and contains an equal number of zinc and oxygen atoms.¹

We became interested in ZnO because of the large free-electron densities that can be obtained on its surface.²⁻⁵ Accumulation layers with an electron surface density of $1-2 \times 10^{14} \text{ cm}^{-2}$ are readily attainable on ZnO surfaces, making ZnO eminently suitable for the study of quantization effects⁶ in narrow surface channels.

During our investigations of the clean (000 $\bar{1}$) face (the oxygen surface) we noticed that the ratio of the Auger signals due to oxygen and to zinc is too small. Using the sensitivity factors from the *Handbook of Auger Electron Spectroscopy* (the Handbook)⁷ we calculated less than 20% oxygen on the oxygen surface. This prompted us to a more thorough investigation of the relative concentrations of oxygen and zinc on the polar and prism surfaces.

II. SAMPLE PREPARATION

Platelets of semiconducting ZnO single crystals grown by the hydrothermal method were supplied by the Airtron Co. The dimensions of the platelets were $10 \times 10 \times 1 \text{ mm}^3$. Platelets with both the hexagonal *c* axis perpendicular to the large surfaces (polar surfaces) and parallel to the large surfaces (prism surfaces) were used. The samples were cut to typical dimensions of $10 \times 3 \times 1 \text{ mm}^3$, mechanically lapped to a flatness of $1 \mu\text{m}$, cleaned, and etched in HCl. After the etch the samples were mounted in the vacuum chamber of a Physical Electronics model 560 scanning Auger microprobe where the large surfaces were cleaned by repeated cycles of argon-ion bombardment and annealing at 360°C .

III. RESULTS

Several (at least six) Auger surveys were taken of each surface and at each beam voltage to check the reproducibility of the results. The position along the surface was also moved, to check uniformity. Both 3- and 5-keV electron beam energies were employed, with a $1-\mu\text{A}$ beam current,

and analyzer energy resolution of better than 0.4%. We used both the single-spot mode and the rastering mode, the latter covering an area of $0.3 \times 0.3 \text{ mm}^2$.

The relative oxygen and zinc concentrations on each surface were derived from the ratio of the peak-to-peak amplitudes of the oxygen *KLL* (510 eV) line to the zinc *LMM* (994 eV) line. This ratio, to be denoted by O_{KLL}/Zn_{LMM} , was found to be reproducible within 1% for the 5-keV beam energy, and within 2%-3% for the 3-keV beam energy. Typical $d[N(E)]/dE$ results of Auger surveys for the three different ZnO surfaces, using a beam energy of 5 keV, are shown in Fig. 1. As can be seen in the figure, the surfaces are clean and the Auger surveys of the different faces are qualitatively very similar. The widths of the oxygen and zinc lines are 9 eV for the O_{KLL} and 6 eV for the Zn_{LMM} line. There are, however, some quantitative differences in the amplitudes of the oxygen and zinc lines. Results obtained at 3 keV were similar, except that the oxygen-to-zinc ratio was somewhat larger. In Table I, column 3, we list the average values of the ratio of the oxygen to zinc line strength O_{KLL}/Zn_{LMM} for the

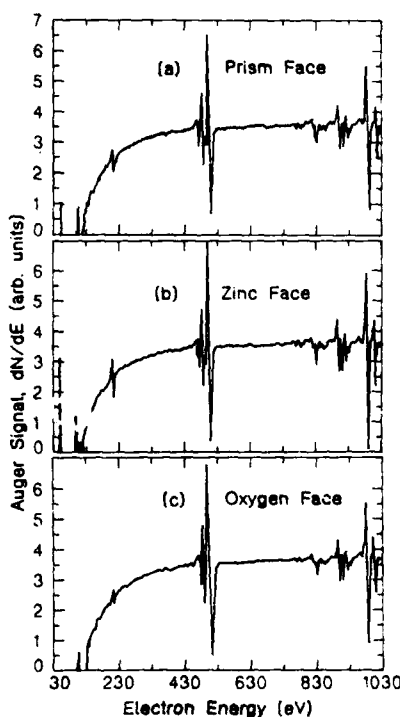


FIG. 1. Differentiated Auger spectra, $d[N(E)]/dE$, for three different ZnO faces as marked. The line at 510 eV is the oxygen *KLL* line and that at 994 eV is the *Zn LMM* line.

TABLE I. Effective oxygen surface concentration.

Surface	Beam energy (keV)	O_{KLL}/Zn_{LMM}	Oxygen concentration from		
			Handbook	Mroczkowski and Lichtman	Present results
Prism	3	1.51	0.33	0.48	0.50
Zinc	3	1.51	0.33	0.48	0.50
Oxygen	3	1.75	0.37	0.51	0.54
Prism	5	1.26	0.39	0.53	0.50
Zinc	5	1.15	0.37	0.51	0.48
Oxygen	5	1.37	0.41	0.55	0.52

different surfaces and the two beam energies. Several Auger sensitivities for oxygen in ZnO were used for the calculation of the effective oxygen surface concentration: the Handbook⁷ values, values calculated by Mroczkowski and Lichtman,⁸ and values proposed by us based on the present results. These latter sensitivities were determined by imposing the requirement that the prism surface contain an equal number of oxygen and zinc atoms. The different sensitivity factors for oxygen are listed in Table II. The sensitivities used for zinc in all our calculations are as listed in the Handbook, 0.17 at 3 keV and 0.20 at 5 keV. These same values were used also by Mroczkowski and Lichtman and, in fact, served as their normalization points.

The different oxygen concentrations derived by using the sensitivity factors in Table II, are listed in columns 4, 5, and 6 in Table I. It is apparent that the concentrations based on the sensitivities of Mroczkowski and Lichtman are fairly close to those obtained from the sensitivities proposed here, and are both in the vicinity of 0.5. In contrast, the values derived using the Handbook sensitivities are much lower. Moreover, for the Handbook sensitivities we should have used the line strengths of $d[EN(E)]/dE$ instead of $d[N(E)]/dE$, at least we were so advised by Physical Electronics upon inquiry (even though there seems to be some confusion about the issue). Using $d[EN(E)]/dE$ would further reduce the calculated oxygen concentration, approximately by a factor of 0.5, yielding values below 0.2 in column 4 of Table I.

IV. DISCUSSION

The low values (below 0.2) for the oxygen surface concentrations derived by using the Handbook sensitivities are unacceptable for several reasons. First, if such a large deficit of oxygen did exist on any of the ZnO surfaces it would have long been detected¹ by low-energy electron diffraction.

TABLE II. Relative Auger sensitivities to oxygen.

Beam energy (keV)	Sensitivity to oxygen from		
	Handbook	Mroczkowski and Lichtman	Present results
3	0.51	0.28	0.26
5	0.40	0.22	0.25

Moreover oxygen deficiency is known^{2,9-12} to enhance the surface conductivity, but no such enhancement was observed in the present measurements. On the contrary, annealing in vacuum after sputter cleaning was always found to restore the high surface resistance prior to sputtering.² Finally, we performed annealing experiments in the presence of oxygen without any appreciable change in O_{KLL}/Zn_{LMM} .

It seems to us that the only explanation for a large oxygen deficiency, if such deficiency exists, would be that the electron beam promotes oxygen desorption. However, this cannot be reconciled with the fact that Auger surveys in the spot mode (with a spot diameter of a few μm) yielded the same results as those employing the raster mode. In the latter case an area larger by a factor of about 10^4 is scanned, thereby reducing the average beam intensity by the same factor. In addition, it is very difficult to see how electron-promoted oxygen desorption would be equally effective on all three crystallographic faces. In particular, one would expect that electron desorption from the zinc face, where the oxygen atoms are essentially protected by the outer layer of zinc atoms, would proceed, if it occurred at all, much less efficiently than from the oxygen face where the oxygen atoms are located at the outer layer.

In view of the above arguments it appears that the sensitivity factors for oxygen given by the Handbook⁷ are inapplicable to the case of ZnO. The approximate equality of the measured O_{KLL}/Zn_{LMM} ratio for the different faces strongly supports the assumption used above that the oxygen concentration on the prism surface equals 0.5. The oxygen concentrations derived for the other surfaces by using this assumption seem very reasonable and are in fairly good agreement with those based on the theoretical sensitivity factors of Mroczkowski and Lichtman. The sensitivities deduced from our results differ by about 10% from those of Mroczkowski and Lichtman and are essentially independent of electron energy between 3 and 5 keV.

It is quite likely that the large discrepancy between our sensitivity factors for oxygen and those of the Handbook⁷ is due to the fact that the oxygen line in the Handbook was measured on MgO, where it is, apparently, appreciably narrower than the width of 9 eV, obtained by us on ZnO. The latter width is real and well above the instrumental resolution (better than 2 eV for the oxygen line). Thus it seems that, at least for oxygen, the peak-to-peak amplitude of the

differentiated Auger spectrum is not a unique measure of the concentration. Rather, $N(E)$ (or the area under the differentiated line) may be a better measure of the concentration. We plan in the future to extend our studies to several other oxides to check this point.

In conclusion, measurements on the polar and prism surfaces of ZnO indicate that the sensitivity factors for oxygen listed in the Handbook are inapplicable to ZnO. On the other hand, the oxygen sensitivity factors derived on the basis of the present results yield reasonable values for the oxygen concentration, and are in fairly good agreement with the theoretical calculations of Mroczkowski and Lichtman.⁸

ACKNOWLEDGMENT

This work was supported in part by U. S. Army Research Office Grant No. DAAG29-84-G-0059.

¹See, for instance, review article by D. Hofmann, in *Zinc Oxide*, edited by W. Hirschwald, P. Bonasewicz, L. Ernst, M. Grade, D. Hofmann, S. Krebs, R. Litbarski, G. Neumann, M. Grunze, D. Kolb, and H. J. Schulz, Vol. 7 of *Current Topics in Materials Science*, edited by E. Kaldus (North-Holland, Amsterdam, 1981), p. 304.

²G. Yaron, A. Many, and Y. Goldstein, *J. Appl. Phys.* **58**, 3508 (1985).

³G. Yaron, J. Levy, Y. Goldstein, and A. Many, *J. Appl. Phys.* **59**, 1232 (1986).

⁴G. Yaron, J. Levy, A. Many, Y. Goldstein, S. Z. Weiz, and O. Resto, *J. Phys. Chem. Solids* **47**, 401 (1986).

⁵G. Yaron, Y. Goldstein, and A. Many, *Appl. Phys. Lett.* **49**, 561 (1986).

⁶See, for instance, *Surf. Sci.* **142** (1984); **170** (1986).

⁷L. E. Davis, N. C. MacDonald, P. W. Palmberg, G. E. Riach, and R. E. Weber, *Handbook of Auger Electron Spectroscopy*, 2nd ed. (Physical Electronics, Eden Prairie, 1976).

⁸S. Mroczkowski and D. Lichtman, *J. Vac. Sci. Technol. A* **3**, 1860 (1985).

⁹G. Heiland and P. Kunstmann, *Surf. Sci.* **13**, 72 (1969).

¹⁰G. Heiland, E. Molwo, and F. Stockman, *Solid State Phys.* **8**, 193 (1958).

¹¹D. Eger, Y. Goldstein, and A. Many, *RCA Rev.* **36**, 508 (1975).

¹²Y. Grinshpan, M. Nitzan, and Y. Goldstein, *Phys. Rev. B* **19**, 1098, 4107 (1979).

INFRARED SPECTROSCOPY OF a-Si_{1-x}Sn_x:H FILMS

R.S. Katiyar, O. Resto, R. Perez, M. Gomez and Z. Weisz

Department of Physics, University of Puerto Rico,
Rio Piedras, PR 00931

Abstract

Several hydrogenated amorphous Si_{1-x}Sn_x alloy films of thicknesses varying between four to eight thousand angstroms were prepared on impurity free silicon substrates using reactive co-sputtering technique. The tin concentration that varied among different samples from 0 to 10.7 %, was determined using Auger depth profile. The oxygen contamination increased with the tin concentration but it was found to be uniform all over the thickness of the films. Samples were characterized using SIMS to detect the presence of various molecular species. The infrared measurements showed vibrational bands characteristics of Si-H, Sn-H, Si-O and perhaps Sn-O. The presence of Sn is found to facilitate the formation of more Si-H than SiH₂ bonds. Si-O band shifts to 1075 cm⁻¹ from 1030 cm⁻¹ as the Sn concentration is increased to .1 %. Additionally there is a new peak at 1155 cm⁻¹ appearing in the mixed samples with Sn concentration over 10 %.

1. INTRODUCTION

Hydrogenated binary alloys of Si with Ge, Sn, C, and N have gathered considerable attention because of their use in the fabrication of devices such as solar cell, photosensors and thin film transistors¹⁻³. Alloys containing Sn are perhaps the least studied in this series. The optical band gap in amorphous Si-Sn alloy decreases systematically with increase in Sn concentration^{4,5} and it becomes possible, at least in principle, to prepare application oriented samples with desired energy gap. Since the vibrational spectroscopy is known to play important role in the characterization of such amorphous materials, we have carried out infrared measurements on a-Si_{1-x}Sn_x:H films prepared in our laboratory.

2. FILM PREPARATION

The a-Si_{1-x}Sn_x:H films were prepared in a conventional reactive sputtering unit on Si substrates with 50 W of RF (13.56 MHz) power and cathode self-bias voltage of -900 V, in a gas mixture of argon at 12 mTorr and hydrogen at 2 mTorr. The sputtering target consisted of a silicon disc of about 15 cm in diameter and a couple of tin pieces (about 1 cm in diam.) placed at one end of silicon disc. The substrate was heated to about 230°C during the deposition. The usual deposition time was about 10 hours. The method produced a film of Si-Sn with a compositional variation along its length. The Si-Sn film was about 5 cm long over the substrate, which was then cut into five equal pieces to produce five Si_{1-x}Sn_x:H samples with different x. We also prepared a hydrogenated Sn film of about 400 Å thickness under the same conditions.

The characterization of the films was carried out using Auger electron microprobe (AEM) and secondary ion mass spectroscopy (SIMS). We used depth profiling to determine the uniformity of the composition of the film throughout the sample thickness. In this method the sample surface is peeled-off by controlled argon-ion sputtering while continuously monitoring the Auger spectrum. Except for the surface layer of a few angstroms the composition of the films was found to be quite uniform. The five Si-Sn samples, namely A, B, C, D and E had varying concentrations of Sn, viz <0.1, 0.1, 0.6, 1.6 and 10.7 % respectively. All films were found to contain oxygen. The oxygen concentration was found to be higher for films containing higher Sn concentration and it was uniform all over the film thickness. The presence of oxygen, therefore, could not be attributed to postdeposition oxidation as suggested by Williamson et al⁷. The oxygen contamination on the surface layers, however, was found to be at least twice higher than the bulk. Even in the sample "A" that had tin concentration of less than 0.1 %, the oxygen concentration was approximately 2.9 %. Other samples, namely B, C, D and E had the oxygen concentrations of 4.5, 5.5, 7.3 and 12.2 % respectively. The oxygen contents in a pure a-Sn:H film (sample "F") were found to be only 1.8 %. However, pure a-Si:H film (sample "G") prepared under similar conditions did not show any oxygen contamination. We, therefore, analysed our tin targets by Auger Spectroscopy that revealed the presence of oxygen in them

to about 1.5 %. This should explain the source of oxygen contamination over the thickness of the films.

The presence of molecular species in the films was characterized using SIMS. The $\text{Si}_x\text{Sn}_{1-x}\text{H}$ films with x less than 0.6 % revealed traces of CH_2 , SiH , SiH_2 , SiH_3 , SiO_x , SiOH , SiOSi , SiCOSi , SiHSi , SiSi , SnH_n , SiSn along with the presence of Si, Sn, O and H elements and films with $x > 1\%$ contained traces of SnO and SiOSn in addition to the above species. Similar analysis of a-Sn sample and a tin target revealed the presence of SnO species along with the peak characteristic of Sn. All of the samples showed traces of Na, K, Al and Li. This is due to the impurities present in the ordinary water that was used to clean the substrates.

3. INFRARED MEASUREMENTS

In order to carry out infrared absorption studies we utilized a Nicolet 6000 Fourier transform infrared spectrometer (FTIR). The parameters were chosen to give a resolution of 4 cm^{-1} in the range of 4000 to 400 cm^{-1} . The absorption spectra from five hydrogenated Si - Sn samples are shown in Figure 1. In Figure 2, we have plotted infrared absorption spectra from a-Si and a-Sn films. These data have not been corrected for interference fringing effect caused by difference in the index of refraction of the amorphous film and the substrate. Moreover, the spectra have been displaced along the absorption axis (y-axis) in order for clarity. Some of the spectra show CO_2 bands around 2361 and 2337 cm^{-1} due to poor subtraction of the background spectra.

4. DISCUSSION

The a-Si:H film (Figure 2) showed absorption peaks at 2096 , 2010 cm^{-1} (sh), 898 , 845 , 797 (weak) and 643 cm^{-1} . The peaks at 2096 and 2010 cm^{-1} are assigned to SiH_2 and SiH stretching modes respectively. The SiH_2 bending modes appear at 898 and 845 cm^{-1} and the 643 cm^{-1} mode is due to SiH_2 wagging. In hydrogenated Si - Sn spectra (Figure 1.) we notice several changes as the Sn concentration increases. There is a gradual decrease in the intensity of SiH_2 peak whereas the peak intensity due to SiH mode increases. This is attributed to the formation of more SiH bonds instead of SiH_2 bonds with the increase in Sn concentration. In fact even with a Sn concentration

of 0.1 % (sample "B") the SiH peak appears as intense as SiH₂ peak. Moreover, as expected there is a slight decrease (about 5 cm⁻¹) in the SiH₂ peak frequency due to the presence of Sn.

As the Sn concentration increases to 10.7 % (sample "E") in Si-Sn film, the absorption edge moves well within the mid infrared range and it was not possible to extract SiH peak from the strong absorption. In fact the strongest peak characteristic of SiH₂ wagging at 643 cm⁻¹ also disappears or becomes very weak in sample "E". There is, however, a new weak peak appearing around 1725 cm⁻¹ that could be interpreted due to SnH vibrations. It may be worth quoting that the stretch mode frequencies for SiH₄, GeH₄ and SnH₄ molecules are at 2183, 2114 and 1901 cm⁻¹ respectively and the corresponding bending mode frequencies are at 910, 819 and 677 cm⁻¹ respectively.

As mentioned earlier the oxygen concentration increases in the hydrogenated Si-Sn films along with the increase in Sn concentration. This is evident from the appearance of a new peak characteristic of Si-O absorption in the region of 1000 to 1100 cm⁻¹ in comparison to a-Si:H spectrum. In sample "A" the Si-O peak is at 1030 cm⁻¹ that moves to about 1075 cm⁻¹ as the Sn concentration is increased to 0.1 % (sample "B"). Sample "B" has an oxygen concentration of 4.5 %. In sample "E" (Sn concentration 10.7 % and oxygen concentration 12.2 %) this peak is considerably stronger as compared to samples with the smaller Sn and O concentrations. Moreover, there is a new peak around 1155 cm⁻¹ in this sample (appearing as shoulder to the 1075 cm⁻¹ peak), that is well beyond the Si-O range. In order to understand some of these features we prepared an amorphous Sn:H film (about 400 Å thick) on Si substrate. Its infrared absorption spectrum is shown in Figure 2. Although the spectrum is a bit noisy the two strong peaks centered around 1164 and 1080 cm⁻¹ can be easily identified. These peaks appear nearly at the same positions as in the Si-Sn spectrum with tin concentration of 10.7 %. Moreover, the a-Sn:H spectrum contains a peak around 440 cm⁻¹ that may be due to Sn-O vibrations. Similarly the features around 1730 and 570 cm⁻¹ may be assigned to SnH stretching and bending vibrations respectively.

Our non-hydrogenated Si-Sn films did not show any significant oxygen when characterizing them by Auger electron spectroscopy and SIMS. This indicates that while depositing the film by sputtering the presence of hydrogen

facilitates the formation of Si-O or Si-OH bonds. The oxygen presumably comes from Sn-O present in tin targets.

ACKNOWLEDGEMENT

This work was supported in part by the EPSCoR Program of National Science Foundation and by U.S. Army Research Office Grant DAAG29-84-G-0059.

REFERENCES

1. Y. Hamakawa, Proceedings of the Materials Research Society Symposia, 49, 239 (1985).
2. Y. Kuwano, Proceedings of the Materials Research Society Symposia, 70, 455 (1986).
3. Y. Tawada, K. Tsuge, M. Kondo, H. Okamoto, and Y. Hamakawa, J. Appl. Phys. 53, 5273 (1982).
4. H. Itozaki, N. Fujita, T. Igarashi and H. Hitotsuyanagi, J. Non-Crystalline Solids, 59-60, 589 (1983).
5. R. Perez, O. Resto, S.Z. Weisz and Y. Goldstein, ~~Appl.~~ Appl. Phys. COHH. (accepted).
6. M.H. Brodsky, M. Cardona and J.J. Kuomo, Phys. Rev. B16, 3556 (1977).
7. D.L. Williamson, R.C. Kerns and S. K. Deb, J. Appl. Phys. 55, 2816 (1984).
8. K. Nakamoto, Infrared and Raman Spectra of Inorganic and Coordination Compounds, (Wiley-Interscience, New York, third Edition, 1978) pp134.

FIGURE CAPTIONS

Figure 1. Infrared absorption spectra of a-Si_{1-x}Sn_x:H films. The spectra have been scale adjusted along the absorption axis for clarity. Tin and oxygen concentrations in each film are as follows: (A) <1% Sn, 2.9% O; (B) .1% Sn, 4.5% O; (C) .6% Sn, 5.5% O; (D) 1.6% Sn, 7.3% O; (E) 10.7% Sn, 12.2% O.

Figure 2. Infrared absorption spectra of (F) a-Sn:H and (G) a-Si:H films. The spectra have been scale adjusted along the absorption axis for clarity.

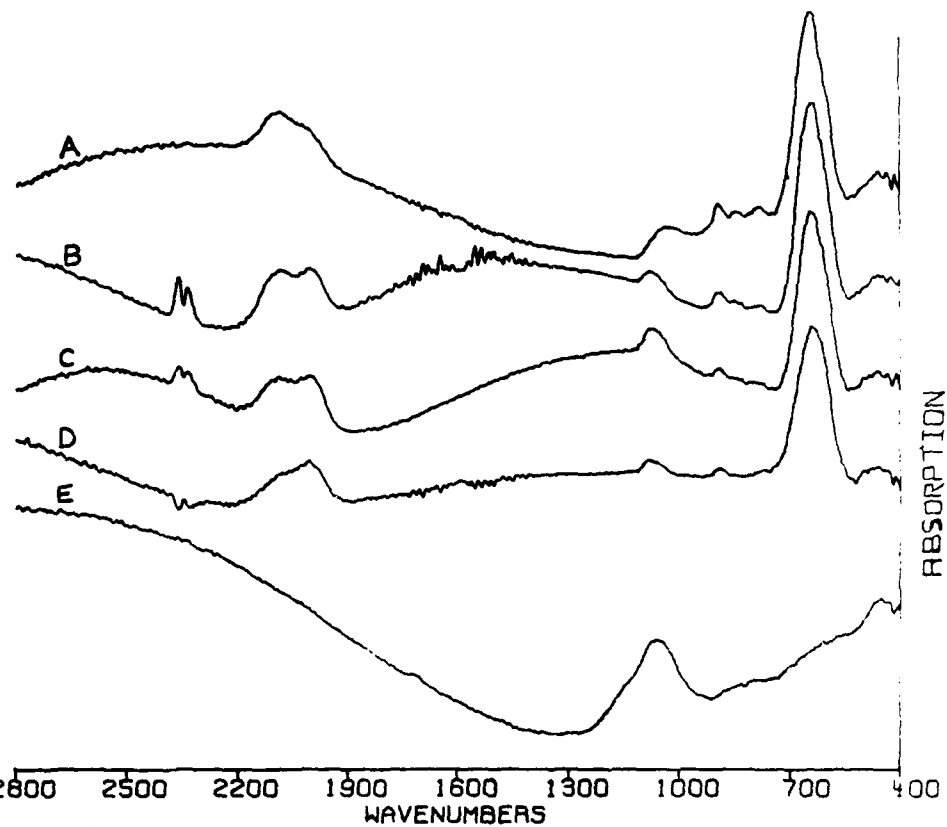


FIGURE 1

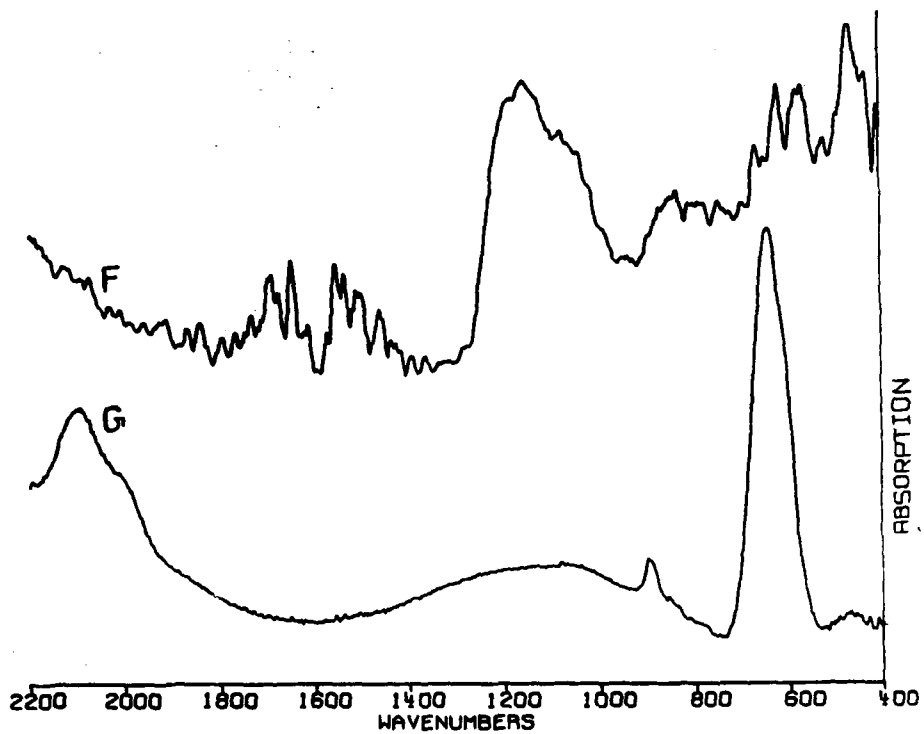


FIGURE 2

FILE: 007828APL 1 QUEUE:APL-APL
IS: pasteup FMT: aipxr
BY:OCR;26/05,18:47 REV: MARGA;27/05,17:21
27-MAY-88 20:22:17

007828APL = 007828APL

Auger electron spectroscopy for quantitative analysis

A. Many and Y. Goldstein
Racah Institute of Physics, The Hebrew University, Jerusalem 91904, Israel

S. Z. Weisz and O. Resta
Department of Physics, University of Puerto Rico, Rio Piedras, Puerto Rico 00931

(Received 16 December 1987; accepted for publication 10 May 1988)

A simple mathematical analysis shows that unless the ratio of the instrumental resolution width to the natural Auger linewidth is less than about 0.3, the measured line intensities do not represent accurately the atomic concentrations. To overcome this difficulty, a universal curve is presented whereby the experimentally measured line intensities can be corrected so as to represent quite accurately the relative atomic concentrations in one's sample. Unfortunately, however, the available sensitivity data required for quantification were not always measured with sufficient instrumental resolution. It is our contention that there is a need for new sensitivity measurements in which the required resolution is ensured.

For a quantitative determination of atomic concentrations by Auger electron spectroscopy (AES), one usually measures^{1,2} the peak-to-peak amplitudes of the Auger signal derivatives $dN(E)/dE$, to be referred to as the "derivative amplitudes" $\Delta(dN/dE)$, where $N(E)$ is the energy distribution of the Auger electron intensity. The derivative is measured by the analyzer modulation technique or by computer differentiation of the measured $N(E)$ curve. The effect of the modulation amplitude on the derivative spectrum has been extensively studied, primarily by Seah and co-workers.³⁻⁷ These workers showed that as long as the ratio of the peak-to-peak modulation amplitude to the measured Auger linewidth is less than about 0.7, the measured signal represents accurately the derivative. As to computer differentiation, Seah *et al.*⁸ showed that it is equivalent in this respect to amplitude modulation, with the energy excursion used for computing the derivative replacing the peak-to-peak modulation amplitude (apart from a factor close to unity).

Even if the derivative amplitudes were determined precisely, whether by modulation or by computer differentiation, the remaining important question in quantification is how accurately the derivative amplitudes represent the relative atomic concentrations in a given sample. The analyzer resolution is a very important factor in this respect, and in the present letter we examine its effect on the derivative amplitude. It is shown both theoretically and experimentally that only if the ratios of the instrumental resolution width to the natural width for all the elements under study are smaller than about 0.3, are the magnitudes of the corresponding derivative amplitudes truly representative of the atomic concentrations. In order to derive quantitatively the actual concentration one needs, in addition, reliable Auger sensitivities of the elements involved. The best procedure is to measure the sensitivities *in situ*. Usually, however, one relies on predetermined sensitivities. Several compilations of such sensitivities have been published.⁹⁻¹² Unfortunately, most of the sensitivity measurements were taken with the commonly available energy resolution of about 0.5% of the Auger energy, corresponding, for example, to 5 eV at an energy of 1000 eV. Since the natural width of many elements ranges between 1.5 and 4 eV, it is unavoidable that the above-mentioned requirement that the width ratio be smaller than 0.3 may not be always satisfied. For example, as will be shown below, there is reason to believe that at least some of the measurements in the Handbook of AES by Davis *et al.*,⁹ perhaps the most commonly used compilation, were performed with inadequate resolution. We therefore believe that a revision of the sensitivity data is advisable. We show here that once high-resolution sensitivity data become available, the user would be able to derive atomic concentrations accurately, even if his own instrumental resolution is quite poor: a procedure is described whereby the experimentally measured derivative amplitudes can be corrected so as to yield the correct atomic concentrations.

It should be noted that the effect on the derivative amplitude of modulation amplitude discussed by Seah and co-workers³⁻⁷ and of analyzer resolution considered here are two totally different issues. The former deals with the accuracy with which the derivative amplitudes are measured, whereas the latter is concerned with how close the derivative amplitudes, even if determined accurately, represent the atomic concentrations in the sample. Other instrumental

factors affecting the accuracy of the derivative amplitudes, such as reproducibility¹³ and the variation of the electron multiplier efficiency with electron energy,⁹ have been discussed in the literature, and will not be considered here.

In the following analysis we evaluate the derivative amplitudes assuming Gaussian line shapes for both the Auger lines and the analyzer's resolution functions. This is a realistic representation since both shapes are usually not far off from Gaussian. Also, the results of the analysis are not expected to depend critically on the precise line shapes used. With these assumptions, the Auger electron distribution $N(E)$ in the vicinity of the i th energy peak E_i is proportional to

$$N_i(E) \propto \int \exp\left(-\frac{(E - E_i)^2}{2\sigma_i^2}\right) \exp\left(-\frac{(E - E_i)^2}{2\sigma_r^2}\right) dE, \quad (1)$$

where σ_i is the peak's natural width and σ_r is the width of the resolution function: the integration is to be performed in the neighborhood of the i th peak. The derivative is obtained by differentiating the integrand with respect to E :

$$\frac{dN_i(E)}{dE} \propto \int \left[1 + \left(\frac{\sigma_r - E}{\sigma_r} \right) \left(\frac{d\sigma_r}{dE} \right) \right] f(E, E_i, \sigma_i, \sigma_r, \mathcal{E}) dE, \quad (2)$$

where

$$f(E, E_i, \sigma_i, \sigma_r, \mathcal{E}) = \left(\frac{\sigma_r - E}{\sigma_r^2} \right) \exp\left(-\frac{(\mathcal{E} - E_i)^2}{2\sigma_i^2}\right) \times \exp\left(-\frac{(\mathcal{E} - E)^2}{2\sigma_r^2}\right). \quad (3)$$

The second term in the large brackets of Eq. (2) originates from the energy dependence of σ_r (usually $\sigma_r \propto E$). Actually, however, this term is very small compared to unity and can safely be neglected: in most analyzers $d\sigma_r/dE$ is less than 0.005, while $|(\mathcal{E} - E)/2\sigma_r|$ is of the order of unity or less throughout the effective range of integration. Thus, by measuring the energies in units of the resolution width and shifting the origin to E_i , i.e., by substituting $x = (\mathcal{E} - E_i)/\sigma_r$ and $y = (E - E_i)/\sigma_r$, we obtain

$$\frac{dN_i(E)}{dE} \propto \int g\left(\frac{x, y, \sigma_r}{\sigma_i}\right) dx, \quad (4)$$

where

$$g\left(\frac{x, y, \sigma_r}{\sigma_i}\right) = (x - y) \exp\left(-\frac{x^2}{2(\sigma_i/\sigma_r)^2}\right) \exp\left(-\frac{(x - y)^2}{2}\right). \quad (5)$$

In this form, the integral becomes a universal function of y , depending only on the parameter σ_i/σ_r . Actually, because we are dealing with derivatives, more suitable parameters than σ_i and σ_r would be the energy separation for each Gaussian between the positive and negative derivative peaks, to be referred to as the resolution width W_r and the natural width W_i , respectively. Obviously $W_r = 2\sigma_r$ and $W_i = 2\sigma_i$.

The solid curve in Fig. 1 is a universal plot of the derivative amplitude $\Delta(dN/dE)$ against the ratio W_r/W_i , as calculated by integration of Eq. (4). We note that starting at the origin, $\Delta(dN/dE)$ increases with increasing resolution width, attains a maximum at $W_r/W_i = 1$, and then decreases. This behavior is a result of two competing processes: $N(E)$ increases with increasing resolution width but at the same time the measured line also widens and eventually the derivative decreases. The behavior depicted in Fig. 1 has far reaching consequences concerning the use of Auger measurements for quantitative analyses. The derivative amplitude is a direct measure of the atomic concentration only in the linear range of the curve ($W_r/W_i < 0.3$). The relative magnitudes of the derivative amplitudes of the different Auger lines are then independent of the analyzer resolution and truly represent the relative atomic concentrations in the sample under study. Only in this linear range is the procedure, sometimes adopted, of dividing each derivative amplitude by W_r or, equivalently, by E meaningful. For larger W_r/W_i , the $1/E$ normalization, undertaken in an attempt to compensate for the increasing resolution width with E , is less adequate and becomes outright meaningless for $W_r/W_i > 1$.

There is, however, a simple procedure to correct the measured derivative amplitudes for $W_r/W_i > 0.3$ so as to make the results meaningful. One derives from the universal curve of Fig. 1 the values one would have measured were the analyzer resolution sufficiently good. To do that, one multiplies the measured derivative amplitude for each element (each W_r/W_i) by a correction factor, given by the ratio of the value read off the extrapolated linear section of the curve (dashed line in Fig. 1) to that of the actual value on the curve at that abscissa.

To illustrate the above considerations we present in Fig. 2 measured AES results for MgO, taken at different instrumental resolutions. The derivative spectra were obtained by five-point computer differentiation⁸ of the measured $N(E)$ spectra, with a ± 1 eV overall excursion. The "differentiation potential" δ is thus 2 eV, which is less than 0.7 of the measured widths of all lines in Fig. 2. Hence this procedure yields accurate values for the derivative spectra.⁹ The resolution widths W_r at the oxygen and magnesium peak energies are marked on the figures. The natural oxygen and magnesium widths, 2.9 and 3.3 eV, respectively, were derived from the data of Fig. 2(a) (measured with the higher resolution) using the calculated values of the integral in Eq. (2). We thus conclude that the width ratios W_r/W_i for oxygen and magnesium are 0.31 and 0.67, respectively. We see that the value of W_r/W_i for Mg is appreciably larger than 0.3, so that even for our better resolved data (W_r/E of only 0.2%!) a significant correction to the measured Mg derivative amplitude should be applied. The correction factor, as evaluated from Fig. 1, is 1.45. To be precise, a small correction of 1.09 should be applied also to the oxygen line. Hence the measured ratio of the two derivative amplitudes, 1.9, should be multiplied by 1.09/1.45 to yield the corrected ratio of 1.4.

The resolution widths in Fig. 2(b) were purposely made larger, as indicated in the figure. Whereas the W_r/W_i value for oxygen is still reasonable, that for magnesium (1.8) becomes very much larger than 0.3. This is exhibited by the dramatic decrease of the magnesium derivative amplitude and the increase of the measured oxygen to magnesium amplitude ratios: from 1.9 in Fig. 2(a) to 3.1 in Fig. 2(b). In order to demonstrate the usefulness of Fig. 1 we shall also derive the corrected derivative amplitude ratio from the poorer resolved ($W_r/E \gtrsim 0.5\%$) data of Fig. 2(b). Using the correction procedure outlined above, we find for the corrected ratio of oxygen to magnesium derivative amplitudes the value of 1.3. This differs by no more than 10% from the value derived from the better resolved data of Fig. 2(a). It should be noted that if no correction were applied, the data in Fig. 2(b), for example, would have led to an error of a factor of over 2 in the oxygen to magnesium concentration ratio. Obviously, much larger errors would be incurred for less resolved data and/or higher energy Auger lines.

We have also evaluated the oxygen to magnesium derivative amplitude ratio from the MgO Auger spectrum appearing in the Handbook of AES.⁹ The value obtained is 3.2, very close to the result of our less resolved data (3.1), in which W_r/W_i appreciably exceeds the value of 0.3 for both elements. This shows that at least some of the sensitivity data in this Handbook were measured with insufficient resolution.

In conclusion, we maintain that the available sensitivity data should be revised in the light of the requirement $W_r/W_i < 0.3$. Particular attention should be given to the high-energy Auger lines, for which the resolution is necessarily less good. For such lines, W_r/W_i could easily exceed the value of 0.3, possibly by quite a large margin. The natural linewidths W_i of all the elements should also be included in the revised sensitivity compilation, so as to enable the user to check his own resolution against these values. The user would then be able to carry out a quantitative analysis even if his own instrumental resolution is rather poor ($W_r/W_i > 1$): by the aid of a universal curve presented here, the measured derivative amplitudes can be corrected so as to truly represent the atomic concentrations in the sample.

This work was supported in part by U.S. Army Research Office grant No. DAAG29-84-G-0059 and in part by a National Science Foundation EPSCOR grant RII 8610677.

¹C. C. Chang, in *Characterization of Solid Surfaces*, edited by P. F. Kane and G. B. Larrabee (Plenum, New York, 1974), Chap. 20.

²C. C. Chang, *Surf. Sci.* **48**, 9 (1975).

³M. T. Anthony and M. P. Seah, *J. Electron Spectrosc. Relat. Phenom.* **32**, 73 (1983).

⁴M. P. Seah and M. T. Anthony, *J. Electron Spectrosc. Relat. Phenom.* **32**, 87 (1983).

⁵M. P. Seah, M. T. Anthony, and W. A. Dench, *J. Phys. E* **16**, 848 (1983).

⁶M. P. Seah, *Surf. Interface Anal.* **9**, 85 (1986) and references therein.

⁷M. P. Seah, *Vacuum* **36**, 399 (1986) and references therein.

⁸A. Savitsky and M. J. E. Golay, *Anal. Chem.* **36**, 1627 (1964).

⁹L. E. Davis, N. C. MacDonald, P. W. Palmberg, G. E. Riach, and R. E. Weber, *Handbook of Auger Electron Spectroscopy*, 2nd ed. (Physical Electronics, Eden Prairie, 1975).

¹⁰G. E. McGuire, *Auger Electron Spectroscopy Reference Manual* (Plenum, New York, 1979).

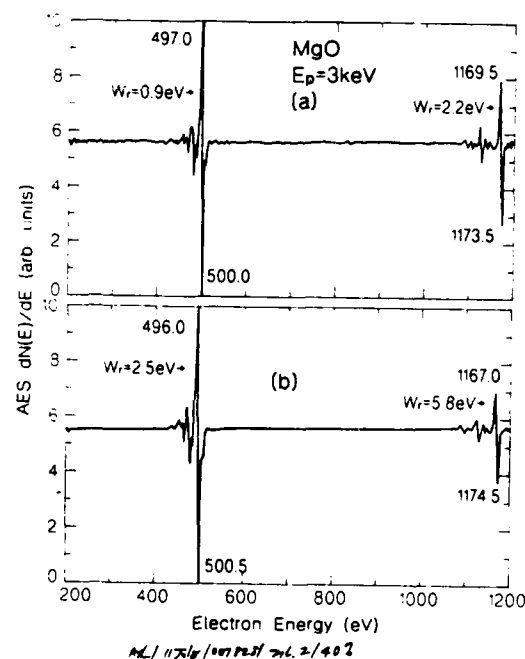
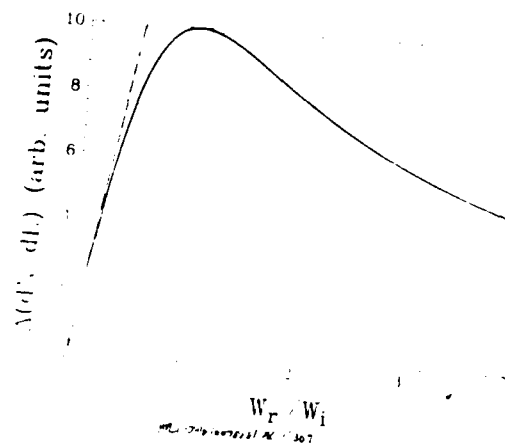
¹¹Auger Electron Spectra Catalogue—A Data Collection of Elements. Anelva Corp., Tokyo, 1979.

¹²T. Sekine, Y. Nagasawa, M. Kudo, Y. Sakai, A. S. Parkes, J. D. Geller, A. Moganu, and K. Hirata, *Handbook of Auger Electron Spectroscopy* (JEOL, Tokyo, 1982).

¹³L. A. West, *J. Vac. Sci. Technol.* **13**, 198 (1976).

FIG. 1. Calculated Auger derivative amplitude $\Delta(dN/dE)$ (solid curve) as a function of the ratio W_r/W_i of the instrumental to natural linewidth. The dashed line is an extrapolation of the linear section of the curve at the origin.

FIG. 2. Two Auger $dN(E)/dE$ spectra of MgO taken at a primary beam energy of 3 keV. The spectrum in (a) was measured with our best instrumental resolution, that in (b) with purposely degraded resolution. The resolution widths W_r for the oxygen (~ 500 eV) and magnesium (~ 1170 eV) lines, as well as the main peak energies, are marked on the figure.



THE OXYGEN AUGER LINE IN ZnO AND MgO

S.Z. Weisz and O. Resto
Dept. of Physics, University of Puerto Rico,
Rio Piedras, PR 00931

and

Y. Goldstein, G. Yaron, and A. Many
Racah Institute of Physics, The Hebrew University,
Jerusalem, Israel

ABSTRACT

High resolution measurements reveal a double peak structure in the oxygen KLL line in ZnO which is absent in MgO. The structure is attributed to local humps in the valence-band density-of-states function of ZnO. The results also illustrate the need for high-resolution measurements of sensitivity factors, if these factors are to be used for quantitative determination of atomic concentrations.

INTRODUCTION

In a recent paper¹ we have reported on measurements of Auger Electron Spectroscopy (AES) on different faces of single crystal ZnO. From these measurements we have derived the relative Auger sensitivity factor for oxygen in ZnO. This value was in good agreement with the theoretical calculations of Mrockowski and Lichtman,² but differed quite appreciably from the oxygen sensitivity cited in the Handbook of AES.³ The difference was attributed to the unusually large oxygen linewidth (about 9V), as contrasted, for example, with the much narrower oxygen line in MgO.³

In this paper we report on careful measurements of the oxygen Auger lines in ZnO and MgO. The measurements were performed at 3 and 5 keV primary-beam energies with different instrumental resolutions. At sufficiently high resolution, we find that the main oxygen line in ZnO exhibits closely spaced double peaks. At somewhat lower resolutions, the double peaks gradually merge and the oxygen line appears to widen. The measured spectra for MgO, taken with the same resolutions, failed to disclose the oxygen double peaks observed on ZnO. Here too the line widens with decreasing resolution, but much less so than in ZnO.

RESULTS

The measurements were carried out on single-crystal ZnO and MgO samples. They were mounted in the vacuum chamber of a Physical Electronics model 560 scanning Auger microprobe, where the surfaces were cleaned by repeated cycles of argon-ion bombardment.

Figure 1 displays Auger $dN(E)/dE$ surveys of a ZnO surface at two different analyzer resolutions. The measurements were performed on the "prism" face¹ with a primary electron beam-energy E_p of 3 keV. The surface is seen to be clean, exhibiting only the oxygen and zinc lines at about 500 and 1000 eV, respectively, except for a weak argon line at ~ 215 eV originating from the argon sputter cleaning. The Auger surveys were normalized by dividing the "as measured" data by the energy E . Such normalization is often applied in order to compensate for the increasing analyzer resolution linewidth with increasing energy. In Fig. 1a, corresponding to the higher instrumental resolution, the ratio of the oxygen to zinc line intensities (1.5) agrees well with that measured previously.¹ Unfortunately, however, this is not very meaningful, because of the presence of a double peak in the oxygen line (see also Fig. 2 below). The ratio of the oxygen to zinc line intensities is then resolution dependent, as illustrated by the Auger derivative spectrum in Fig. 1b, taken at a somewhat lower resolution, where the ratio has increased to about 2.

We shall define the resolution linewidth W , as the energy separation between the positive and

negative derivative peaks of the analyzer's resolution function. This linewidth can be determined very simply by differentiating the signal originating from the elastically scattered electron beam. One uses a sufficiently high primary-beam energy, say 2000 eV, for which the energy spread associated with the cathode emission of the electron gun is negligible compared to W_r at that energy. Since W_r is directly proportional to energy, the resolution linewidth can readily be scaled down to the oxygen and zinc Auger energies of about 500 and 1000 eV, respectively. The values of W_r so obtained are marked on Fig. 1.

Figure 2 displays three blown-up plots, at different analyzer resolutions, of the Auger derivatives of the oxygen line in ZnO. The measurements were taken on the prism face with a primary-beam energy E_p of 5 keV. For clarity of presentation the curves were shifted with respect to each other along the vertical axis. The values of W_r are marked on the figure next to each curve. The bottom plot [curve (a)], taken with the highest resolution, shows clearly that the positive and negative derivatives of the main oxygen line consist each of closely spaced double peaks. The energy separations of the positive and negative double peaks are 2.4 and 4.6 eV, respectively. Moving on to curves (b) and (c), taken with progressively lower resolutions, we see that the double peaks become less pronounced until in curve (c) only traces of the double peak can be seen (at the negative derivative).

The situation is quite different for the oxygen line of MgO, shown in Fig. 3. Here, as well, three blown-up plots are displayed of the Auger derivatives of the oxygen line, taken at $E_p = 5$ keV and with the same resolutions as those used for the data of Fig. 2. It is seen that even with the highest resolution [curve (a)], the oxygen line in MgO is not split into double peaks. As the resolution of the analyzer decreases [curves (b) and (c)], the oxygen line widens, as expected.

In order to check whether the presence of the double peaks in the ZnO oxygen line is characteristic of the prism face, we have carried out measurements on the (0001) "zinc" and the (000T) "oxygen" faces of ZnO. We invariably observed the double peaks, just as for the prism face (Fig. 2). That the double peaks are not due to surface effects was evidenced by measurements on freshly ion-bombarded surfaces, on annealed surfaces, and on surfaces exposed to oxygen after the sputter cleaning. In all these cases the double peaks were observed to remain essentially unchanged.

It should be pointed out that the ZnO double peaks, pronounced as they may appear in the derivative $dN(E)/dE$ curves (Fig. 2), show up merely as small wriggles in the $N(E)$ curve. This is seen in Fig. 4, where the $N(E)$ curves, from which the derivatives of Fig. 2 were obtained, are displayed. The small wriggles occur at 506.4 eV and, less pronouncedly, at 501.4 eV.

DISCUSSION

The two energy bands involved in the Auger emission process in both ZnO and MgO are the respective valence bands and the much deeper (by about 500 eV) K band of oxygen. The latter is expected to be narrow, so that the Auger emission processes in the two crystals should reflect essentially the valence-band structures. Whereas, judging from the shapes of the Auger oxygen lines, the density-of-states function of the MgO valence band seems to be rather smooth, that of ZnO appears to have local humps on both sides of the maximum density (see the wriggles in the N(E) curve of Fig. 4).

The occurrence of closely-spaced peaks in the Auger derivative spectrum of the oxygen line in ZnO also illustrates the need for high-resolution measurements of sensitivity factors for quantitative determination of atomic concentrations based on these factors. As will be shown elsewhere⁴ this requirement of high resolution is essential even in the absence of double peaks. Otherwise, the relative peak-to-peak derivative amplitudes depend in a rather complicated manner on the resolution linewidth and do not, therefore, represent the sensitivity factors to any reasonable degree of accuracy.

ACKNOWLEDGMENT

This work was supported in part by an NSF-EPSCOR grant RII 8610677 and in part by U.S. Army Research Office Grant No. DAAG29-84-G-0059.

REFERENCES

¹S.Z. Weisz, O. Resto, G. Yaron, A. Many, and Y. Goldstein, *J. Vac. Sci. Technol. A5*, 302 (1987).

²S. Mrockowski and D. Lichtman, *J. Vac. Sci., Technol. A3*, 1860 (1985).

³L.E. Davis, N.C. MacDonald, P.W. Palmberg, G.E. Riach, and R.E. Weber, *Handbook of Auger Electron Spectroscopy*, 2nd ed. (Physical Electronics, Eden Prairie, 1976).

⁴A. Many, Y. Goldstein, S.Z. Weisz, and O. Resto (to be published).

FIGURE CAPTIONS

Figure 1. Two Auger $dN(E)/dE$ surveys of the prism face of a ZnO single crystal sample, taken with a 3 keV primary beam energy and with different instrumental resolutions. The resolution linewidths W_r for the oxygen (~ 500 eV) and the zinc (~ 1000 eV) lines are marked on the figure.

Figure 2. Three blown-up Auger derivative spectra of the oxygen KLL line in ZnO exhibiting double peaks, and their disappearance with increasing resolution linewidth, measured on the prism face at a primary beam energy of 5 keV. The resolution linewidths W_r for the different curves are marked on the figure. For the sake of clarity, the curves are shifted vertically with respect to each other.

Figure 3. Derivative spectra of the oxygen KLL line in MgO measured under identical conditions as for the data in Fig. 2.

Figure 4. Three Auger electron-density $N(E)$ spectra of the oxygen KLL line in ZnO, from which the curves in Fig. 2 were derived. The energies of the wriggles, at 506.4 and at 501.4 eV (as well as the peak energies), are marked on curve (a).

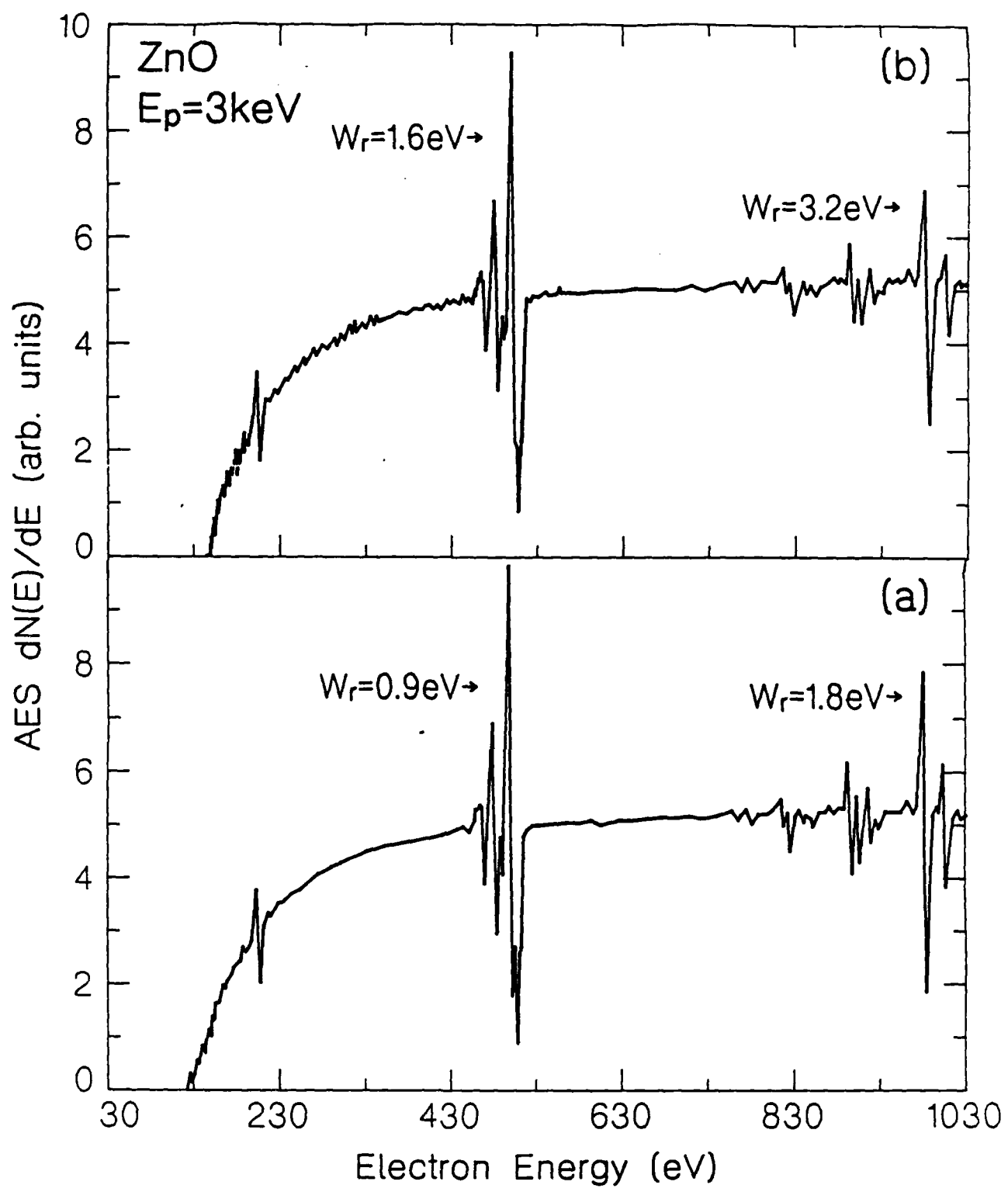


Fig. 1

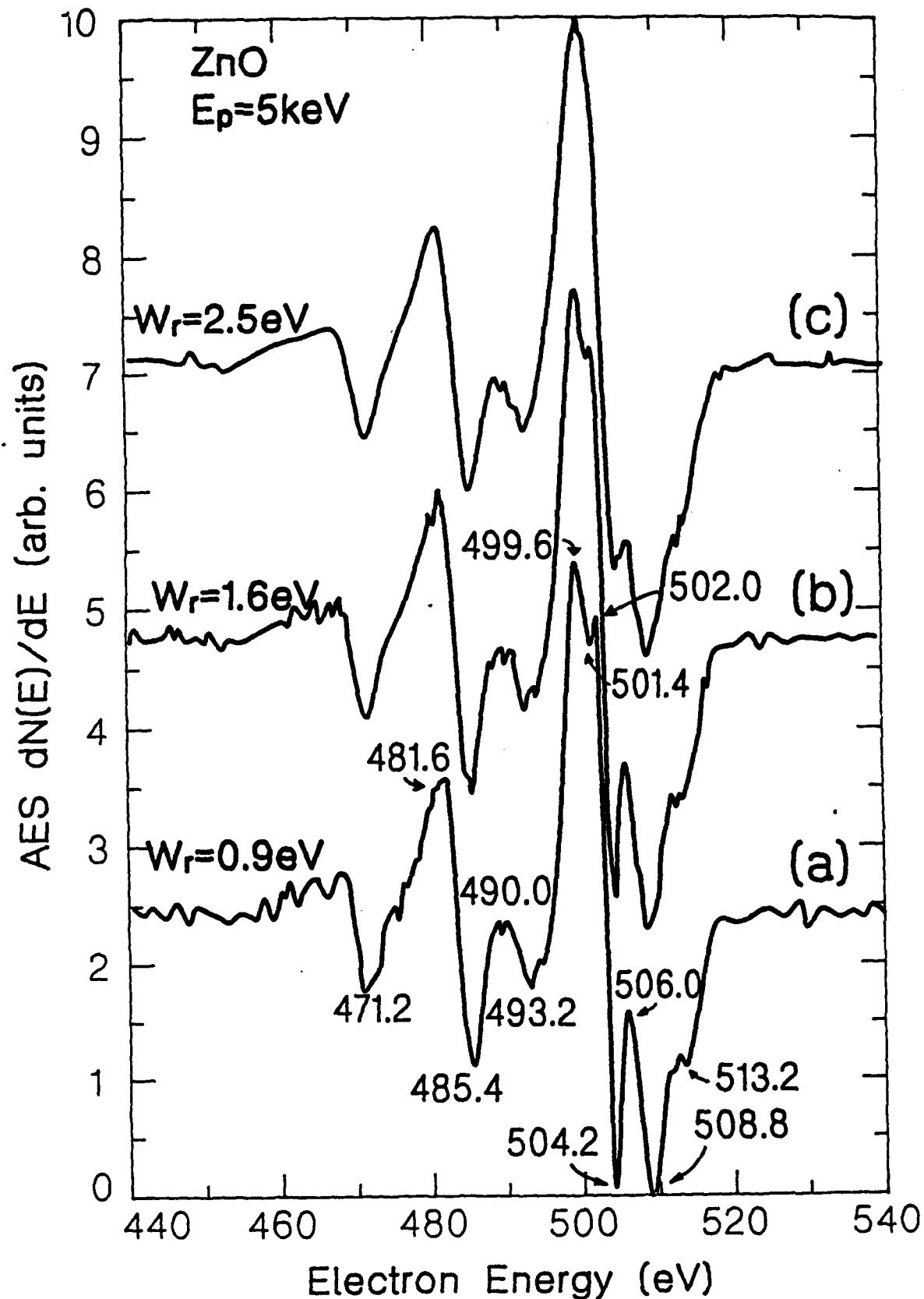


Fig. 2

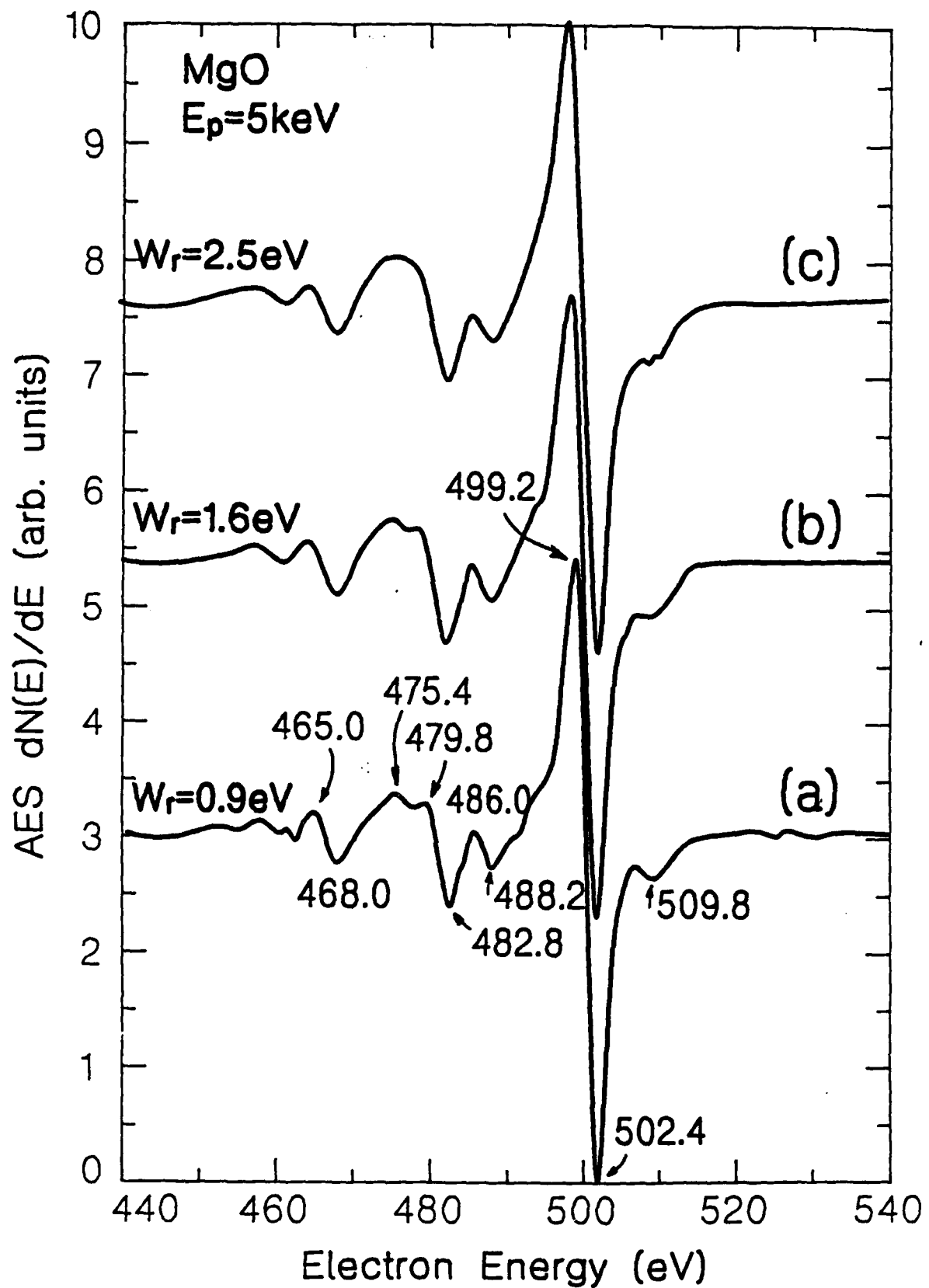


Fig. 3

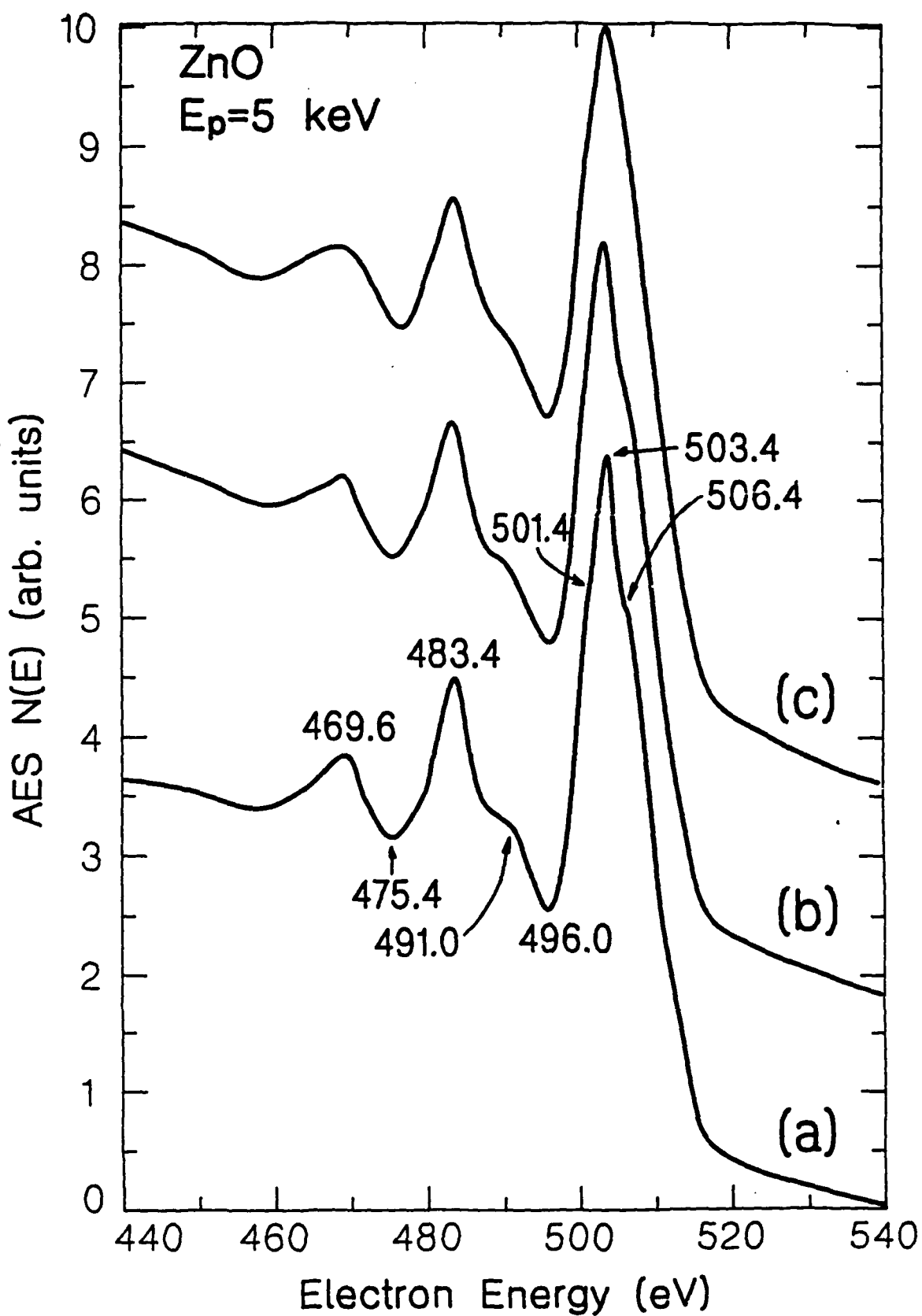


Fig. 4

1
f. L. et al.

QUANTITATIVE DETERMINATION OF ATOMIC CONCENTRATIONS
BY AUGER ELECTRON SPECTROSCOPY

Y. Goldstein, A. Many and O. Millo

Racah Institute of Physics, The Hebrew University
Jerusalem 91904, Israel

and

S.Z. Weisz and O. Resto
Dept. of Physics, University of Puerto Rico,
Rio Piedras, PR 00931

ABSTRACT

A simple mathematical analysis presented here shows that unless the ratio of the instrumental resolution width to the natural linewidth of each Auger line is less than about 0.3, the measured peak-to-peak amplitudes of the differentiated Auger signals do not represent accurately the atomic concentrations. At the same time, the analysis provides the means for overcoming this difficulty even when the linewidth ratio is considerably larger than 0.3. A universal relation is presented whereby the experimentally measured peak-to-peak amplitudes can be corrected so as to enable one to derive quite accurately the relative atomic concentrations in one's samples. So much so, provided reliable Auger sensitivities of the elements are available. Unfortunately, however, most of the sensitivity data, especially for the high energy Auger lines, were measured with insufficient resolution. In fact, we show

that at least in some cases the published data were measured with a resolution far from satisfactory. It is our contention, therefore, that there is a need for a revision of the sensitivity data with the required resolution if they are to be used for quantification.

INTRODUCTION

It is becoming more and more of a practice to use Auger Electron Spectroscopy (AES) for a quantitative determination of the concentrations of the different atomic species comprising a solid. In this method one usually measures^{1,2} the peak-to-peak amplitudes of the Auger-signal derivatives $dN(E)/dE$ corresponding to the different elements, where $N(E)$ is the energy distribution of the Auger electron intensity. These amplitudes will be referred to for short as the "derivative amplitudes" and will be denoted by $\Delta(dN/dE)$. In order to derive the atomic concentrations from the measured derivative amplitudes, one usually employs pre-determined Auger sensitivities.³⁻⁶

The Auger derivative $dN(E)/dE$ is measured by the analyzer modulation technique^{7,8} or by computer differentiation⁹ of the measured $N(E)$ curve. The effect of the modulation amplitude on the derivative spectrum has been extensively studied, primarily by Seah and co-workers.^{7,8,10-12} These workers showed that as long as the ratio of the peak-to-peak modulation amplitude to the measured Auger linewidth is less than about 0.7, the measured signal represents accurately the derivative. As to computer differentiation,⁹ Seah, Anthony and Dench¹² showed that it is equivalent in this respect to amplitude modulation, with the energy excursion used for computing the derivative replacing the peak-to-peak modulation amplitude (apart from a factor close to unity).

Even if the derivative amplitudes were determined precisely, whether by modulation or by computer

differentiation, the remaining important question in quantification is how accurately do the derivative amplitudes represent the relative atomic concentrations in a given sample. The analyzer resolution is a very important factor in this respect, and in this paper we examine its effect on the derivative amplitude. It is shown both analytically and experimentally that only if the ratios of the instrumental resolution width to the natural width for all the elements under study are smaller than about 0.3, are the magnitudes of the corresponding derivative amplitudes truly representative of the atomic concentrations. Otherwise, the derivative amplitudes depend on the resolution width in a rather complicated manner and are consequently largely meaningless.

In order to derive quantitatively the actual concentration one needs, in addition, reliable Auger sensitivities of the elements involved. The best procedure is to measure the sensitivities *in situ*. Usually, however, one relies on pre-determined sensitivities. Several compilations of such sensitivities have been published.³⁻⁶ Unfortunately, however, most of the sensitivity measurements were taken with the commonly available energy resolution of about 0.5% of the Auger energy, corresponding, for example, to 5 eV at an energy of 1000 eV. Since the natural width of many elements range between 1.5 to 4 eV, it is unavoidable that the above-mentioned requirement that the width ratio be smaller than 0.3 may not be always satisfied. For example, as will be shown below, there is reason to believe that at least some of the measurements in the Handbook of AES by Davis *et al.*,³ perhaps the most commonly

used compilation, were performed with inadequate resolution. We therefore believe that a revision of the sensitivity data is advisable. Also, it would be most useful to include in the revised Handbook the natural linewidths of the elements. The user could then check his own experimental resolution against these linewidths. However, even if the user does not have the required resolution, he would still be able to derive atomic concentrations quite accurately on the basis of the revised sensitivity data. A procedure is described below whereby the experimentally measured derivative amplitudes can be corrected so as to yield the correct relative atomic concentrations.

It should be noted that the effect on the derivative amplitude of modulation amplitude discussed by Seah and co-workers^{7,8,10-12} and of analyzer resolution considered here are two totally different issues. The former deals with the accuracy with which the derivative amplitudes are measured, whereas the latter is concerned with how close do the derivative amplitudes, even if determined accurately, represent the atomic concentrations in the sample. Other instrumental factors affecting the accuracy of the derivative amplitudes, such as reproducibility¹³ and the variation of the electron multiplier efficiency with electron energy,⁷ have been discussed in the literature, and will not be considered here.

ANALYSIS

For the calculation of the derivative amplitude of a given element (i-th line), we assume Gaussian line shapes for both the Auger line and the analyzer's resolution function. This is

certainly a realistic representation for the resolution function. As to the Auger line, the Gaussian representation is a reasonable approximation for well resolved single peaks. Moreover, the results of the analysis are not expected to depend critically on the precise line shapes taken. If there are closely spaced, overlapping peaks, the analysis is more complicated and will not be considered here.

With the above assumptions, the measured Auger-electron distribution $N_i(E)$ in the vicinity of the i -th peak is proportional to

$$N_i(E) \propto X_i \int \exp[-(E-E_i)^2/2\sigma_i^2] \exp[-(E-E)^2/2\sigma_r^2] dE, \quad (1)$$

where X_i is the atomic concentration corresponding to the i -th Auger peak, E_i is the peak's energy, σ_i is its natural linewidth, σ_r is the linewidth of the resolution function, and E is the integration variable; the integration is to be performed in the neighborhood of the i -th peak. The derivative is obtained by differentiating the integrand with respect to E :

$$dN_i(E)/dE \propto X_i \int \{1 + [(\bar{E}-E)/\sigma_r] (d\sigma_r/dE)\} f(E, E_i, \sigma_i, \sigma_r, E) dE, \quad (2)$$

where

$$f(E, E_i, \sigma_i, \sigma_r, E) = [(\bar{E}-E)/\sigma_r^2] \exp[-(\bar{E}-E_i)^2/2\sigma_i^2] \exp[-(\bar{E}-E)^2/2\sigma_r^2]. \quad (3)$$

The second term in the curly brackets of eq. (2) originates from the energy dependence of σ_r (usually $\sigma_r \propto E$). Actually, however, this term is very small compared to unity: in most analyzers $d\sigma_r/dE$ is less than 0.005, while $|(\bar{E}-E)/\sigma_r|$ is of the

order of unity or less throughout the effective range of integration. (When $|(\bar{E}-E)/\sigma_r|$ exceeds ~1.5, the function f contributes very little to the integral.) We shall accordingly neglect the second term in the curly brackets of eq. (2). This corresponds to treating σ_r as effectively constant in the vicinity of each Auger peak, and introduces an error of less than one percent for most Auger lines. By measuring the energies in units of the resolution width and shifting the origin to E_i , i.e., by substituting $x=(\bar{E}-E_i)/\sigma_r$ and $y=(E-E_i)/\sigma_r$, we obtain

$$dN_i(\bar{E})/d\bar{E} \propto X_i \int g(x, y, \sigma_r/\sigma_i) dx, \quad (4)$$

where

$$g(x, y, \sigma_r/\sigma_i) = (x-y) \exp[-x^2/2(\sigma_i/\sigma_r)^2] \exp[-(x-y)^2/2]. \quad (5)$$

In this form, the integral becomes a universal function of y , depending only on the parameter σ_r/σ_i . Actually, because we are dealing with derivatives, more suitable parameters than σ_r and σ_i would be the energy separations for each Gaussian between the positive and negative derivative peaks. It is these latter that will henceforth be referred to as the resolution width W_r and the Auger natural width W_i , respectively. Obviously for the Gaussian functions assumed $W_r = 2\sigma_r$ and $W_i = 2\sigma_i$. In terms of these widths, integration of eq. (4) yields

$$dN_i/d\bar{E} \propto -\sqrt{2\pi} X_i (W_r/W_i)^2 [1 + (W_r/W_i)^2]^{-3/2} y \exp\{-y^2/2[1 + (W_i/W_r)^2]\}$$

(6)

where W_r refers to the resolution width at the i -th Auger peak.

By differentiating eq.(6) we find that the maximum and minimum of the derivative occur at $y = \pm[1+(W_i/W_r)^2]^{1/2}$. Thus the measured derivative width W_m is given by the relation

$$W_m^2 = W_r^2 + W_i^2 . \quad (7)$$

The derivative amplitude $\Delta(dN_i/dE)$, which is equal to the difference between the maximum and minimum of $dN_i(E)/dE$, is proportional to

$$\Delta[dN_i(E)/dE] \propto \sqrt{8\pi} \exp(-\frac{1}{2}) X_i (W_r/W_i) / [1 + (W_r/W_i)^2] . \quad (8)$$

The universal relation in eq. (8) shows that the derivative amplitude $\Delta(dN/dE)$ rises linearly with increasing resolution width for $W_r/W_i \leq 0.3$, attains a maximum at $W_r/W_i = 1$ and then decreases. This behavior is a result of two competing processes: $N(E)$ increases with increasing resolution width but at the same time the measured line also widens and the derivative eventually decreases. Equation (8) has far-reaching consequences concerning the use of Auger measurements for quantitative analyses. The derivative amplitude is a direct measure of the atomic concentration X_i only in the linear range, assuming, of course, that the pre-determined sensitivities used in the quantification have also been measured with $W_r/W_i < 0.3$. The W_r dependence of $\Delta(dN/dE)$ is the

reason for the procedure, sometimes adopted, of dividing each derivative amplitude by W_r or, equivalently, by E. Such a procedure is meaningful only for $W_r/W_i < 0.3$. For larger W_r/W_i , the 1/E normalization is less adequate and becomes outright meaningless for $W_r/W_i > 1$.

There is, however a simple procedure to correct the measured derivative amplitudes for $W_r/W_i > 0.3$ so as to make the results meaningful. One derives from eq.(8) the values one would have measured were the analyzer resolution sufficiently good ($W_r/W_i < 0.3$). To do that, one multiplies the measured derivative amplitude for each line (each W_r/W_i) by a correction factor, given by $[1 + (W_r/W_i)^2]$. Such a procedure extends, in effect, the linear range of eq.(8) to $W_r/W_i > 0.3$. For $W_r/W_i < 0.3$, the correction factor is close to unity, as it should, while for larger W_r/W_i it increases fairly rapidly, reaching, for example, a value of 10 at $W_r/W_i = 3$. It is the corrected derivative amplitudes that are truly representative of the atomic concentrations throughout the range of W_r/W_i .

The existing atomic sensitivity data³⁻⁶ are lacking in two important aspects. First, the natural widths W_i for the different elements are not specified. Secondly, as pointed out above, most of the data were measured with a resolution of about 0.5%. Hence, the ratios W_r/W_i may very well exceed in many cases the value of 0.3, possibly by quite a large margin. The sensitivities listed in the various handbooks are thus suspect, to say the least. This is particularly the case for the high energy lines, for which the analyzer resolution is necessarily less good.

These considerations point to the need for compiling a revised sensitivity Handbook. On the basis of the revised data, the user would be able to derive atomic concentrations quite accurately, even if his own instrumental resolution is rather poor (W_r/W_i larger than 0.3 by as much as an order of magnitude). First, however the user should determine his own analyzer resolution width W_r . This can be done very simply by differentiating the signal originating from the elastically scattered electron beam. One uses a sufficiently high primary-beam energy, say 2000 eV, for which the energy spread associated with the cathode emission of the electron gun is negligible compared to W_r at that energy. Since W_r is proportional to energy, its value at any Auger line can readily be evaluated. Using the natural widths W_i of the Auger lines of the different atoms in the sample under study, as obtained from the revised Handbook, one calculates the linewidth ratio W_r/W_i and corrects the measured derivative amplitudes with the aid of eq.(8). These corrected derivative amplitudes, in conjunction with the sensitivity data in the revised Handbook, should yield rather accurately the relative atomic concentrations in the sample.

RESULTS

In order to illustrate the above considerations, we present some Auger derivative spectra obtained with different instrumental resolutions. The measurements were carried out on single-crystal MgO samples. The samples were mounted in the vacuum chamber of a Physical Electronics model 560 scanning

Auger microprobe, where the surfaces were cleaned by repeated cycles of argon-ion bombardment. The resolution was varied by changing the analyzer apertures. The resolution widths W_r were determined in each case by differentiating the signals originating from the elastically scattered electrons at a primary beam energy of 2000 eV, as discussed above. The derivative spectra were obtained by 5-point computer differentiation⁹ of the measured N(E) spectra, with a ± 1 eV overall excursion. The "differentiation potential"¹² is thus 2 eV, which is less than 0.7 of the measured widths of all the Auger lines to be displayed. Hence this procedure yields accurate values for the derivative spectra.¹²

In Figs. 1-3 AES derivative spectra of MgO, measured with three different instrumental resolutions, are displayed. The values of the resolution widths at the oxygen and magnesium lines, as well as the peak energies, are marked on the figures. The data were taken with a primary beam energy of 3 keV. For the data in Fig. 1, taken with our highest resolution, the W_r values at the oxygen and magnesium peak energies are 0.9 and 2.2 eV, respectively. The measured oxygen and magnesium widths W_m are 3.0 and 4.0 eV, respectively. Using eq.(7), we conclude that the natural widths of the oxygen and magnesium lines are $W_i(O)=2.9$ eV and $W_i(Mg)=3.3$ eV. We see, then, that W_r/W_i for Mg, 0.67, is appreciably larger than 0.3, so that even for our best resolved data (W_r/E only 0.2% !) a significant correction should be applied to the measured Mg derivative amplitude. The correction factor, as evaluated from eq.(8) is 1.45. To be precise, a small correction of 1.1 should be applied also to

the oxygen line ($W_r/W_i=0.31$). Hence, the measured ratio of the two derivative amplitudes, 1.9, should be multiplied by $1.1/1.45$ to yield the corrected ratio of 1.4.

The resolution widths in Figs. 2 and 3 were purposely made progressively larger, as marked in the figures. Whereas the resolution widths for oxygen are still smaller than $W_i(O)$, those for magnesium become larger than $W_i(Mg)$. This is exhibited by the dramatic decrease of the magnesium derivative amplitude and the increase of the measured oxygen to magnesium amplitude ratios: from 1.9 in Fig. 1, to 2.3 in Fig. 2, and to 3.1 in Fig. 3. In order to demonstrate the usefulness of eq.(8) we shall also derive the corrected derivative-amplitude ratio from the less resolved data of Figs. 2 and 3 ($W_r/E = 0.32\%$ and 0.5%, respectively, better than or comparable to the resolution commonly used). With the natural widths determined from Fig. 1, and using the correction procedure outlined above, we find for the corrected ratio of oxygen to magnesium derivative amplitudes the value of 1.3 for the data in both Figs. 2 and 3. This differs by no more than 10% from the value of 1.4 derived from the best resolved data of Fig. 1. It should be noted that if no correction were applied, the error in deriving the oxygen to magnesium concentration ratio would have been quite appreciable, amounting, for example, to a factor of over two for the data in Fig. 3.

We have also evaluated the oxygen to magnesium derivative-amplitude ratio from the MgO Auger spectrum appearing in the Davis et al.'s Handbook of AES.³ The value obtained is 3.2, very close to the result of 3.1 obtained from our poorest

resolved data, in which W_r/W_i appreciably exceeds the value of 0.3 for both elements. Furthermore, if we apply the Handbook sensitivities for oxygen (0.5) and magnesium (0.1) to our oxygen to magnesium derivative-amplitude ratio (1.4), we come up with oxygen and magnesium concentrations of 22% and 78%, respectively, instead of the expected value of 50% for each element.

CONCLUSION

The presently available sensitivity data are inadequate because the resolution used in measuring most of them ($W_r/E = 0.5\%$) was insufficient. This was demonstrated for the case of the MgO spectrum in the Davis *et al.*'s Handbook of AES.³ We therefore feel that there is a need for a revised Handbook which would present Auger spectra and sensitivity data based on measurements in which the condition $W_r/W_i < 0.3$ is ensured. The revised Handbook should also include the natural linewidths W_i of all the elements.

With the availability of the revised Handbook, the user would be able to determine fairly accurately the relative atomic concentrations in his sample, even if his own instrumental resolution is rather poor ($W_r/W_i > 1$). A simple experimental procedure has been suggested for measuring the resolution width, so that the ratios W_r/W_i can be determined for all the Auger lines under study. By the aid of a universal relation, the user can then correct, if necessary, the measured derivative amplitudes so as to truly represent the atomic concentrations in the sample.

ACKNOWLEDGEMENT

This work was supported in part by U.S. Army Research Office Grant No. DAAG29-84-G-0059 and in part by an NSF-EPSCOR grant RII 8610677.

REFERENCES

- ¹ C.C. Chang in *Characterization of Solid Surfaces*, eds. P.F. Kane and G.B. Larrabee (Plenum, New York, 1974), Ch. 20.
- ² C.C. Chang, *Surf. Sci.* **48**, 9 (1975).
- ³ L.E. Davis, N.C. MacDonald, P.W. Palmberg, G.E. Riach, and R.E. Weber, *Handbook of Auger Electron Spectroscopy*, 2nd ed. (Physical Electronics, Eden Prairie, 1976).
- ⁴ G.E. McGuire, *Auger Electron Spectroscopy Reference Manual* (Plenum, New York, 1979).
- ⁵ *Auger Electron Spectra Catalogue - A Data Collection of Elements* (Anelva Corp., Tokyo, 1979).
- ⁶ T. Sekine, Y. Nagasawa, M. Kudo, Y. Sakai, A.S. Parkes, J.D. Geller, A. Mogami, and K. Hirata, *Handbook of Auger Electron Spectroscopy* (JEOL, Tokyo, 1982).
- ⁷ M.P. Seah, *Surf. Interface Anal.* **9**, 85 (1986) and references therein.
- ⁸ M.P. Seah, *Vacuum* **36**, 399 (1986) and references therein.
- ⁹ A. Savitsky and M.J.E. Golay, *Anal. Chem.* **36**, 1627 (1964).
- ¹⁰ M.T. Anthony and M.P. Seah, *J. Electron Spectrosc. Relat. Phenom.* **32**, 73 (1983).
- ¹¹ M.P. Seah and M.T. Anthony, *J. Electron Spectrosc. Relat. Phenom.* **32**, 87 (1983).
- ¹² M.P. Seah, M.T. Anthony, and W.A. Dench, *J. Phys. E.* **16**, 848 (1983).
- ¹³ L.A. West, *J. Vac. Sci. Technol.* **13**, 198 (1976)

FIGURE CAPTIONS

Figure 1. Auger $dN(E)/dE$ spectrum of MgO surface taken at a primary-beam energy of 3 keV with the best instrumental resolution. The resolution widths W_r , as well as the main-peak energies for the oxygen (~ 500 eV) and magnesium (~ 1170 eV) lines are marked on the figure.

Figure 2. Auger $dN(E)/dE$ spectrum of the same MgO surface as in Fig. 1, measured with a somewhat lower resolution.

Figure 3. Auger $dN(E)/dE$ spectrum of the same MgO surface as in Figs. 1 and 2, taken with the lowest resolution.

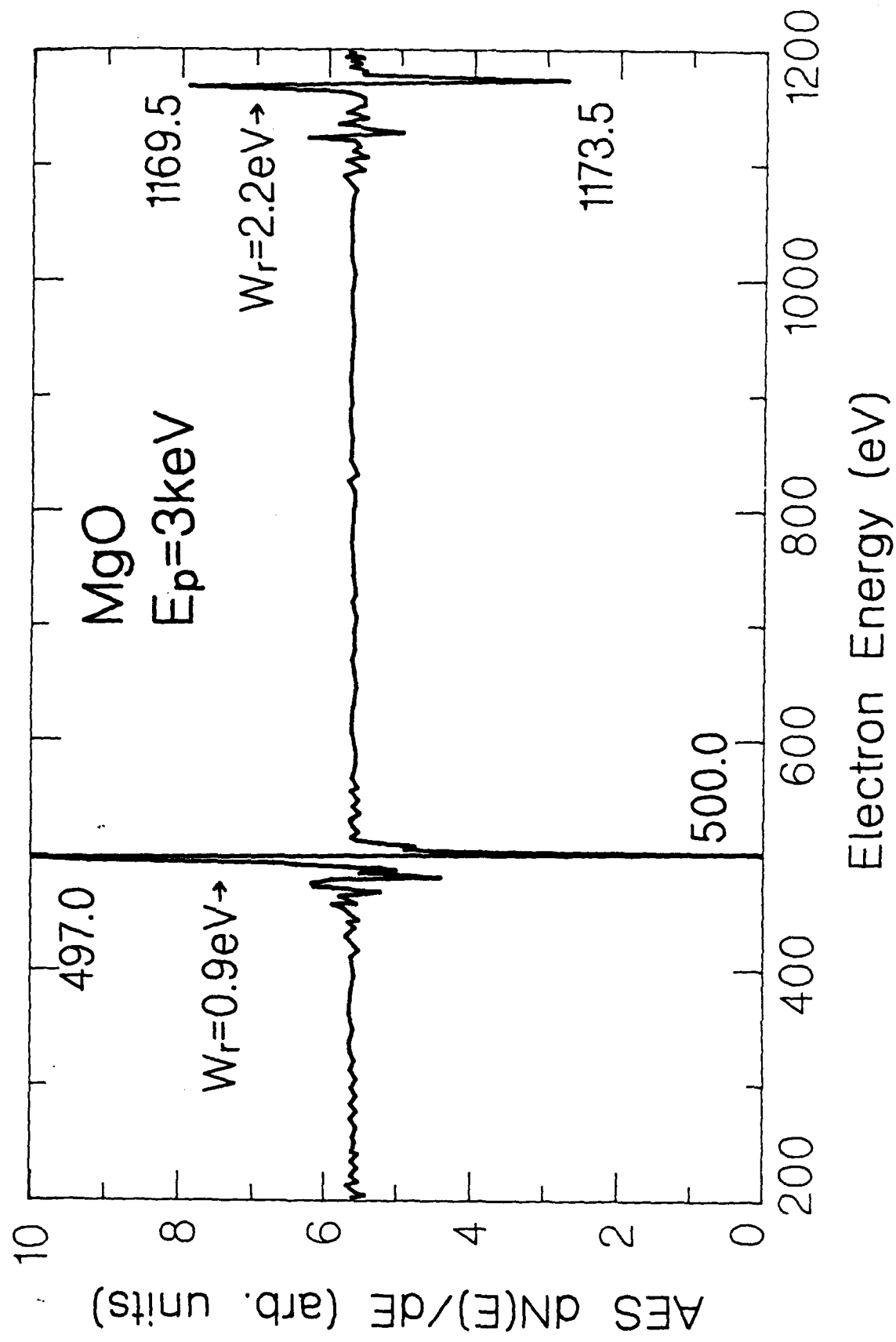


Fig. 1

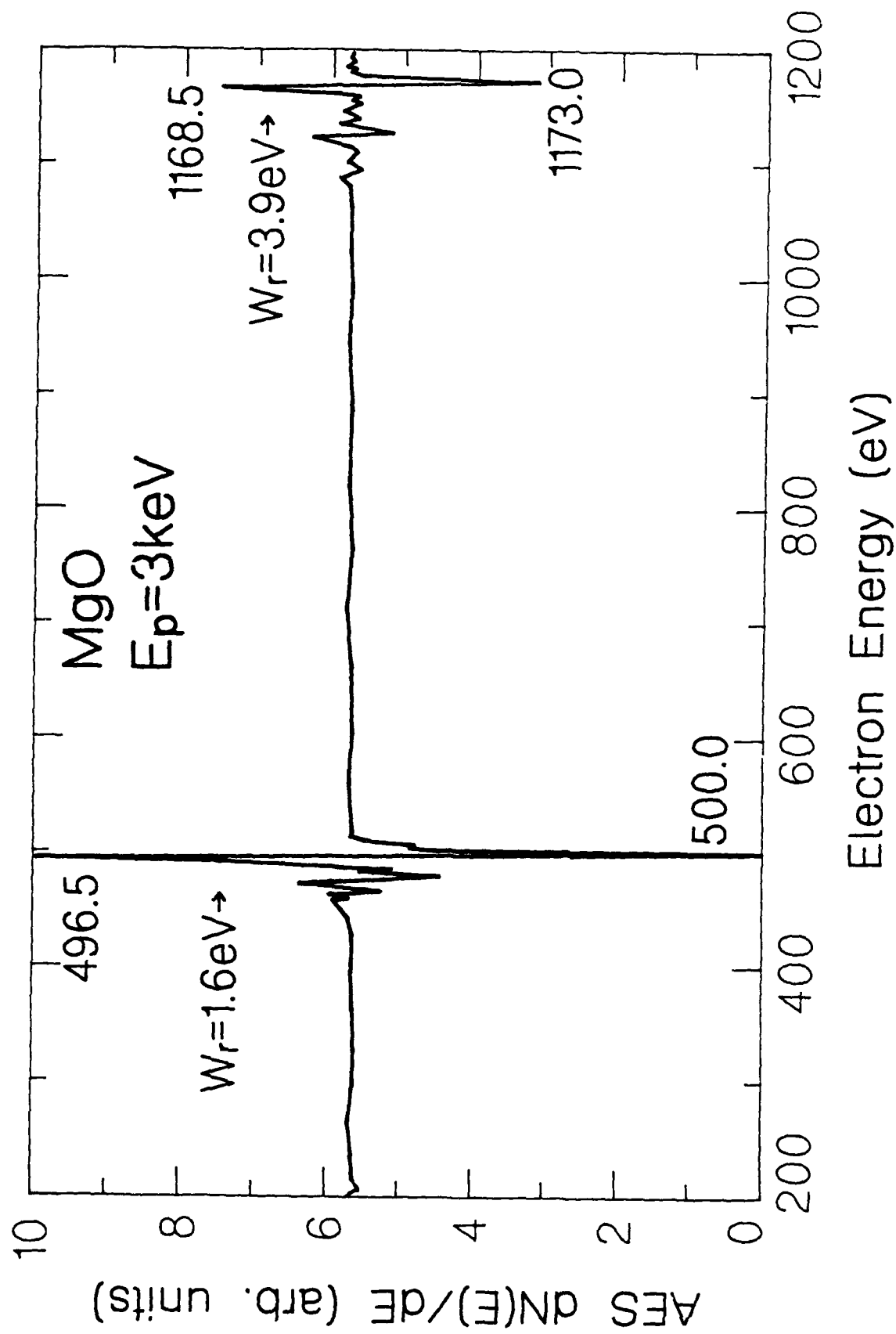


Fig. 2